

Interaction in Metal Rare Gas Complexes and Assignment of REMPI Spectra of Some Disubstituted Benzenes

Yu Zheng

Thesis submitted to the University of Nottingham

for the degree of Master of Science by Research in Chemistry

September 2018

Abstract

A consistent set of interaction energy curves are shown in this work for the Group 2 (IIA) and Group 12 (IIB) metal cation/rare gas complexes, M^+-RG, where $M^+ = Be^+–Ra^+$ and $Zn^+–Hg^+$; and RG = He–Rn. spectroscopic constants derived from these are reported and compared with available data, and discuss trends in the values. Insight into the interactions are gained that occur using a range of approaches: reduced potential energy curves; charge and population analyses; molecular orbital diagrams and contour plots; and Birge-Sponer plots. Although sp hybridisation occurs in the Be^+-RG, Mg^+-Rg and Group 12 M^+-RG complexes, this appears to be minimal and covalency is the main aspect of the interaction. However, major sd hybridisation occurs in the heavier Group 2 M^+-RG systems, which increases their interaction energies but there is minimal covalency. Examination of Birge-Sponer plots reveals significant curvature in many cases, which are ascribed to the changing amounts of hybridisation or covalency as a function of internuclear separation. This suggests why the use of a simple electrostatics-based model potential to describe the interactions is inadequate.

Assignment of four different spectra obtained by resonance-enhanced multiphoton ionisation spectroscopy (REMPI) is undertaken; these are for the four disubstituted benzene molecules: *ortho*-difluorobenzene, *ortho*-chlorofluorobenzene, *meta*–difluorobenzene and *meta*-chlorofluorobenzene . Comparing with several previous experimental studies, some results could be compared,and confirms the correctness of the analysis. More generally, the information impacts on how mixed the vibrational motions have become – this directly impacts on how well energy can be dispersed in each molecule.

Acknowledgements

Here, I show my great respect and appreciation to my supervisor, Prof. Timothy Wright. As my first supervisor abroad, he impressed a lot in different aspects. Having known him for 1 year, I was attracted by his tolerance to an International student from the stage with language barrier, even though one had met the language proficiency requirement set by the university before the arrival to the UK there were still many barriers when it came to using English in the country where the English was born. His story about how his wife from Uruguay went over with the language barrier especially on the academic aspect in the United States of America encouraged me in depth. Dr. William Tuttle helped me almost every day when he was working in Wright group at the University of Nottingham. Since my undergraduate programme is quite different from what this group is undertaking, Dr. Tuttle's instruction and clarification with highly enough patience made the understanding and insight became much easier. Numbers of confusion was solved by Dr. Tuttle. Dr. Adrian Gardner, who had gained his degree of Doctor of Philosophy in 2013 amazed me with his huge storage of knowledge as well as his abundant experience. Besides these three above, the young researcher Mr. David Kemp played an important role to illustrate tedious definitions in this spectroscopy area. I think his proximity of age and experience offered me a straightforward way to learn something new here. It is them who promoted me forward in this year.

It is my pleasure to meet these people on my first arrival to an unfamiliar country, particularly it was my first time to be abroad. This stage is really valuable for me to go over. It is my fortune to experience this annual year with all of them accompanied.

Thank you for my family in China who always supported me and encouraged me.

Contents

1 Interaction in Metal Rare Gas Complexes 1

1.1 Introduction 1

1.2 Computational Methodology 3

1.3 Results and Discussion 8

1.3.1 IECs and Spectroscopic Constants 8

1.3.2 Reduced Potentials 16

1.3.3 Trends in the Spectroscopic Constants of the Group 2 M^+-RG Series 20

1.3.4 Molecular Orbital Diagrams and Contour Plots 23

1.3.5 Partial Atomic Charge Analyses 32

1.3.6 Model Potential 35

1.3.7 Birge-Sponer Plots 40

1.3.8 $H(R)$ values 47

1.4 Conclusions 48

1.5 Bibliography 51

2 Assignment of REMPI Spectra of Disubstituted Benzenes 58

2.1 Introduction 58

2.1.1 Resonance-Enhanced Multiphoton Ionisation (REMPI) Spectroscopy 59

2.1.2 Molecular Vibrations 60

2.1.3 Labelling Scheme 60

2.1.4 Symmetries of Vibrational Modes 61

2.1.5 Combination Bands, Overtones and Fermi Resonances 61

2.2 Computational Details 62

2.3 Assignment Methodology 62

2.4 Results and Assignment 63

2.4.1 Assignment of *ortho*-difluorobenzene 63

2.4.2 Assignment of *ortho*-chlorofluorobenzene 66

2.4.3 Assignment of *meta*-difluorobenzene 69

2.4.4 Assignment of *meta*-chlorofluorobenzene 71

2.4.5 A Comparison between *ortho*-difluorobenzene and *meta*-difluorobenzene REMPI Spectra 75

2.4.6 A Comparison between *ortho*-chlorofluorobenzene and *meta*-chlorofluorobenzene REMPI Spectra 76

2.5 Conclusions 78

2.6 Bibliography 80

List of Figures

Figure 1-1. Interaction energy curves for the Group 2 M^+-RG complexes. 12
Figure 1-2. Interaction energy curves for the Group 12 M+ RG complexes. 14
Figure 1-3. Reduced potentials for the Group 2 M^+-RG complexes. 17
Figure 1-4. Reduced potentials for the Group 12 M^+-RG complexes. 18
Figure 1-5. Plots of κ (see Eqn. 1-1) for Group 2 and Group 12 M^+-RG complexes. 19
Figure 1-6. Trends in R_e for the Group 2 and Group 12 M^+-RG complexes. 20
Figure 1-7. Trends in D_e for the Group 2 and Group 12 M^+-RG complexes. 22
Figure 1-8. Trends in k for the Group 2 and Group 12 M^+-RG complexes. 23
Figure 1-9. MO diagram and contour plots for the Be^+-RG and Mg^+-RG complexes calculated at the RCCSD(T) R_e values obtained at the extrapolated basis set limit. The values of the contours were selected both to show the details clearly for all complexes, and are identical to allow direct comparison between the plots. The different colours indicate opposite signs of the wavefunction. 25
Figure 1-10. MO diagram and contour plots for the Ca^+-RG and Zn^+-RG complexes calculated at the RCCSD(T) R_e values obtained at the extrapolated basis set limit. The values of the contours were selected both to show the details clearly for all complexes, and are identical to allow direct comparison between the plots. The different colours indicate opposite signs of the wavefunction. 27
Figure 1-11. MO diagram and contour plots for the Sr^+-RG and Cd^+-RG complexes calculated at the RCCSD(T) R_e values obtained at the extrapolated basis set limit. The values of the contours were selected both to show the details clearly for all complexes, and are identical to allow direct comparison between the plots. The different colours indicate opposite signs of the wavefunction. 29
Figure 1-12. Birge-Sponer Plots for Be^+-RG and Mg^+-RG. The red dots are the calculated spacings between consecutive vibrational levels, while the line is a Morse line calculated from the ω_e and $\omega_e x_e$ values given in Table 1-1 (see text). 39

Figure 1-13. Birge-Sponer Plots for Ca^+-RG and Zn^+-RG. The red dots are the calculated spacings between consecutive vibrational levels, while the line is a Morse line calculated from the ω_e and $\omega_e x_e$ values given in Table 1-1 and Table 1-2(see text). 40
Figure 1-14. Birge-Sponer Plots for Ba^+-RG and Hg^+-RG. The red dots are the calculated spacings between consecutive vibrational levels, while the line is a Morse line calculated from the ω_e and $\omega_e x_e$ values given in Table 1-1 and Table 1-2 (see text). 42
Figure 1-15. Birge-Sponer Plots for Sr^+-RG and Cd^+-RG. The red dots are the calculated spacings between consecutive vibrational levels, while the line is a Morse line calculated from the ω_e and $\omega_e x_e$ values given in Table 1-1 and Table 1-2(see text). 44
Figure 1-16. MO diagram and contour plots for the Ba^+-RG and Hg^+-RG complexes calculated at the RCCSD(T) R_e values obtained at the extrapolated basis set limit. The values of the contours were selected both to show the details clearly for all complexes, and are identical to allow direct comparison between the plots. The different colours indicate opposite signs of the wavefunction. 45
Figure 2-1. Assigned REMPI spectra of *ortho*-difluorobenzene to wavenumber ~ 1500 cm^{-1} 64
Figure 2-2. Assigned REMPI spectra *ortho*-chlorofluorobenzene to wavenumber ~ 1500 cm^{-1}. The black trace is the ^{35}Cl isotopologue, and the red one ^{37}Cl. 67
Figure 2-3. Assigned REMPI spectra *meta*-difluorobenzene to wavenumber ~ 1500 cm^{-1} ...70
Figure 2-4. Assigned REMPI spectra *meta*-chlorofluorobenzene to wavenumber ~ 1500 cm^{-1} 73
Figure 2-5. A Comparison between assigned REMPI Spectra of *ortho*-difluorobenzene and *meta*-difluorobenzene to wavenumber ~ 1500 cm^{-1} 75
Figure 2-6. A Comparison between assigned *ortho*-chlorofluorobenzene and *ortho*-difluorobenzene REMPI Spectra to wavenumber ~ 1500 cm^{-1} 77

List of Tables

Table 1-1: Spectroscopic constants for the Group 2 M^+-RG series.[a,b] 5
Table 1-2: Spectroscopic constants for the Group 12 M^+-RG series.[a, b] 10
Table 1-3: κ values (see Eqn. 1-1) for the Group 2 and Group 12 M^+-RG Complexes 19
Table 1-4: Energies (cm^{-1}) of the excited s^0p^1, d^9s^2 and s^0d^1 states of the Group 2 and Group 12 cations[a,b] 24
Table 1-5: Partial atomic charges for the Group 12 M^+-RG complexes, calculated using NPA and AIM methodologies, in units of elementary charge *e*. 31
Table 1-6: Partial atomic charges for the Group 2 M^+-RG complexes, calculated using NPA and AIM methodologies, in units of elementary charge *e*. 32
Table 1-7: Input Parameters for the electrostatic model potential (Eqn. 1-2)[a] 35
Table 1-8: Effective charges on M^+ from the electrostatic model potential (Eqn. 1-2),[a] in units of elementary charge *e*. 38
Table 1-9: Local energy densities $H(R)$ for the Group 2 and 12 M^+-RG complexes.[a] 46
Table 2-1: Assignment of *ortho*-difluorobenzene 65
Table 2-2: Assignment of *ortho*-chlorofluorobenzene 68
Table 2-3: Assignment of *meta*-difluorobenzene 71
Table 2-4: Assignment of *meta*-chlorofluorobenzene 72

Chapter 1

Interaction in Metal Rare Gas Complexes

In this work, a consistent set of interaction energy curves for the Group 2 (IIA) and Group 12 (IIB) metal cation/rare gas complexes, M^+-RG, where $M^+ = Be^+–Ra^+$ and $Zn^+–Hg^+$; and RG = He–Rn is reported. Spectroscopic constants are derived from these and compared with available data; in addition, trends in these values are discussed. Insight into the interactions that occur in these species is gained using a range of approaches: reduced potential energy curves; charge and population analyses; molecular orbital and contour plots; and Birge-Sponer plots. Although sp hybridisation occurs in the Be^+-RG, Mg^+-RG and Group 12 M^+-RG complexes, this appears to be minimal and covalency is the main aspect of the interaction. It is concluded that sd hybridisation occurs in the heavier Group 2 M^+-RG systems (M^+ = Ca–Ra), which increases their interaction energies but does not induce covalency. Examination of Birge-Sponer plots reveals significant curvature in many cases, which is ascribed to the changing amounts of hybridisation as a function of *R*. The latter suggests why the use of a simple electrostatics-based model potential is inadequate.

1.1 Introduction

Many theoretical studies have been undertaken previously by the Wright group at the University of Nottingham on M^+-RG systems (RG = He–Rn), with the metals coming from Group 1,[1-6] Group 2,[7-9] Group 11,[10,11] Group 12,[12,13] and Group 13.[14-17] These studies have used CCSD(T) or RCCSD(T) theory with large basis sets to calculate interaction energy, E_{int}, curves (IECs), often extrapolated to the basis set limit. These IECs have been employed to obtain spectroscopic constants and to calculate transport coefficients for the metal cations moving in inert gases. At the commencement of the studies the emphasis was on obtaining reliable IECs with a view to generating transport coefficients to compare to experiment, and to compare to the limited spectroscopic data available. However, in a number of cases it was evident that the

systems were showing behaviour that was reminiscent of incipient chemical bonding, and so various methods were employed to establish the extent to which "chemistry" was present in the interactions, as opposed to just "physics". (Here, the use of the term "chemistry" includes hybridisation that occurs as a result of the interaction.) Initially, this was undertaken using a physical "model potential" [18] including damping,[1,6] but since then various population analyses have been employed, as well as molecular orbital diagrams including contour plots. Also, it has recently proven insightful to look at Birge-Sponer plots of the whole set of calculated bound vibrational levels, [15] as this seems to show subtleties in the change in shape of a IEC that are otherwise difficult to see, even using such approaches as reduced potentials.[9,15] Finally, contour plots and molecular orbital diagrams allow the visualization of the interactions between the atomic orbitals. [9,15] In the present work, the most insightful of the above methods is applied in an examination of the interactions of the Group 2 (Be^+–Ra^+) and Group 12 (Zn^+–Hg^+) metal cations with each of the rare gases (He–Rn).

Of the systems previously studied, the metal cations belonging to groups 1, 11, and 13 all possess $^1\Sigma^+$ electronic ground states, and as such it might have been anticipated that the interactions within those M^+–RG complexes would be of essentially the same character. However, as previous investigations have highlighted, interactions in the Group 11 M^+-RG complexes exhibit rather strong binding energies, [10] with Au^+-Xe in particular being very strongly bound and proposed as exhibiting a degree of covalency. [11,19] Conversely, the Group 1 complexes are comparatively weakly bound and were found to be described well by a 'physical' model potential that included the main induction and dispersion terms together with a simple repulsion potential.[6] Group 13 is a different case again, with the heavier members of the M^+-RG group showing similar behaviour to the Group 1 complexes,[16] and the lightest members, involving B^+,[15] showing strong binding energies with some incipient covalency.

Another logical comparison presents itself in the case of the Group 2 and Group 12 M^+–RG complexes. For these complexes, a single unpaired electron is present in the outermost valence *n*s orbital, and as such these all possess common $^2\Sigma^+$ electronic ground states. Consequently, on the basis of valence isoelectronic arguments, the complexes from both of these groups might be expected to exhibit close similarities in their interactions. In previous work by the Wright group at Nottingham, the Group 2 complexes have been examined in detail [7-9] but not consistently with all of the above-described methods. Unfortunately, at that time, consistent basis sets were not available for the whole set of Group 2 metals and so custom-designed basis were employed in some cases, albeit to match the quality of standard Dunning-style aug-cc-

pV5Z basis sets combined with an effective core potential for the heavier species. A similar situation occurred with the Group 12 species, [12,13] but also at that time a detailed analysis of the interactions was not undertaken.

In the present work, high-quality IECs are employed, employing consistent basis sets across the whole set of complexes and extrapolating to the basis set limit. Furthermore, analyses of the interactions are undertaken across the series using various approaches, which makes it possible to compare and contrast the interactions in these valence isoelectronic species.

1.2 Computational Methodology

As noted above, some of previous studies by the Wright group at the University of Nottingham on the Group 2 and Group 12 M^+-RG complexes employed custom-designed basis sets of the same overall construction as the Dunning-style quintuple-ζ quality basis sets. Since then, appropriate basis sets have subsequently been published for all relevant metals[20-22] and now RCCSD(T) calculations have been undertaken by J. P. Harris and W. D. Tuttle with these to obtain consistent IECs for all of the complexes; further more, since both quadruple-ζ and quintuple-ζ quality basis sets became available, it is also applicable to extrapolate the interaction potentials pointwise to the complete basis set limit using the X^{-3} method of Halkier et al.[23] In earlier work done by the Wright group at Nottingham on Be^+-RG and Mg^+-RG,[9] the basis sets employed were pre-publication versions, and these are slightly modified in their published form, and so those calculations were repeated using the published basis sets, for consistency.

RCCSD(T) IECs for each of the 54 complexes have been calculated by J. P. Harris and W. D. Tuttle using MOLPRO,[24] covering a range of internuclear separations that covered the long- and short-range as well as equilibrium separation regions. Basis sets were quadruple-ζ and quintuple-ζ quality, as described below, allowing extrapolation to the basis set limit. The final extrapolated curves may be represented as RCCSD(T)/apCV∞Z or RCCSD(T)/apwCV∞Z quality. LeRoy's LEVEL 8.0 code[25] is then employed to obtain rovibrational energy levels from each of these curves. Using these IECs, as part of the present work, a number of spectroscopic constants are then obtained from standard Morse expressions, as discussed below. Birge-Sponer-like (BS) plots were also created, using the calculated separations between the vibrational levels.

The details of the basis sets employed for the metals are as follows (with X = Q, 5): for

beryllium and magnesium, all-electron aug-cc-pwCVXZ; for Ca, Sr and Ba aug-cc-pCVXZ-PP (non-weighted-core) valence basis sets along with relativistic, small-core effective core potentials ECP10MDF, ECP28MDF and ECP46MDF, respectively; and for Zn, Cd, Hg and Ra aug-cc-pwCVXZ-PP (weighted-core) valence basis sets with relativistic, small-core effective core potentials ECP10MDF, ECP28MDF, ECP60MDF and ECP78MDF, respectively. For the rare gases, aug-cc-pVXZ basis sets were used for He, and for Kr–Rn aug-cc-pwCVXZ-PP valence basis sets were employed with small-core effective core potentials ECP10MDF, ECP28MDF, and ECP60MDF, respectively. For Ne and Ar, either aug-cc-pCVXZ or aug-cc-pwCVXZ basis sets were used to match whether a core-weighted basis set was used for the metal cation or not. The use of either core-valence or weighted-core-valence basis sets is not expected to impact the results significantly, with any effect having even less impact on interaction energies. In previous work of the Wright group at Nottingham on the Be^+-RG and Mg^+-RG complexes, doubly-augmented basis sets were employed, thus giving a better description of the diffuse regions of electron density. Although singly-augmented basis sets are mostly employed here, it was found that in several cases there was a requirement for the second set of diffuse functions; hence, as will be discussed below, in those cases RCCSD(T)/d-aCV∞Z results are presented.

For Be^+ all electrons were correlated, while for Mg^+ all but the 1s electron were correlated; for the heavier Group 2 metals, all electrons on the metal not described by the ECPs were correlated. In the cases of the rare gas atoms, the Ne 1s orbitals and Ar 1s, 2s, and 2p orbitals were frozen. Each of the heavier rare gases RG = Kr–Rn had the inner-valence (*n*-1)s and (*n*-1)p orbitals frozen. For the Group 12 systems, each of the metals Zn–Hg had only their inner-valence (*n*-1)s orbitals frozen, since the (*n*-1)p orbitals for these cations are higher in energy than the analogous Group 2 cation orbitals, and all other electrons (save for those described by the ECP) were correlated. The same correlation scheme that was used for the rare gas atoms in the Group 2 complexes was also used for Zn^+-RG and Cd^+-RG, and also for the Hg^+-He, Hg^+-Ne, and Hg^+-Ar complexes, but the 5p orbitals on the mercury cation are energetically closer to the inner-valence orbitals for RG = Kr–Rn. As such, for those three complexes the inner-valence Hg^+ 5s orbital was frozen, and all others outside of the ECPs (including those on the rare gas) were correlated.

Orbital contour plots were also produced as part of the present work for these complexes: the orbital energies were taken from Hartree-Fock calculations performed at the CCSD(T) level using triple-ζ basis sets of the same designation as those used for the IEC calculations. For the

latter, the equilibrium separation employed was that obtained using the CCSD(T)-extrapolated basis set results. Calculated contours were visualized using MOLDEN.[26]

Finally, as part of the present work, partial atomic charges were obtained using Mulliken populations,[27] natural population analysis (NPA),[28] and the atoms-in-molecules (AIM)[29] theories. For the NPA and AIM analyses, we analysed the density from QCISD calculations performed with Gaussian 09[30] using the same triple-ζ basis sets as just noted. The NPA analysis used the NBO6 software,[31] whilst the AIM analysis used AIMAll. [32]

Table 1-1: Spectroscopic constants for the Group 2 M^+-RG series.[a,b]

	R_e / Å	D_e / cm^{-1}	D_0 / cm^{-1}	ω_e / cm^{-1}	$\omega_e x_e$ / cm^{-1}	B_e / cm^{-1}	α / cm^{-1}	k / N m^{-1}	D_e^{Morse} / D_e
Be^+-He	**2.922**	**133**	**98**	**76.8**	**11.8**	**0.724**	**0.1420**	**0.96**	**0.94**
	2.924	133	98	76.3	11.7	0.723	0.142	0.950	0.94
Be^+-Ne	**2.437**	**424**	**391**	**67.4**	**1.16**	**0.463**	**0.0055**	**1.66**	**2.31**
	2.452	**407**	**375**	**64.5**	**1.06**	**0.456**	**0.0064**	**1.52**	**2.42**
	2.454	407	375	65.2	1.47	0.456	0.00607	1.56	1.78
	(2.462)	(404)	(372)	(65.6)	(1.63)	(0.453)			
Be^+-Ar	**2.086**	**4405**	**4226**	**363.0**	**9.02**	**0.527**	**0.0148**	**57.11**	**0.83**
	2.086	**4401**	**4221**	**363.1**	**9.03**	**0.527**	**0.0148**	**57.13**	**0.83**
	2.084	4428	4248	364.1	8.94	0.528	0.0147	57.4	0.84
	2.0855(6)[c]		*3933(200)*[c]	*362.7(1)*[c]	*8.92(5)*[c]	*0.5271(3)*[c]	*0.0145(3)*[c]		
Be^+-Kr	**2.217**	**6072**	**5891**	**366.0**	**5.90**	**0.421**	**0.0082**	**64.25**	**0.94**
	2.221	6053	5872	365.5	5.82	0.420	0.00816	64.0	0.95
	2.2201			*367.14*[d]	*6.21*[d]	*0.42030*[d]	*0.00821*[d]		
Be^+-Xe	**2.403**	**8273**	**8087**	**373.7**	**4.10**	**0.346**	**0.0049**	**69.42**	**1.03**
	2.407	8239	8054	372.8	4.04	0.345	0.00486	69.0	1.04
				~367[e]	*~3.7*[e]				
Be^+-Rn	**2.482**	**9485**	**9300**	**371.7**	**3.43**	**0.316**	**0.0038**	**70.5**	**1.06**
	2.486	9491	9306	371.0	3.32	0.315	0.00381	70.1	1.10
Mg^+-He	**3.481**	**73**	**51**	**47.4**	**8.50**	**0.413**	**0.0909**	**0.45**	**0.91**
	3.482	73	52	45.8	7.68	0.412	0.0900	0.424	0.95
Mg^+-Ne	**3.119**	**206**	**185**	**43.5**	**2.39**	**0.159**	**0.0103**	**1.22**	**0.96**
	3.147	**203**	**182**	**42.7**	**2.28**	**0.156**	**0.0098**	**1.17**	**0.99**
	3.145	203	182	43.1	2.44	0.157	0.00987	1.19	0.94
	3.17(5)[f]		*96(50)*[f]	*41*[f]					
Mg^+-Ar	**2.825**	**1291**	**1240**	**104.5**	**2.70**	**0.141**	**0.0041**	**9.65**	**0.78**

	R_e / Å	D_e / cm^{-1}	D_0 / cm^{-1}	ω_e / cm^{-1}	$\omega_e x_e$ / cm^{-1}	B_e / cm^{-1}	α / cm^{-1}	k / N m^{-1}	D_e^{Morse} / D_e
	2.825	**1290**	**1238**	**104.7**	**2.68**	**0.141**	**0.0041**	**9.69**	**0.79**
	2.822	1299	1247	104.8	2.53	0.141	0.00407	9.71	0.84
	2.825(7)[g]		*1210(165)*[g]	*96*[g]					
	2.875	**2001**	**1942**	**119.6**	**2.14**	**0.109**	**0.0021**	**15.7**	**0.84**
Mg^+-Kr	2.884	1978	1919	118.4	2.08	0.109	0.00213	15.4	0.85
			1800(600)[g]	*112*[g]					
	3.010	**3012**	**2944**	**135.9**	**1.57**	**0.092**	**0.0012**	**22.1**	**0.98**
Mg^+-Xe	3.018	2973	2906	134.8	1.66	0.0912	0.00123	21.7	0.92
			3300(1700)[g]						
Mg^+-Rn	**3.057**	**3666**	**3595**	**142.1**	**1.41**	**0.083**	**0.0009**	**25.7**	**0.97**
	3.064	3639	3569	141.1	1.41	0.0830	0.000919	25.4	0.97
Ca^+-He	**4.240**	**37**	**24**	**28.8**	**6.16**	**0.264**	**0.0698**	**0.18**	**0.91**
	4.259	36	23	25.6	4.88	0.264	0.00730	0.141	0.93
	3.744	**111**	**100**	**23.2**	**1.10**	**0.091**	**0.0050**	**0.42**	**1.10**
Ca^+-Ne	3.760	109	97	24.8	1.50	0.0889	0.00591	0.484	0.94
	3.70(5)[j]	*115(5)*[j]	*103(5)*[j]	*26(2)*[j]					
	3.108	**877**	**841**	**72.5**	**2.43**	**0.087**	**0.0029**	**6.19**	**0.62**
Ca^+-Ar	3.256	742	712	60.6	1.59	0.0795	0.00255	4.33	0.78
	3.20(0.15)[k]	*810(60)*[k]		*69(2)*[k]					
	3.174	**1376**	**1336**	**79.6**	**1.70**	**0.062**	**0.0013**	**10.12**	**0.68**
Ca^+-Kr	3.305	1200	1160	69.7	1.31	0.0570	0.00116	7.76	0.78
	3.30(0.15)[l]	*1280(80)*[l]		*77(2)*[l]					
	3.330	**2034**	**1991**	**87.1**	**1.17**	**0.050**	**0.0007**	**13.72**	**0.80**
Ca^+-Xe	3.457	1780	1740	78.2	1.03	0.0460	0.00064	11.1	0.83
	3.45(0.15)[m]	*1850(100)*[m]	*1811(80)*[m]	*84(2)*[m]					
Ca^+-Rn	**3.378**	**2493**	**2448**	**89.9**	**0.96**	**0.044**	**0.0005**	**16.1**	**0.85**
	3.487	2190	2150	81.9	0.88	0.0410	0.00046	13.4	0.87
Sr^+-He	**4.524**	**30**	**19**	**24.4**	**5.49**	**0.221**	**0.0609**	**0.13**	**0.90**
	4.547	29	19	21.1	4.12	0.220	0.0652	0.10	0.94
	3.979	**93**	**84**	**18.0**	**0.73**	**0.066**	**0.0032**	**0.31**	**1.20**
Sr^+-Ne	4.005	91	82	19.5	1.11	0.0650	0.00398	0.37	0.94
		77[n]	*67/85*[n]	*19.5(1.5)*[n]	*1.12(0.5)*[n]				
Sr^+-Ar	**3.327**	**712**	**685**	**54.3**	**1.89**	**0.056**	**0.0017**	**4.77**	**0.55**
	3.385	646	623	47.3	1.21	0.0535	0.00162	3.63	0.72

	R_e / Å	D_e / cm^{-1}	D_0 / cm^{-1}	ω_e / cm^{-1}	$\omega_e x_e$ / cm^{-1}	B_e / cm^{-1}	α / cm^{-1}	k / N m^{-1}	D_e^{Morse} / D_e
		830(240)[o]	*800(240)[o]*	*49.5[o]*	*0.75[o]*				
	3.385	**1120**	**1092**	**55.1**	**1.03**	**0.034**	**0.0006**	**7.67**	**0.66**
Sr^+-Kr	3.433	1050	1030	51.1	0.85	0.0333	0.000578	6.62	0.73
		1231[p]	*1200(580)[p]*	*52(1)[p]*	*0.6[p]*				
	3.535	**1660**	**1631**	**58.3**	**0.62**	**0.026**	**0.0003**	**10.56**	**0.83**
Sr^+-Xe	3.591	1560	1530	54.7	0.60	0.0248	0.000278	9.32	0.80
		1970(440)[q]		*54.6[q]*	*0.38[q]*				
Sr^+-Rn	**3.576**	**2052**	**2023**	**58.4**	**0.48**	**0.021**	**0.0002**	**12.65**	**0.86**
	3.617	1910	1910	55.4	0.47	0.0205	0.000177	11.4	0.84
	4.912	**23**	**14**	**19.6**	**4.65**	**0.185**	**0.0545**	**0.09**	**0.91**
Ba^+-He	4.950	22	13	16.7	3.39	0.183	0.0555	0.064	0.95
	[4.921][r]	[22][r]	[14][r]	[17.0][r]	[3.45][r]				
	{4.917}[r]	[r]	[r]	{17.2}[r]	{3.99}[r]				
	4.249	**76**	**69**	**14.6**	**0.64**	**0.054**	**0.0018**	**0.22**	**1.10**
Ba^+-Ne	4.291	73	65	15.1	0.82	0.0529	0.00291	0.24	0.95
	[4.267][r]	[75][r]	[68][r]	[15.4][r]	[0.92][r]				
	{4.246}[r]	{77}[r]	{69}[r]	{15.6}[r]	{0.90}[r]				
	3.319	**811**	**778**	**67.8**	**2.24**	**0.049**	**0.0013**	**8.38**	**0.63**
	3.385	693	664	58.6	2.19	0.0476	0.00147	6.27	0.57
Ba^+-Ar	*3.364[s]*	*680[s]*		*61.7(1.5)[s]*	*2.3(0.2)[s]*		*0.00125[r]*		
	3.47[t]	*~800[t]*							
	[3.339][r]	[766][r]	[734][r]	[65.6][r]	[2.80][r]				
	{3.348}[r]	{752}[r]	{720}[r]	{63.9}[r]	{2.72}[r]				
	3.415	**1215**	**1186**	**59.3**	**0.97**	**0.028**	**0.0004**	**10.83**	**0.75**
Ba^+-Kr	3.479	1093	1066	53.9	1.02	0.0267	0.000428	8.92	0.65
	[3.438][r]	[1175][r]	[1147][r]	[57.8][r]	[1.14][r]				
	{3.446}[r]	{1164}[r]	{1136}[r]	{56.9}[r]	{1.12}[r]				
	3.581	**1731**	**1703**	**56.2**	**0.18**	**0.020**	**0.0002**	**12.52**	**2.57**
Ba^+-Xe	3.653	1569	1543	52.3	0.61	0.0187	0.000192	10.87	0.71
	[3.612][r]	[1672][r]	[1645][r]	[55.3][r]	[0.65][r]				
	{3.621}[r]	{1663}[r]	[1636][r]	[54.6][r]	{0.63}[r]				
Ba^+-Rn	**3.635**	**2100**	**2073**	**53.5**	**0.45**	**0.015**	**0.0001**	**14.36**	**0.76**
	3.709	1916	1892	49.5	0.41	0.0144	0.00011	12.31	0.79
Ra^+-He	**4.871**	**24**	**15**	**20.3**	**4.79**	**0.186**	**0.0536**	**0.10**	**0.90**
	4.885	23	15	17.6	3.55	0.186	0.0553	0.07	0.94
Ra^+-Ne	**4.268**	**79**	**71**	**16.2**	**0.73**	**0.050**	**0.0027**	**0.28**	**1.12**

	R_e / Å	D_e / cm^{-1}	D_0 / cm^{-1}	ω_e / cm^{-1}	$\omega_e x_e$ / cm^{-1}	B_e / cm^{-1}	α / cm^{-1}	k / N m^{-1}	D_e^{Morse} / D_e
Ra^+-Ar	4.276	77	69	16.3	0.92	0.0504	0.00311	0.29	0.95
	3.704	**526**	**507**	**37.5**	**1.14**	**0.036**	**0.0010**	**2.82**	**0.59**
	3.759	486	469	34.3	0.78	0.0351	0.000949	2.36	0.78
Ra^+-Kr	**3.735**	**831**	**813**	**36.8**	**0.64**	**0.020**	**0.0003**	**4.87**	**0.64**
	3.775	793	775	34.9	0.52	0.0193	0.000294	4.40	0.74
Ra^+-Xe	**3.871**	**1235**	**1216**	**37.6**	**0.42**	**0.014**	**0.0001**	**6.93**	**0.68**
	3.917	1170	1160	35.9	0.35	0.0132	0.000127	6.33	0.78
Ra^+-Rn	**3.897**	**1546**	**1528**	**35.8**	**0.15**	**0.010**	**0.0001**	**8.48**	**1.34**
	3.944	1470	1450	34.6	0.25	0.00967	0.000069	7.89	0.82

[a] R_e is the equilibrium bond length, D_e and D_0 are the equilibrium and zero point dissociation energies respectively, ω_e is the harmonic vibrational frequency, $\omega_e x_e$ is the anharmonicity constant, B_e the rotational constant, α the vibration-rotation constant, k the force constant from Hooke's law, and D_e^{Morse} is the Morse estimate of the dissociation energy, given by $\omega_e^2/4\omega_e x_e$. The most prevalent naturally-occurring isotope was used in all cases.

[b] A bold value indicates a value from the present work, with a bold, underlined value indicating a value obtained with a doubly-augmented basis set from the present work (see text). A normal value indicates one previously published by us (see text) and a value in italics indicates an experimental value.

[c] Ref. 33. [d] Ref. 34. [e] Ref. 35. [f] R_0 value, Ref. 36. [g] R_0 value, Refs. 37 and 38. [h] Ref. 38. [i] Ref. 38.[j] Ref. 39. [k] Refs. 40, 41, 42 and 43. [l] Refs. 40, 41 and 42. [m] Refs. 40, 41 and 42. [n] Ref. 44. [o] Ref. 45. [p] Ref. 46. [q] Ref. 47. [r] Ref. 48. Values in square brackets are the non-small core ECP/CBS results and values in braces are the non-small core ECP/BF/C5Z results from Ref. 48 (see Table IV in that work). [s] Ref. 49. [t] Ref. 50.

1.3 Results and Discussion

1.3.1 IECs and Spectroscopic Constants

The IECs are plotted in Figure 1-1 for the Group 2 M^+-RG complexes, and in Figure 1-2 for the Group 12 M^+-RG complexes. Full interaction energy curves are provided as Supplementary Material in Ref. 51 for all of the species. A summary of the derived spectroscopic constants obtained from the IECs are provided in Table 1-1 for the Group 2 complexes, and Table 1-2 for the Group 12 complexes. The key experimental data[33-47,49,50,52-54] is displayed in Table 1-1 and Table 1-2, as well as comparisons between the present and our previous work. Since these complexes have been previously studied using subsets of the approaches taken here, and in

those studies the generally very good agreement between previous theoretical and experimental work was seen,[6-9,12,13] a full survey of previous experimental and theoretical studies is not repeated herein. In most cases, those experimental results are spectroscopic studies and it was possible to compare to the calculated spectroscopic constants. The previous IECs for the titular species from the Wright group at Nottingham were also used to calculate ion transport coefficients and this provided another avenue of comparison by which to evaluate the quality of the calculated potentials via ion transport studies of metal cations moving through a bath of rare gas. [7-9,12,13] Some comment will, however, be made on several studies that have been published since that earlier work. In Ref. 9, the experimental rotational constants were compared to vibrational constants and an excellent agreement was obtained. There, the v = 0, 1 and 2 energies were used to derive the standard Morse (ω_e and $\omega_e x_e$) constants; and B_0 and B_1 values to obtain the B_e and α parameters – this method mimics that used in a spectroscopic experiment. In the present work, it is noted that R_e and D_e can be obtained from the interpolated IEC from the LEVEL program. The R_e value allows the calculation of B_e and together with B_0, α can be obtained; similarly, with D_e and the v = 0 and 1 energies, the Morse vibrational constants can be obtained. This latter approach should be more representative of the lowest regions of an IEC and so more representative of the curvature there – the results are reported from this approach in Table 1-1 and Table 1-2. As an example, for Be^+-He, B_e = 0.7189 cm^{-1} and α = 0.1175 cm^{-1} are obtained from the latter approach, but the corresponding values are 0.7242 cm^{-1} and 0.1420 cm^{-1} using the former. The differences between the two approaches become less marked as the well depth increases, as expected. Even though these two slightly different methods have been used to obtain the spectroscopic constants, the agreement of the present results with our previous calculated values, and the limited available experimental spectroscopic ones, is excellent (see Table 1-1).

Table 1-2: Spectroscopic constants for the Group 12 M^+-RG series.[a, b]

	R_e / Å	D_e / cm^{-1}	D_0 / cm^{-1}	ω_e / cm^{-1}	$\omega_e x_e$ / cm^{-1}	B_e / cm^{-1}	α / cm^{-1}	k / Nm^{-1}	D_e^{Morse} / D_e
Zn^+-He	**3.014**	**131**	**99**	**68.8**	**10.01**	**0.498**	**0.0861**	**1.05**	**0.90**
	3.03	125.3	94	63.0	8.36	0.487		0.88	0.95
Zn^+-Ne	**2.807**	**348**	**320**	**58.6**	**2.84**	**0.141**	**0.0075**	**3.09**	**0.87**
	2.86	325.4	298	55.5	2.62	0.135		2.76	0.90
Zn^+-Ar	**2.627**	**2062**	**2002**	**119.7**	**2.04**	**0.099**	**0.0018**	**20.8**	**0.85**
	2.64	1977	1918	120.7	2.14	0.098		21.1	0.86
Zn^+-Kr	**2.656**	**3291**	**3229**	**123.6**	**1.25**	**0.066**	**0.0007**	**32.7**	**0.93**
	2.67	3192	3132	120.3	1.22	0.065		30.9	0.93
Zn^+-Xe	**2.759**	**5197**	**5131**	**132.3**	**0.81**	**0.052**	**0.0004**	**44.4**	**0.93**
	2.77	5088	5023	129.9	0.79	0.051		42.8	1.05
Zn^+-Rn	**2.806**	**6372**	**6307**	**130.9**	**0.68**	**0.043**	**0.0002**	**50.1**	**0.99**
	2.81	6285	6221	128.6	0.60	0.043		48.4	1.10
Cd^+-He	**3.204**	**114**	**85**	**63.2**	**9.88**	**0.429**	**0.0775**	**0.91**	**0.89**
	3.24	108		59.4	8.85	0.415		0.80	0.92
Cd^+-Ne	**3.022**	**297**	**272**	**52.1**	**2.72**	**0.109**	**0.0058**	**2.72**	**0.84**
	3.07	276		48.9	2.47	0.105		2.40	0.88
Cd^+-Ar	**2.914**	**1497**	**1452**	**89.8**	**1.61**	**0.067**	**0.0012**	**14.0**	**0.83**
	2.94	1408		86.5	1.55	0.066		13.0	0.86
Cd^+-Kr	**2.922**	**2390**	**2346**	**89.2**	**0.94**	**0.041**	**0.0004**	**22.6**	**0.88**
	2.96	2260		85.6	0.92	0.040		20.9	0.88
Cd^+-Xe	**2.995**	**3886**	**3838**	**96.3**	**0.60**	**0.031**	**0.0002**	**33.4**	**1.00**
	3.03	3705		93.2	0.60	0.030		31.3	0.98
Cd^+-Rn	**3.025**	**4870**	**4823**	**94.3**	**0.43**	**0.024**	**0.0001**	**39.4**	**1.05**
	3.06	4763		92.0	0.43	0.024		37.5	1.03
Hg^+-He	**3.077**	**149**	**113**	**78.7**	**11.78**	**0.458**	**0.0761**	**1.43**	**0.88**
	3.12	138		71.9	10.30	0.441		1.20	0.91
	3.10	144		74.3	10.55				

	R_e / Å	D_e / cm^{-1}	D_0 / cm^{-1}	ω_e / cm^{-1}	$\omega_e x_e$ / cm^{-1}	B_e / cm^{-1}	α / cm^{-1}	k / Nm^{-1}	D_e^{Morse} / D_e
Hg^+-Ne	**3.002**	**351**	**322**	**60.3**	**3.09**	**0.103**	**0.0050**	**3.90**	**0.84**
	3.06	316		54.8	2.77	0.099		3.22	0.86
	3.04	334		27.0	2.81				
	2.98(3)[c]	*346*[c]		*57.8(1.0)*[c]					
Hg^+-Ar	**2.876**	**1802**	**1754**	**97.4**	**1.35**	**0.061**	**0.0009**	**18.7**	**0.98**
	2.91	1650		92.9	1.49	0.060		17.0	0.88
	2.90	1720		95.4	1.50				
	2.868[d]	*1630(100)*[d]		*99.0*	*1.5*				
Hg^+-Kr	**2.856**	**3111**	**3062**	**97.1**	**0.85**	**0.035**	**0.0003**	**32.9**	**0.89**
	2.89	3867		92.0	0.80	0.034		29.6	0.68
Hg^+-Xe	**2.905**	**5546**	**5494**	**104.1**	**0.42**	**0.025**	**0.0001**	**50.9**	**1.17**
	2.95	5237		100.7	0.44	0.024		47.7	1.10
Hg^+-Rn	**2.938**	**7140**	**7091**	**98.2**	**0.42**	**0.019**	**0.0001**	**60.1**	**0.80**
	2.98	6997		95.2	0.27	0.018		56.5	1.20

[a] R_e is the equilibrium bond length, D_e and D_0 are the equilibrium and zero point dissociation energies respectively, ω_e is the harmonic vibrational frequency, $\omega_e x_e$ is the anharmonicity constant, B_e the rotational constant, α the vibration-rotation constant, k the force constant from Hooke's law, and D_e^{Morse} is the Morse estimate of the dissociation energy, given by $\omega_e^2/4\omega_e x_e$. The most prevalent naturally-occurring isotope was used in all cases.

[b] A bold value indicates a value from the present work, with a bold, underlined value indicating a value obtained with a doubly-augmented basis set from the present work (see text). A normal value indicates one previously published by us (see text) and a value in italics indicates an experimental value.

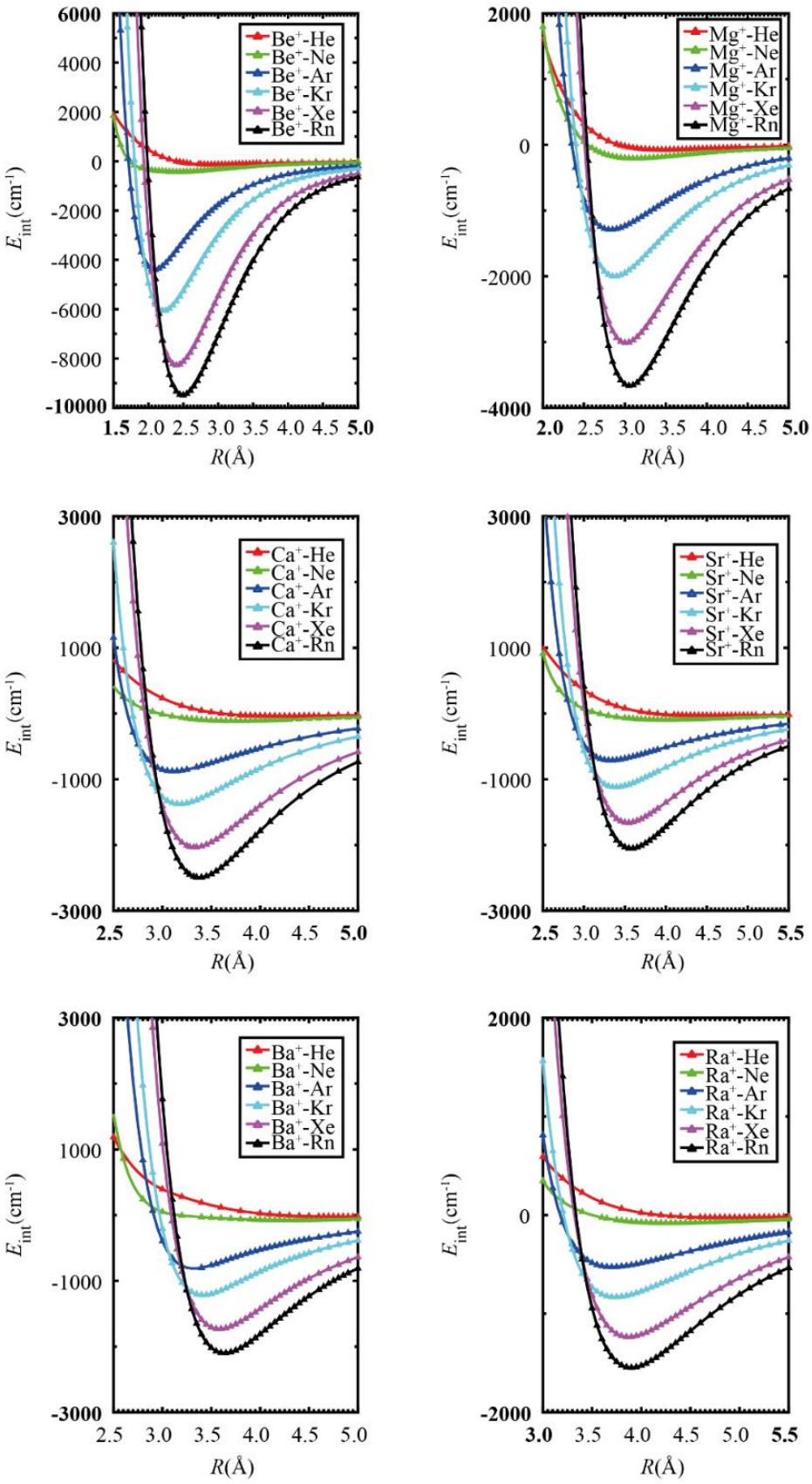


Figure 1-1. Interaction energy curves for the Group 2 M^+-RG complexes.

In Ref. 9, calculations were run with doubly-augmented basis sets. Here, for Be^+-Ne, sets of calculations were run with singly- doubly- and triply-augmented basis sets, with the latter obtained in an even-tempered way from the former. It was found that the double-augmentation gave results that were significantly different from the singly-augmented ones, while the triple augmentation essentially gave no further improvement. Thus, for Be^+-Ne it is concluded that doubly-augmented basis sets are required to give converged results and these are the ones presented in Table 1-1. With this in mind, the same set of calculations for Be^+-Ar were also performed, and obtained no further improvement over the singly-augmented basis set, and so use the latter results in further analyses. In fact, double augmentation of the basis set was only important for the Be^+-Ne and Mg^+-Ne species.

Table 1-1 shows selected available experimental results for $M^+ = Mg^+$, Ca^+, Sr^+ and Ba^+; there are no experimental data for $M^+ = Ra^+$. Generally the close agreement between the previous and present spectroscopic parameters means that the previous comments[7,8] apply. It is aware that only a few studies published on the Group 2 M^+-RG complexes subsequent to our previous work.[9] Three of these are focused on a single Group 2 M^+-RG complex, Be^+-Ar[55], Be^+-Kr[56] and Ba^+-Xe[57]; while a more recent study tackled the Ba^+-RG series, for RG = He–Xe.[48] The very recent study on Be^+-Ar by Niu et al. [55] used CASSCF/icMRCI+Q calculations in conjunction with both triple- and quadruple-ζ quality Dunning-style basis sets, allowing extrapolation to the basis set limit. Several electronic states were calculated and spectroscopic constants derived for each state. For the ground state, D_e was reported as ~4030 cm^{-1}, which is significantly lower than the values obtained in the present and previous work of the Wright group at Nottingham; [9] the agreement in R_e is fairly good, albeit with a shorter value of 2.065 Å compared to that reported here, with value being in excellent agreement with that of the previous spectroscopic study done by the Wright group at Nottingham[33] of 2.086 Å. We note that the given units (cm^{-1}) for the D_e value in Ref. 55 are incorrect, and should be eV; converting the given value to cm^{-1} then yields a value of 4379 cm^{-1}, which is in fairly good agreement with the present value, albeit lower. Other given spectroscopic constants are also in fairly good agreement, but our values are in excellent agreement with experiment throughout. On the other hand, for Be^+-Kr, the D_e value in Ref. 56 of 6180 cm^{-1} is slightly larger than the value obtained here, while the R_e value of 2.232 Å is slightly longer than present value and the spectroscopic value[34] – see Table 1-1. With regard to the other constants, ω_e and B_e agree well, but $\omega_e x_e$ and α are in somewhat poorer agreement with our previous and spectroscopic values. It is concluded that the MRCI calculations of Ref. 56 are somewhat compromised in their

description of the $X^2\Sigma^+$ ground state, owing to their state-averaged nature; additionally, the basis sets used in the present work are larger, making the extrapolation to the basis set limit more reliable.

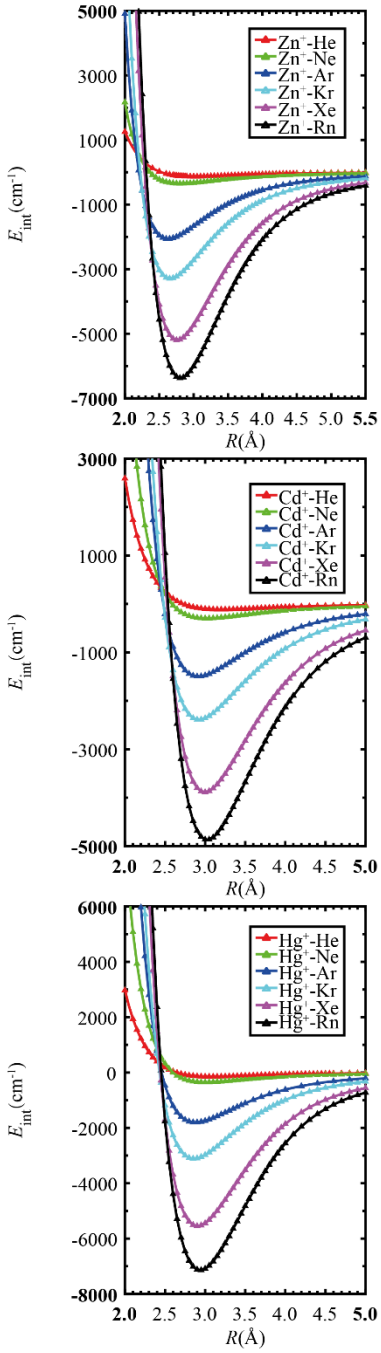


Figure 1-2. Interaction energy curves for the Group 12 M+ RG complexes.

The study on Be^+-Xe by Abdessalem et al, [57] used a pseudopotential plus core-polarization function for the Ba^{2+}-Xe 'core' with the lone 6s electron being treated by configuration interaction to calculate several electronic states of Ba^+-Xe (and Ba-Xe). For the ground state

of Ba^+-Xe, the reported spectroscopic constants showed poor agreement with our equilibrium separation, with their value being 3.77 Å compared to the present CCSD(T) result of 3.581 Å. Similarly poor agreement is seen in the values for D_e, as the value reported by Abdessalem is 1971 cm^{-1}, significantly higher than the present result of 1731 cm^{-1}.

Very recently, Buchachenko and Viehland[48] studied the Ba^+-RG series as part of a wider study of the interactions of the rare gases with neutral, singly- and doubly-charged barium atoms. A range of different basis sets were employed, with the calculations being carried out at the RCCSD(T) level. Various sizes of Dunning-type basis sets were employed, with and without bond functions; additionally, for the cases where an ECP was employed, small-core versions were also tried. These calculations are very similar to those employed here: the RCCSD(T) method ,and the corresponding Dunning-type basis sets, and small-core ECPS were also employed. Extrapolation to the basis set limit was performed in Ref. 48, with and without bond functions, but not with the small-core ECPs. In addition, the radon-containing complexes were not considered. When comparing the results in Table 1-1 to those in Ref. 48, excellent agreement is found for both R_e and D_e for each of Ba^+-He and Ba^+-Ne, with the extrapolated results that employed the non-bond function basis sets, while for RG = Ar–Xe, our R_e values are slightly shorter and the D_e values slightly larger. The decreasing trend of R_e and the increasing trend of D_e with improvements in the basis set in Ref. 48, suggests that the present results are likely the more reliable. There are spectroscopic and transport data for Ba^+-Ar (see Table 1-1). The agreement for R_e from Ref. 48 is slightly closer to the experimental value, but the values of the dissociation energy from Ref. 48 and the present value suggest the spectroscopic estimate[49] is a little low, and that the transport value[50] is more in line with the calculated values. With regard to the vibrational parameters, the ω_e value from Ref. [48] is in slightly better agreement with experiment, while the present $\omega_e x_e$ is better. Overall the results from the present study and those of Ref. 48 appear to be of a similar reliability.

Note that the $\omega_e x_e$ value for Ba^+-Xe is significantly smaller than that from our previous work[7] and also that from Ref. 48. This was checked, and it was found that values from the two unextrapolated potentials are in good agreement with the previous values, but the extrapolation leads to this smaller value; since there are no experimental data for this complex, further evaluation cannot be made.

No studies subsequent to previous work done by the Wright group at Nottingham[12,13] seem to have been published for $M^+ = Zn^+$–Hg^+.

1.3.2 Reduced Potentials

It is difficult to compare the bonding directly from the IECs, since the binding energies are very different and changes to the shapes of the curves are not apparent. In Figure 1-3 and Figure 1-4 reduced potential plots are shown,[58-61] where the interaction energies are normalized to D_e and the internuclear separations to R_e, making any difference in the shapes of the IECs more evident. Such plots are expected to be close to each other for a family of species, if the interactions are similar; any differences can be attributed to differences in the interactions, and so give information on whether a universal diatomic potential function exists.[62,63] As may be seen for the Group 2 M^+-RG complexes, the M^+-Ne curves are markedly different from the others, being significantly flatter. such plots for Be^+-RG and Mg^+-RG were examined in Ref. 9. There it was noted that Be^+-Ne was unusual; however, it is clear from Figure 1-3 that the M^+-Ne species are somewhat out of line for all of the Group 2 complexes. In contrast, the reduced potentials for the Group 12 M^+-RG species in Figure 1-4 are all somewhat similar. The implication from the reduced potential plots is that the repulsive region of the Group 2 M^+-Ne complexes is comparatively softer than at R_e than for the other species, and particularly so for Be^+-Ne –more details about this point will be mentioned later.

Another way of examining the interactions is via the κ parameter[59] (which is essentially the Sutherland parameter put forward in 1938)[64], which has been termed the "reduced curvature of the potential at R_e", [59] and may be expressed as:

$$\kappa = \omega_e^2/2B_eD_e \qquad \text{Eqn. 1-1}$$

The κ values for the Group 2 and Group 12 M^+-RG complexes are given in Table 1-3 and plotted in Figure 1-5. It may be seen that the Group 2 M^+-Ne complexes have κ values that are significantly different to the other species, in line with their different reduced potentials. In contrast, for the Group 12 M^+-RG complexes, the κ values fall in a narrower range, although the values for Hg^+-RG are somewhat more erratic. Winn[59] has noted that κ values in the range 0–20 are indicative of strong chemical bonding, which would seem to include Be^+-Ne, with the heavier Be^+-RG complexes having values close to this range. This does not fit with the weak binding in these complexes and indicates that κ values should only be used in a comparative way within groups of similar species, rather than as a global indicator. For the Group 2 complexes, there is an overall increase and plateauing of the κ values as the atomic number of M^+ increases, with the Ba^+-containing complexes being unusual. With regard to the atomic

number of RG, there is a fall from He to Ne for all complexes. There is then a gradual rise and plateauing for the other RG atoms when $M^+ = Mg^+–Sr^+$ and Ra^+, while the Be^+-RG and Ba^+-RG complexes have the opposite trend for RG = Ar–Rn.

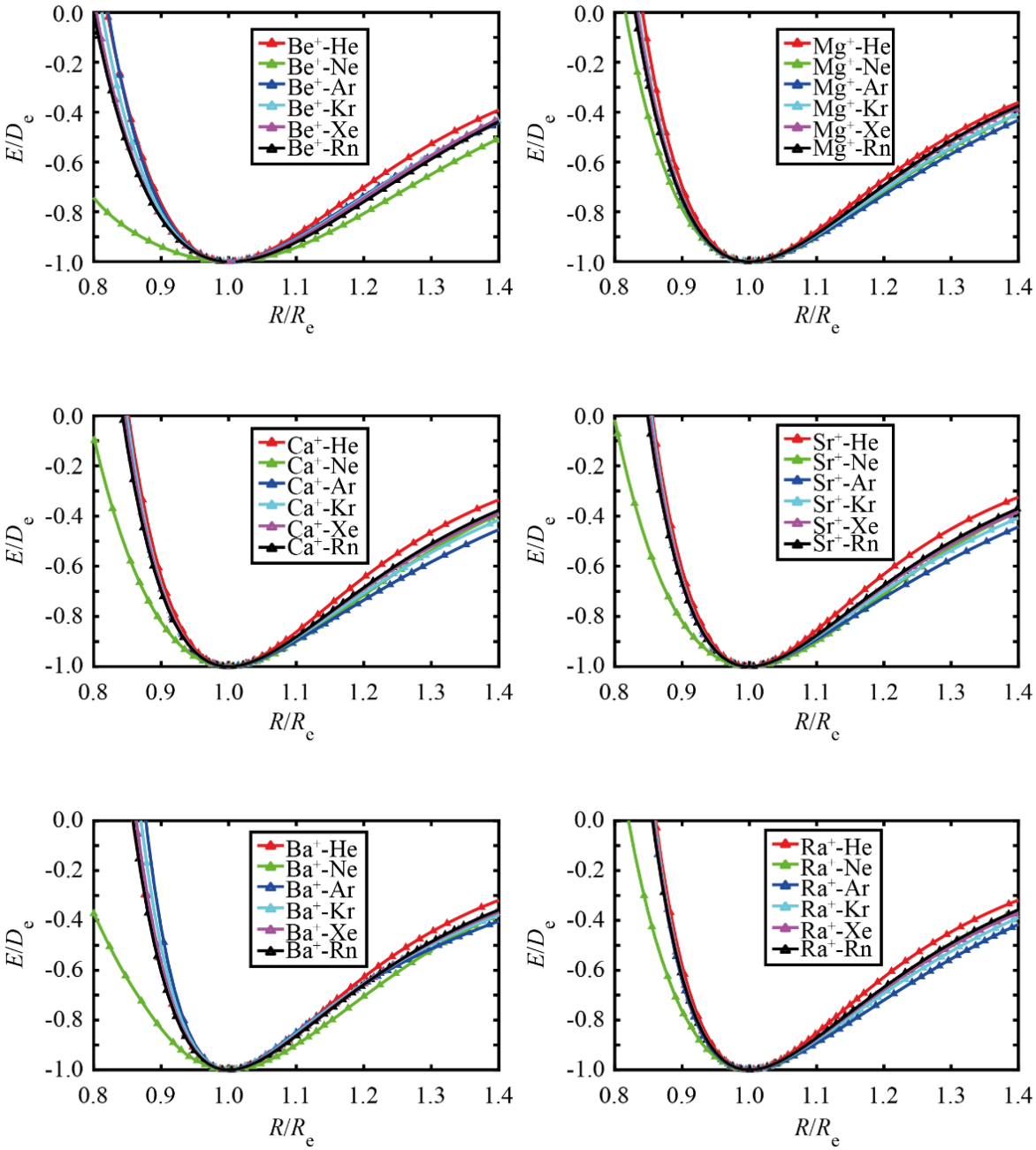


Figure 1-3. Reduced potentials for the Group 2 M^+-RG complexes.

For the Group 12 species, there is a rise of κ with the atomic number of M^+. Additionally, there is an overall fall in κ with the atomic number of RG, although the trend is somewhat erratic. It is interesting to note that for RG = Ar–Rn, the Be^+-RG and Ba^+-RG trends are similar to those of the corresponding Group 12 species.

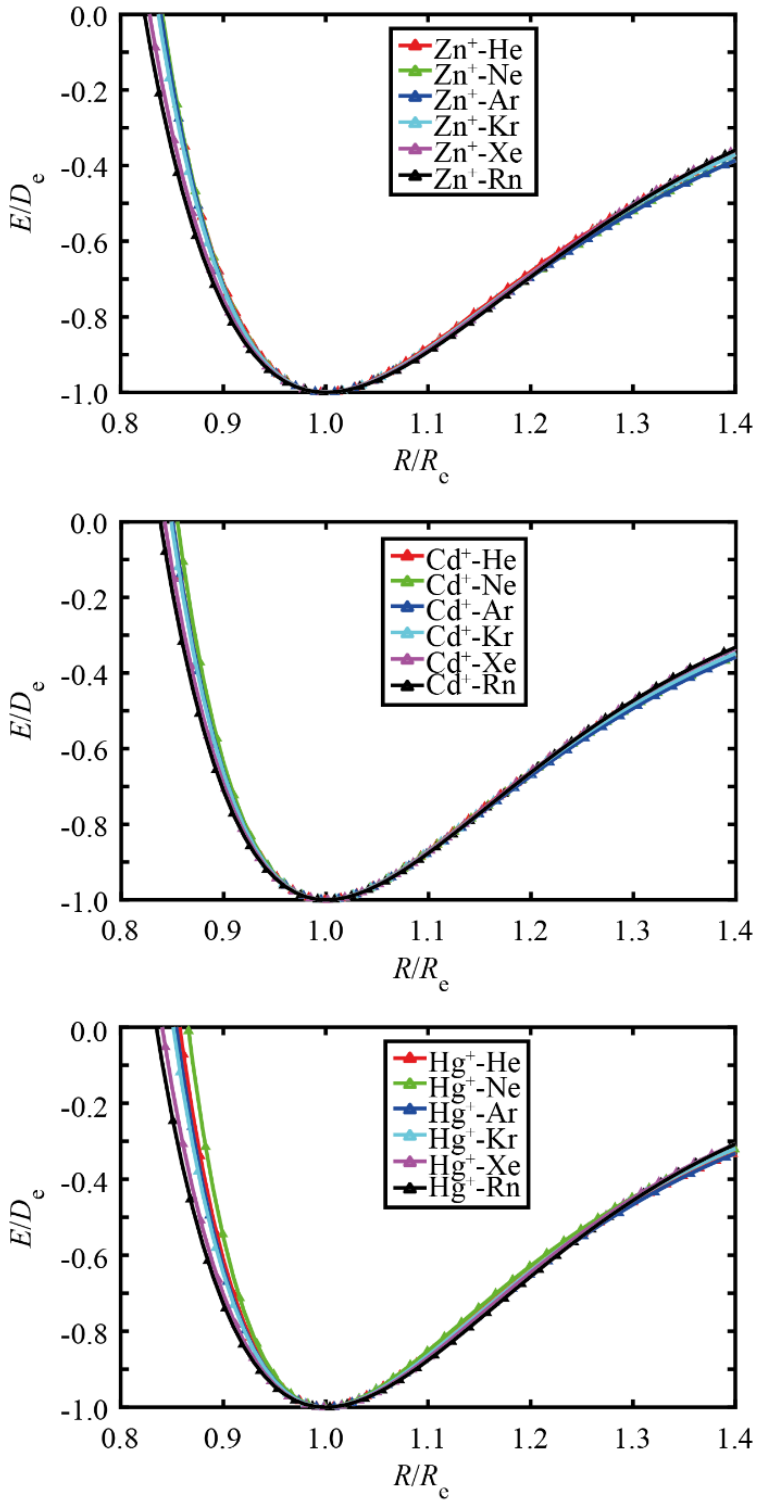


Figure 1-4. Reduced potentials for the Group 12 M^+-RG complexes.

Overall, the κ parameter has limited use, and the reduced potential plots themselves seem more transparent in highlighting differences in the interactions. A further comment is made on the κ

parameter at the end of the following subsection.

Table 1-3: κ values (see Eqn. 1-1) for the Group 2 and Group 12 M^+-RG Complexes

M	M^+-He	M^+-Ne	M^+-Ar	M^+-Kr	M^+-Xe	M^+-Rn
			Group 2			
Be	31.1	11.7	28.4	26.2	24.4	23.1
Mg	38.0	29.3	30.0	32.7	33.4	33.0
Ca	43.3	26.7	34.3	37.3	37.4	37.1
Sr	46.0	26.7	37.3	39.5	40.0	39.7
Ba	47.1	26.2	57.3	52.3	46.7	45.5
Ra	48.0	32.8	37.0	41.2	42.4	41.9
			Group 12			
Zn	36.6	35.1	35.0	35.2	32.8	31.2
Cd	41.3	41.4	40.1	40.7	38.8	37.3
Hg	45.8	50.4	43.1	43.5	39.0	36.6

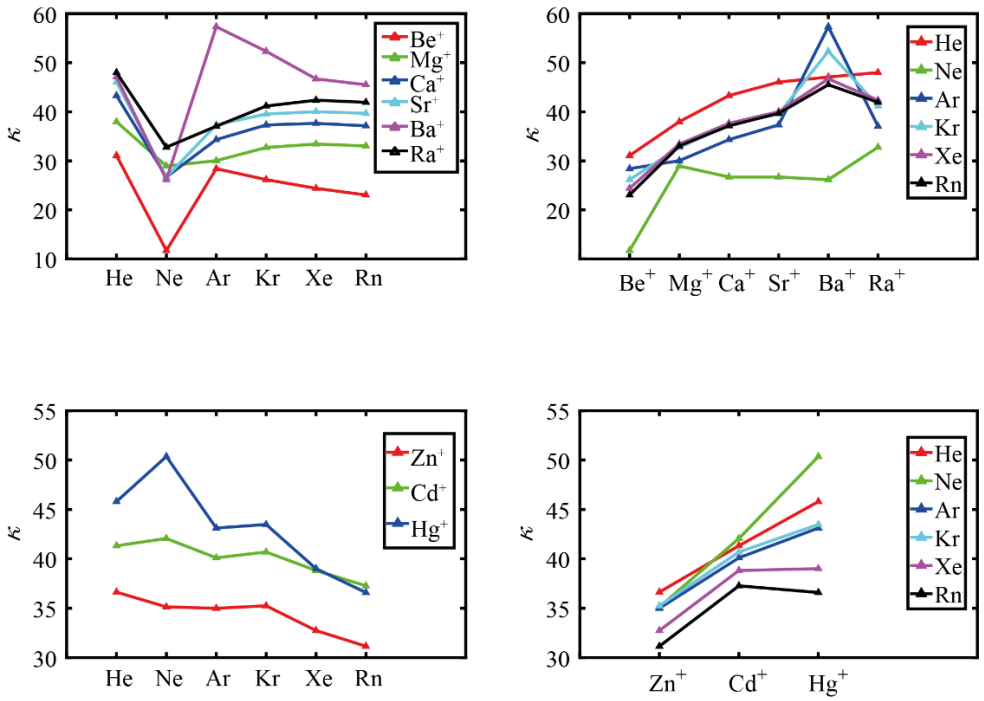


Figure 1-5. Plots of κ (see Eqn. 1-1) for Group 2 and Group 12 M^+-RG complexes.

1.3.3 Trends in the Spectroscopic Constants of the Group 2 M^+-RG Series

Equilibrium Internuclear Separations

The R_e values for the Group 2 and 12 M^+-RG are plotted in Figure 1-6 to allow an examination of trends in the values. First, it is clear (see also Table 1-1 and Table 1-2) that the Group 12 species generally have shorter bond lengths than their corresponding Group 2 counterparts along the same row of the Periodic Table. Next, for the same RG atom, the R_e values generally show an overall increase with increasing atomic number of the metal cation for the Group 2 M^+-RG complexes. This increase is mostly monotonic with the increasing atomic number of the metal, but for RG = Ar–Rn, a small dip is seen at Ba^+.

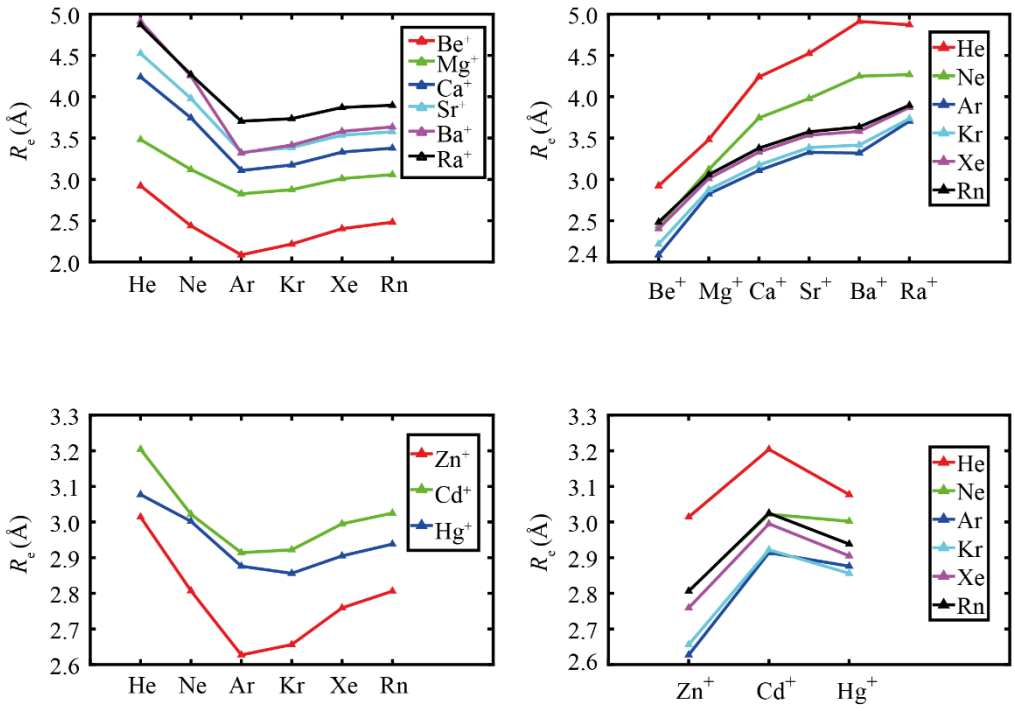


Figure 1-6. Trends in R_e for the Group 2 and Group 12 M^+-RG complexes.

Examining now the trends throughout each M^+-RG series as the rare gas atom is changed, for the Group 2 species a uniform behaviour is seen for all series, marked by a decrease from RG = He through Ar, followed by an increase thereafter. This is interpreted in terms of a subtle balance between the attractive and repulsive terms. From helium through argon, the rate at which the attractive terms increase with R evidently outpaces the increase in repulsive terms, leading to successively contracting bond lengths. From argon onwards, however, the repulsive terms are seen to be becoming relatively more important and so the equilibrium separations increase in response. It is clearly surprising that there is the fall from He to Ar, since the RG

atom is becoming larger; this will be linked to hybridisation below, which allows electron density between the RG atom and the M^+ to be lowered. In so doing, the RG atom can move closer and so gains are made in the attractive electrostatic energy terms. This suggests that even for the weakly polarizable Ne there is an energy gain involved in this process and this continues for the larger (and more polarizable) Ar atom systems. It appears that this process has a limit, however, as for Kr–Rn the rise is shallower. One rationale for this is an increase in the electron repulsion terms as the electron density increases in regions away from the internuclear zone. Hence, further energy gains from moving the RG atom closer to M^+ are not sufficient to overcome this, even with the larger and more polarizable RG atoms, as their proximity to the cation will be limited by their increasing size and additional repulsion from the greater number of RG electrons.

For the same RG atom, the M^+-RG complexes involving the Group 12 metals all show similar behaviour, in that the Cd^+-RG complexes show the longest bond lengths in each case and the Zn^+-RG complexes the shortest, with the Hg^+-RG bond lengths close to those of Zn^+-RG for the lighter RG atoms. A rationale for this arises through consideration of the ionic radii of the metal cations, for example using the Wright-Breckenridge radius, R_{WB},[65] whereby the ionic radius of a cation is found by subtracting half the He_2 dimer equilibrium separation, (1.49 Å) from the value of M^+–He. For the Group 12 metal cations, this treatment leads to the ordering of the ionic radii being $Cd^+ > Hg^+ \gtrsim Zn^+$ – a result which is in line with the lanthanide contraction experienced by mercury, and accounts for the observed trends.

Examining each Group 12 M^+-RG series for a fixed M^+, a rather different picture is seen, which is similar to the trends seen for the Group 2 complexes, albeit less pronounced. For all three series, there is an initial decrease in bond length as the atomic number of the rare gas increases, followed by a rise for the heavier rare gases, with the turning point being at M^+-Ar for Zn^+-RG and Cd^+-RG but at Kr for Hg^+-RG. The same explanation given above for the Group 2 species is applicable, in that there is a delicate balance between the attractive and repulsive terms in each complex.

Dissociation Energies and k

In Figure 1-7 the D_e values are plotted for the Groups 2 and 12 M^+-RG, and it may immediately be seen that the Group 12 (M^+=Zn^+–Hg^+) species have larger dissociation energies than their corresponding Group 2 (Ca^+–Ba^+) counterparts.

There is a general trend in the D_e values of decreasing dissociation energy with increasing

atomic number and size of the metal cation, this is in line with the leading term, $-\alpha/2R^4$, of the ion/induced-dipole interaction. In the case of the lightest two rare gases, there are much sharper decreases in interaction energy seen for the lighter metal cations which eventually give way to the more-slowly changing interaction energies for $M^+ = Ca^+–Ra^+$. Notably there is a very small increase in dissociation energy at Ba^+-RG.

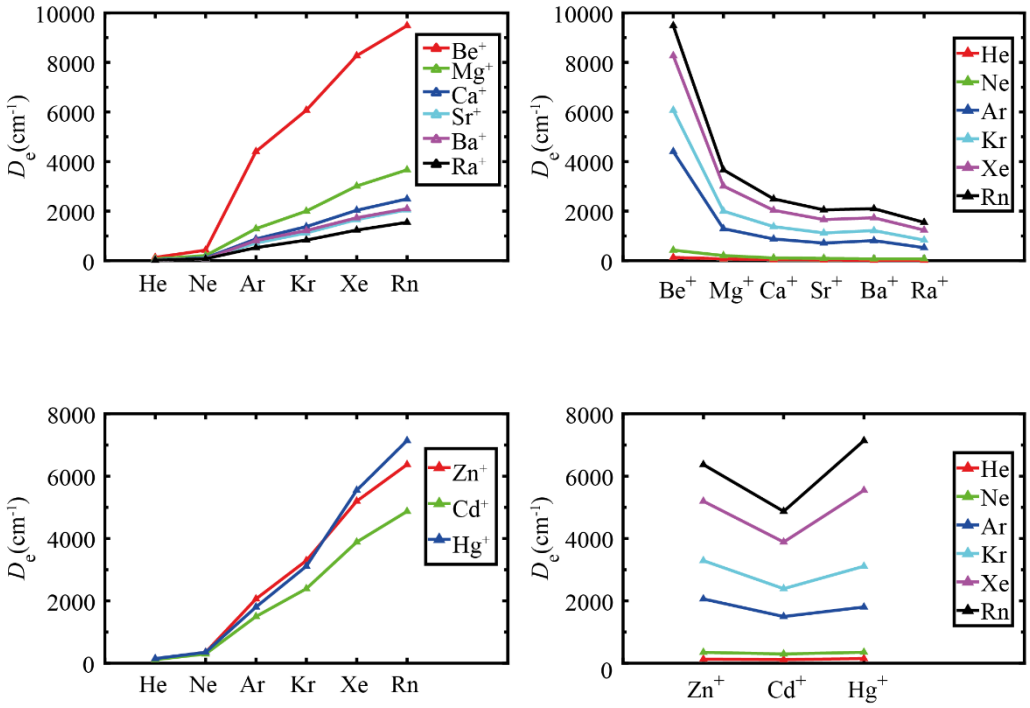


Figure 1-7. Trends in D_e for the Group 2 and Group 12 M^+-RG complexes.

For the heavier rare gases, the interaction energies are generally much higher than for the He and Ne analogues and the rise is particularly steep for Be^+-RG. The explanation of this is the small size of Be^+, which allows the close approach of RG and so a significant increase in the attractive electrostatic terms, in particular the leading term, $-\alpha/2R^4$.

Trends for the harmonic vibrational frequencies, ω_e, are usually generally less clear since the harmonic vibrational frequencies are a consequence of two main effects: the electronic interaction and the reduced mass of each system. Hence the trends in the force constant obtained from Hooke's law, k is worth to focus on, and these are plotted in Figure 1-8 for the Group 12 M^+-RG complexes and the corresponding Group 2 ones that are in the same row of the Periodic Table. The trends in k are very similar to those in D_e, as might be expected.

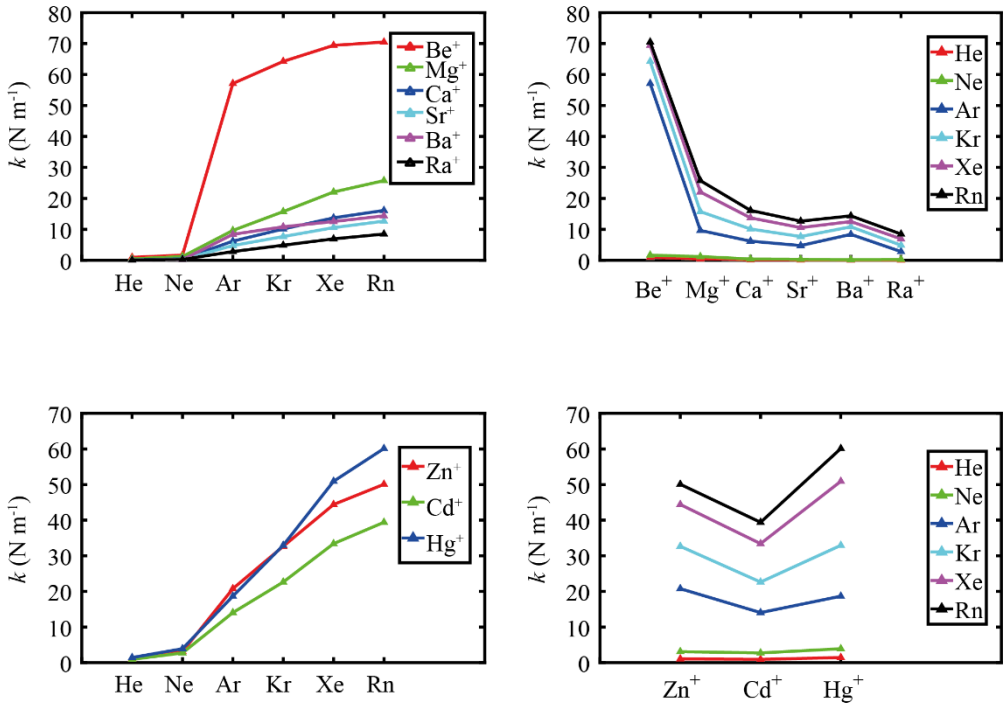


Figure 1-8. Trends in k for the Group 2 and Group 12 M^+-RG complexes.

Comment on κ

It was noted above that the κ parameter was quantitatively not very indicative of the bonding in these species. It may be seen from its definition (Eqn. 1-1) that it depends on ω_e, R_e (via B_e) and D_e. It has been noted in the above subsections that the variation in these parameters can be quite marked and is not always monotonic. As such, the κ parameter depends on different aspects of the interaction, both at R_e and at the dissociation asymptote; when considering Birge-Sponer plots and discuss the contour plots of the molecular orbitals, it will become more obvious that linking κ to the strength of bonding is simplistic.

1.3.4 Molecular Orbital Diagrams and Contour Plots

In discussing the interactions in the M^+-RG complexes, it will be useful to refer to the energies of some of the lowest M^+ excited states, which are presented in Table 1-4 taken from Ref. 66.

Be^+-RG and Mg^+-RG.

Shown in Figure 1-9 are molecular orbital diagrams and associated contour plots for Be^+-RG and Mg^+-RG (RG = He, Ar and Xe). For all RG, ϕ_1 corresponds largely to the outermost *n*s orbital on RG – it appears at a significantly lower energy in the complex than on the isolated

RG atom, since in the cationic complex it experiences the coulombic field from M^+, which lowers its energy, but this is ameliorated by e^-–e^- repulsion. In the case of M^+-He, it can be seen that ϕ_2 is largely the outermost *n*s orbital on M^+ and is at almost the same energy in the complex and in the atomic cation. For RG = Ar and Xe the situation is a little more complicated as there are now four molecular orbitals made up from the interactions between the outermost *n*s orbital on M^+ and the outermost *n*p orbitals on RG. (The expected small contributions are neglected from the outermost *n*s orbital on RG.) Note that there will be a loss of degeneracy of the three MOs that largely correspond to the three RG *n*p orbitals (ϕ_2–ϕ_4) from the interaction with the positive charge on M^+. Further deviations may then occur as a result of covalency, which will be accompanied by a concomitant rise in the energy of ϕ_5 from the atomic energy of the outermost *n*s orbital on M^+, making this orbital antibonding in nature.

Table 1-4: Energies (cm^{-1}) of the excited s^0p^1, d^9s^2 and s^0d^1 states of the Group 2 and Group 12 cations[a,b]

M^+	ns^0np^1	$(n\text{-}1)d^9ns^2$	ns^1nd^1
		Group 2	
Be^+	31933		98055
Mg^+	35730		71491
Ca^+	25340		13687
Sr^+	24250		14724
Ba^+	21389		5354
Ra^+	24590		13079
		Group 12	
Zn^+	49064	64354	96940
Cd^+	45791	72640	89782
Hg^+	57568	44539	105320

[a] Data taken from Ref. 66.

[b] Non-spin-orbit split energies, derived from the energies of the spin-orbit levels, assuming the latter are located at $E_0 = \frac{1}{2}\zeta[j(j+1) - l(l+1) - s(s+1)]$, where E_0 is the non-spin-orbit split energy, ζ is the spin-orbit coupling constant and *j*, *l* and *s* have their usual meanings.

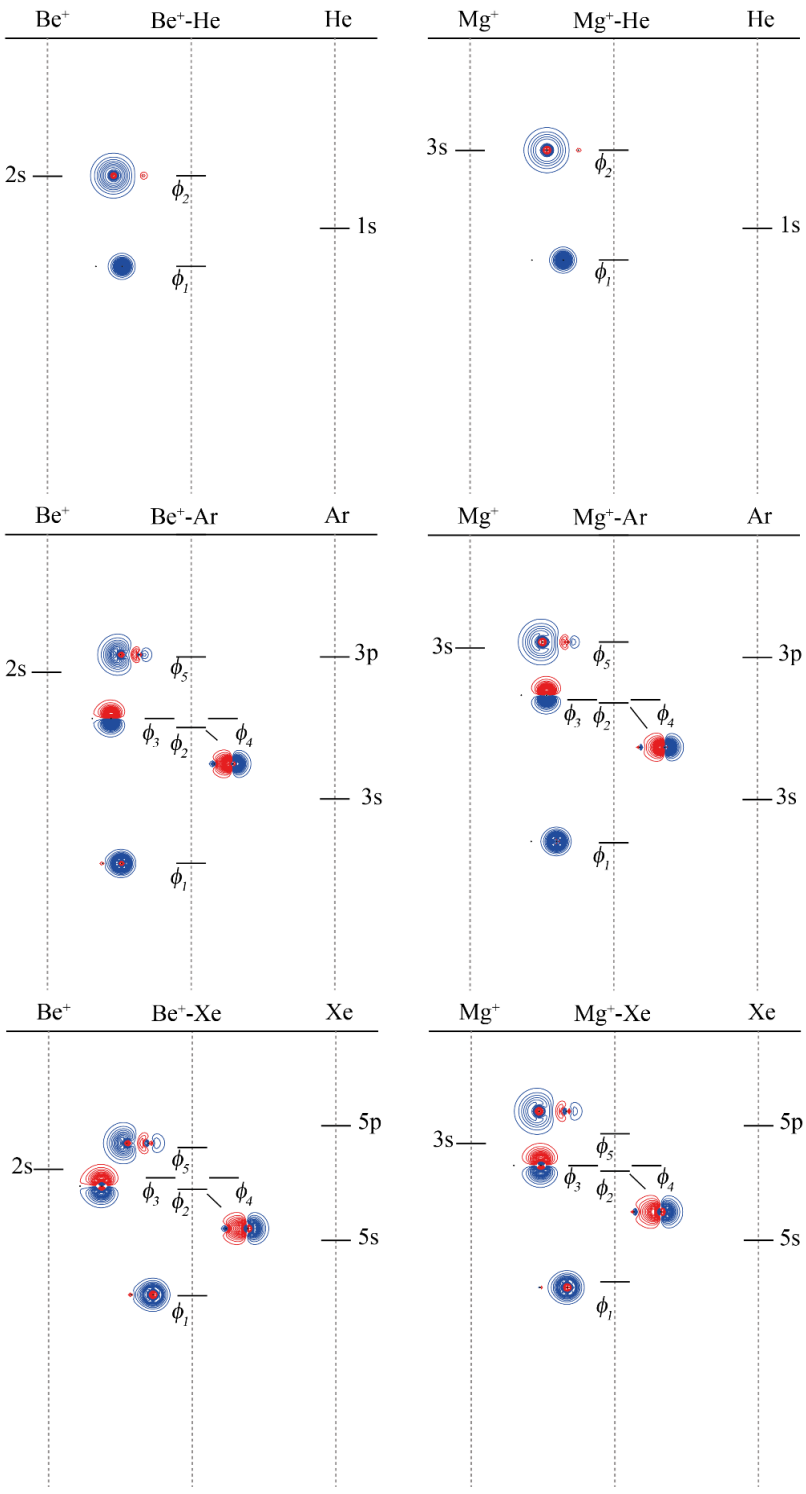


Figure 1-9. MO diagram and contour plots for the Be^+-RG and Mg^+-RG complexes calculated at the RCCSD(T) R_e values obtained at the extrapolated basis set limit.

The latter clearly destabilizes the overall interaction, but this is balanced by the other stabilizing interactions that occur. These deviations in the orbital energies are clearly significant. Although ϕ_5 is predominantly the outermost M^+ *n*s orbital, there is clearly an interaction with the

outermost RG *n*p orbital; although less clear from the contours, there is also a small amount of M^+ outermost *n*s character in ϕ_2. Further, there are small contributions to ϕ_5 from the formally unoccupied M^+ (*n*+1)p orbitals, which arise from the sp hybridisation of the metal centre; this will lead to ϕ_5 being stabilized, reducing its antibonding character, this effect is only slight since the excited M^+ p orbitals are relatively high in energy (Table 1-4). The effect of this small amount of sp hybridisation is to facilitate the movement of electron density away from the internuclear region and so reduce the electron repulsion between the electron in the M^+ *n*s orbital and the incoming RG atom; this also allows RG to approach the M^+ core more closely, increasing the various attractive electrostatic terms, as well as allowing RG to see a higher effective nuclear charge. The sp hybridisation effects can be discerned in minor perturbations to the contour plots of the M^+ electron density on the side opposite to the RG atom. The overall effect of the covalency and sp hybridisation is a clear stabilization of the interaction. It is notable that these effects seem to be similar for the Ar and Xe complexes. Increased degrees of interaction would seem to require a distortion of the inner regions of the singly-occupied *n*s orbital and the latter is clearly more strongly held by the nuclear charge and we conclude the energy cost of this is too high to be recouped from increased charge/induced-dipole terms arising from moving the RG atom closer. Similar comments apply to the Mg^+-RG complexes, but to a much lower extent; this can be attributed to the larger size of the Mg^+ ion, which means that the amount of energy gained from attractive interactions with the RG atoms is less, because of the leading $-\alpha/2R^4$ ion/induced-dipole interaction.

Comparison of Interactions in Groups 2 and 12

In Figure 1-10, Figure 1-11 and Figure 1-16 comparisons of the Group 2 M^+-RG complex with the Group 12 species located along the same period are shown. It is started by considering the MO diagram for Ca^+-He in Figure 1-10, where ϕ_1–ϕ_3 almost entirely correspond to the Ca^+ atomic 3p orbitals, ϕ_4 to the He 1s orbital (but lowered in energy owing to the coulombic field) and ϕ_5 to the Ca^+ 4s orbital. In the case of Zn^+-He, the same picture may be seen to apply, except the penultimate orbitals on Zn^+ are the 3d orbitals, which are almost entirely degenerate. Note that ϕ_6 is coincidentally very close in energy to ϕ_1–ϕ_5, and arises from the coulombically-lowered He 1s orbital; however, the lowering in energy of ϕ_1 is minimal, suggesting this interaction is weak, even though the contours show mixed character.

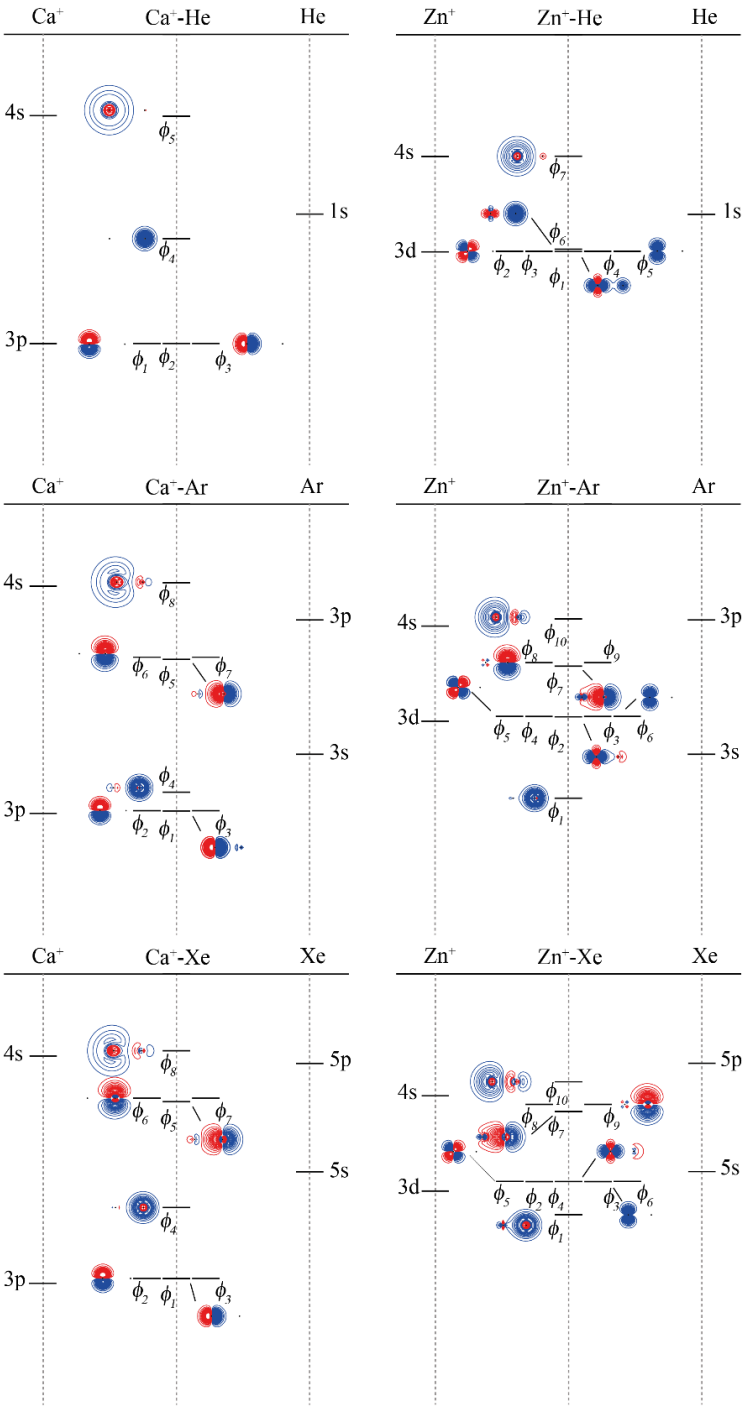


Figure 1-10. MO diagram and contour plots for the Ca^+-RG and Zn^+-RG complexes calculated at the RCCSD(T) R_e values obtained at the extrapolated basis set limit.

It may be seen that ϕ_7 is largely the unperturbed Zn^+ 4s orbital. Reference to the M^+-He diagrams helps us to orient ourselves when considering the M^+-Ar and M^+-Xe MO diagrams, with the observation that the coulombically-lowered RG *n*s orbital becomes ϕ_1 for Zn^+-Ar and Zn^+-Xe, and ϕ_2–ϕ_6 are the (*n*-1)d orbitals. First it is notable that for Ca^+-Ar and Ca^+-Xe ϕ_1–ϕ_3

stay approximately degenerate, and this is also the case for ϕ_2–ϕ_6 for Zn^+-Ar and Zn^+-Xe; consequently, the conclusion can be made that these orbitals remain atom-localized and are essentially unaffected by the complexation. However, ϕ_5–ϕ_7 for Ca^+-Ar and Ca^+-Xe, and ϕ_7–ϕ_9 for Zn^+-Ar and Zn^+-Xe lose their degeneracy, and further, there is a rise in energy of ϕ_{10}, suggesting covalency. Further, ϕ_8 in both Ca^+-Ar and Ca^+-Xe shows off-axis 4d contributions, arising from sd hybridisation.

In contrast, for the Zn^+-RG systems the main effect appears to be covalency, with interaction between the M^+ 4s and the RG outermost np$_z$ orbitals, causing ϕ_7 to lower in energy; there is also rise in energy of ϕ_{10}. In the cases of Zn^+-Ar and Zn^+-Xe there are small perturbations to the contour plots of ϕ_{10} on the side opposite to the incoming RG atom, arising as a result of very small amounts of sp hybridisation; these are small, however, owing to the relatively high energy of the M^+ excited p orbitals (Table 1-4). Small, but noticeable, contributions from the $3d_{z^2}$ orbital may also be seen in ϕ_1 in the case of Zn^+-Xe, and likely arises from the 3d orbitals, noting that the $3d^9 4s^2$ state is fairly low in energy (see Table 1-4 and comments on Hg^+-Xe, below). Note that any mixing between the $3d^{10}4s^1$ and $3d^9 4s^2$ states lead to an increased occupancy of the 4s orbital, and so lead to increased repulsion. Finally, a very small amount of π bonding from the RG atom through the highest occupied np orbitals into the Zn^+ dπ orbitals (d_{xz} and d_{yz}).

Similar, although slightly less marked, observations can be made for the MO and contour plots for Sr^+-RG and Cd^+-RG in Figure 1-11. On the other hand, for the Ba^+-RG plots in Figure 1-16, the perturbations are significant. First, we note that the case of Ba^+-He appears to show very little sign of anything except physical interactions. For Ba^+-Ar, however, it is clear that the degeneracies of ϕ_2–ϕ_4 are broken slightly, and that ϕ_{10} rises in energy a little compared to Ba^+ 6s alongside movement in the energy of ϕ_5; these are indicative of minor incipient chemical effects. The most noticeable effect, however, is in ϕ_8 where quite dramatic off-axis contributions from the low-lying Ba 5d orbitals (Table 1-4) can be seen, showing that there is significant sd hybridisation in these species. Very little further change is seen when moving to Ba^+-Xe.

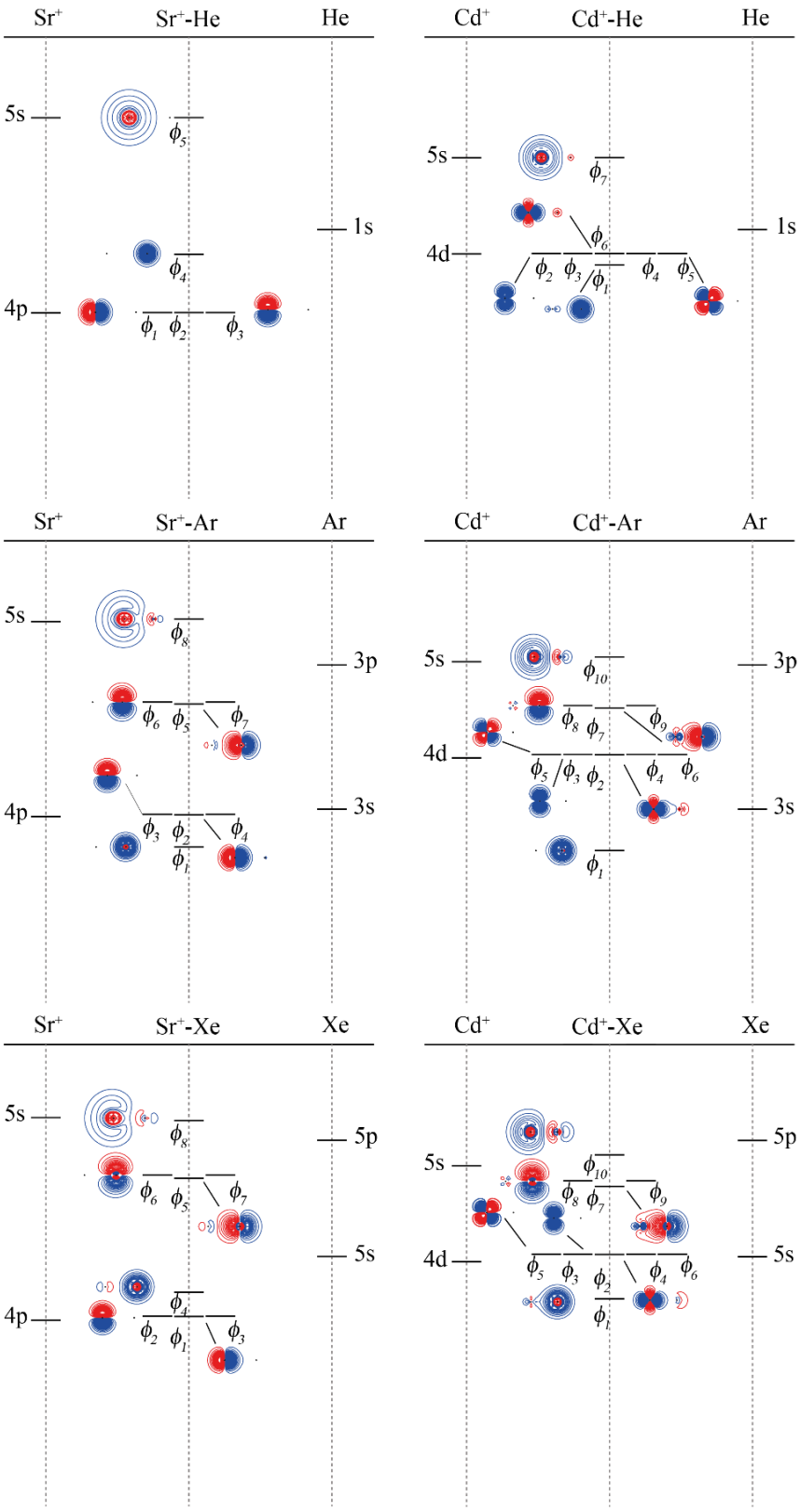


Figure 1-11. MO diagram and contour plots for the Sr^+-RG and Cd^+-RG complexes calculated at the RCCSD(T) R_e values obtained at the extrapolated basis set limit.

The implication of the above is that sd hybridisation is significant for M^+ = Ca^+–Ra^+, but covalency is only a minor effect – it is the lowering of electron density in the internuclear region that is the key driver in these complexes, allowing the RG atom to get close to the M^+ centre and so lower the energy, predominantly via the $-\alpha/2R^4$ term.

Considering now Hg^+-RG, again Hg^+-He shows little indication of any covalency, while for Hg^+-Ar and Hg^+-Xe there is a loss in degeneracy of both the Hg 5d orbitals (ϕ_2–ϕ_6) and the RG *n*p orbitals (ϕ_7–ϕ_9), together with a small rise in energy of ϕ_{10} compared to Hg^+ 6s, indicates that covalency is now present. There are minor perturbations in the ϕ_{10} contour on the side opposite to the incoming RG atom, showing that a very small amount sp hybridisation is occurring – noting the high energy of the Hg^+ excited p orbitals (Table 1-4). Finally, it is notable that there is a small, but increased amount of π bonding from the RG atom through its highest occupied *n*p orbitals into the Hg^+ dπ orbitals (d_{xz} and d_{yz}). In addition, there is a small amount of mixing between the $5d_{z^2}$ orbital and the RG *n*p_z orbital.

Summary

The overall picture is that the M^+-RG complexes involving Group 12 cations, Be^+ and Mg^+ demonstrate a significant amount of covalency, while those involving Ca^+–Ra^+ show significant sd hybridisation. In all cases, sp hybridisation appears to be relatively small. The sd hybridisation clearly has a major impact on the interactions via the lowering of electron density in the internuclear region, and can occur when the excited d orbitals lie low in energy. Conversely, the amount of sp hybridisation that can occur appears to be small, owing to the high energy of the excited p orbitals in all cases (see Table 1-4). In fact the lowest unoccupied (*n*+1)p orbital on Ca^+–Ra^+ is actually lower in energy than those for Be^+ and Mg^+. Hence, some sp as well as sd hybridisation is possible in the Ca^+–Ra^+ species, but the latter is by far the most pronounced.

The observed covalency is the result of the lowering of the electron density in the internuclear region resulting in higher effective Be^+ and Mg^+ nuclear charges being experienced by the RG atom. This is largely driven by the small radii of these ions, particularly for Be^+; this also occurs for the Group 12 cations, whose smaller cationic radii arise following the traversing of the respective d block, which leads to orbital contraction. The ability for the RG atom to approach M^+ closely drives the lowering of energy via the $-\alpha/2R^4$ ion/induced-dipole term.

Table 1-5: Partial atomic charges for the Group 12 M^+-RG complexes, calculated using NPA and AIM methodologies, in units of elementary charge *e*.

M	Charge	Method	M^+-He	M^+-Ne	M^+-Ar	M^+-Kr	M^+-Xe	M^+-Rn
Zn	Q_{Zn}	Mulliken	1.00	0.98	0.94	0.90	0.81	0.74
		NPA	1.00	0.99	0.94	0.90	0.82	0.77
		AIM	1.00	1.01	0.95	0.91	0.83	0.78
	Q_{RG}	Mulliken	0.00	0.02	0.06	0.10	0.19	0.26
		NPA	0.00	0.01	0.06	0.10	0.18	0.23
		AIM	0.00	-0.01	0.05	0.09	0.17	0.22
Cd	Q_{Cd}	Mulliken	1.00	0.99	0.96	0.92	0.87	0.80
		NPA	1.00	1.00	0.97	0.93	0.87	0.83
		AIM	1.00	1.01	0.97	0.93	0.86	0.82
	Q_{RG}	Mulliken	0.00	0.01	0.04	0.08	0.13	0.20
		NPA	0.00	0.00	0.03	0.07	0.13	0.17
		AIM	0.00	-0.01	0.03	0.07	0.14	0.18
Hg	Q_{Hg}	Mulliken	1.00	0.99	0.94	0.89	0.74	0.64
		NPA	1.00	1.00	0.95	0.89	0.74	0.70
		AIM	1.00	1.00	0.95	0.87	0.74	0.66
	Q_{RG}	Mulliken	0.00	0.01	0.06	0.11	0.26	0.36
		NPA	0.00	0.00	0.05	0.11	0.26	0.30
		AIM	0.00	0.00	0.05	0.13	0.26	0.34

In addition, part of the explanation for the covalency lies with the closer energetic proximity of the outermost M^+ *n*s orbitals to the coulombically-lowered outermost p orbitals on RG. It has just been noted that the sd hybridisation that arises for Group 2 Ca^+–Ra^+ occurs from the low-lying unoccupied d orbitals (see Table 1-4), so that the energetic cost of hybridisation is small. This is not possible for the other species owing to the much higher-lying unoccupied d orbitals. In such cases, sp hybridisation is a possibility, but the unoccupied (*n*+1)p orbitals (Table 1-4) are relatively high in energy. Indeed, the outermost *n*p orbitals for Group 12 are significantly higher than both the lowest unoccupied *n*d and (*n*+1)p orbitals for Group 2, perhaps explaining why the amount of hybridisation is small in these species: i.e. even the

smaller ionic radii (and so smaller R_e values) of these species cannot overcome the high energetic cost of hybridisation.

It is notable that in Hg^+-Ar and Hg^+-Xe there is a small amount of $5d_{z^2}$ $5d_{xz}$ and $5d_{yz}$ character mixing with the RG *n*p orbitals; this likely arises from the presence of the excited $5d^96s^2$ state (see Table 1-4 and its footnotes), and causes a loss in degeneracy of the 5d orbitals. The high energy of the excited …$5d^{10}6s^06d^1$ states (see Table 1-4) means that sd hybridisation is unlikely.

Although the Group 2 cations are larger than their neighbouring Group 1 species,[65] actually the corresponding R_e values for M^+-RG involving the Group 2 cations and RG = Ne–Rn are smaller than those involving Group 1[1-5] demonstrating the significant distortions that occur in the former; this also leads to the D_e values from the Group 2 species being the larger. In contrast, the R_e ordering is reversed in the cases of RG = He, demonstrating that deriving R_e values from the M^+-He complexes demonstrate a more intuitive set of ionic radii. [65]

1.3.5 Partial Atomic Charge Analyses

Partial atomic charges for the M^+-RG complexes have been calculated using Mulliken, NPA and AIM analyses, and the results are collected in Table 1-6 and 6 for the Group 2 and Group 12 complexes, respectively. The Group 12 species are initially considered and then move onto Group 2.

Group 12

There is good agreement between all three methodologies for $M^+ = Zn^+$–Hg^+. This is somewhat surprising since Mulliken population analysis is very frequently unreliable. Importantly, all sets of results give the same trend of increasing partial charge on the rare gas atom with its increasing atomic number.

Calculated charges show there is some slight migration of charge taking place in the Ar complexes, in line with the delocalization of orbital density (via covalency) in the φ_7 and φ_{10} orbital contours (see Figure 1-10). The amount increases as the RG atomic number increases, but the transfer is slightly smaller for Cd^+ than it is for Zn^+ and Hg^+; for the species containing the lighter RG atoms the values for the latter two metals is very similar, but for the Xe and Rn, the amount of charge transfer is slightly larger for Hg^+ (~0.3*e*) than for Zn^+ (~0.2*e*). All of the latter are in line with the atomic radii discussed above. These amounts of charge transfer are quite significant and suggest chemical interactions, in line with the contour plots, the loss in

degeneracy of the RG *n*p orbitals and the rise in energy of the M^+ *n*s orbital. The trend also follows the energy of the singly-occupied *n*s orbital (which is energetically the lowest for Hg^+).

Table 1-6: Partial atomic charges for the Group 2 M^+-RG complexes, calculated using NPA and AIM methodologies, in units of elementary charge *e*.

M	Charge	Method	M^+-He	M^+-Ne	M^+-Ar	M^+-Kr	M^+-Xe	M^+-Rn
Be	Q_{Be}	Mulliken	1.00	0.97	0.82	0.97	0.52	0.42
		NPA	1.00	0.99	0.91	0.88	0.82	0.79
		AIM	1.00	1.02	1.02	1.00	0.98	0.97
	Q_{RG}	Mulliken	0.00	0.03	0.18	0.03	0.48	0.58
		NPA	0.00	0.01	0.09	0.12	0.18	0.21
		AIM	0.00	-0.02	-0.02	0.00	0.02	0.03
Mg	Q_{Mg}	Mulliken	1.00	0.98	0.97	0.93	0.83	0.75
		NPA	1.00	1.00	0.98	0.97	0.93	0.92
		AIM	1.00	1.01	1.02	1.02	1.00	0.99
	Q_{RG}	Mulliken	0.00	0.02	0.03	0.07	0.17	0.25
		NPA	0.00	0.00	0.02	0.03	0.07	0.08
		AIM	0.00	-0.01	-0.02	-0.02	0.00	0.01
Ca	Q_{Ca}	Mulliken	1.00	0.99	0.96	0.95	0.92	0.88
		NPA	1.00	1.00	0.99	0.98	0.97	0.97
		AIM	1.00	1.01	1.02	1.02	1.01	1.00
	Q_{RG}	Mulliken	0.00	0.01	0.04	0.05	0.08	0.12
		NPA	0.00	0.00	0.01	0.02	0.03	0.03
		AIM	0.00	-0.01	-0.02	-0.02	-0.01	0.00
Sr	Q_{Sr}	Mulliken	1.00	0.99	0.98	0.99	0.94	0.85
		NPA	1.00	1.00	1.00	1.01	0.97	0.92
		AIM	1.00	1.01	1.03	1.04	1.00	0.96
	Q_{RG}	Mulliken	0.00	0.01	0.02	0.01	0.06	0.15
		NPA	0.00	0.00	0.00	-0.01	0.03	0.08

M	Charge	Method	M^+-He	M^+-Ne	M^+-Ar	M^+-Kr	M^+-Xe	M^+-Rn
		AIM	0.00	-0.01	-0.03	-0.04	0.00	0.04
Ba	Q_{Ba}	Mulliken	1.00	0.99	0.98	0.98	0.97	0.93
		NPA	1.00	1.00	1.00	0.98	0.99	0.98
		AIM	1.00	1.01	1.01	1.01	1.02	1.00
	Q_{RG}	Mulliken	0.00	0.01	0.02	0.02	0.03	0.07
		NPA	0.00	0.00	0.00	0.02	0.01	0.02
		AIM	0.00	-0.01	-0.01	-0.01	-0.02	0.00
Ra	Q_{Ra}	Mulliken	1.00	0.94	0.97	0.96	0.96	0.93
		NPA	1.00	0.94	0.99	0.99	0.99	0.98
		AIM	1.00	0.96	1.02	1.02	1.01	1.01
	Q_{RG}	Mulliken	0.00	0.06	0.03	0.04	0.04	0.07
		NPA	0.00	0.06	0.01	0.01	0.01	0.02
		AIM	0.00	0.04	-0.02	-0.02	-0.01	-0.01

Group 2

Although in agreement for the lightest two RG atoms, the results from the different methods of charge analysis for Group 2 are in poor agreement with each other and are the most divergent when the atomic numbers of M^+ and RG differ the most, being the poorest for Be^+-Xe and Be^+-Rn. These are the cases when RG is closest to the M^+ centre, and hence it becomes more difficult to decide on which centre the electron density is located. Qualitatively, it seems NPA does the best when compared to the contour plots. For example, the contours for Be^+-Xe suggest a reasonable amount of charge transfer, while for Mg^+-Xe, very little. This seems to correspond best to the NPA charges, since AIM suggests very little transfer, particularly for Mg^+-Xe. Clearly the very large amounts of transfer suggested by the Mulliken analysis is far from reasonable, particularly for Be^+-Rn where the transfer is implied to be > 0.5*e* – we experienced similar issues in recent work on C^+-RG.[67]

Thus, it seems that describing the partial atomic charges for the Group 2 M^+–RG complexes is rather more challenging than for the Group 12 ones, especially so for the Be^+-RG and Mg^+-RG

complexes involving the heavier rare gases.

Table 1-7: Input Parameters for the electrostatic model potential (Eqn. 1-2)[a]

Species	α_d/ Å^3	α_q/ Å^5	α_o/ Å^7	B (e^{-1} Å^6)	γ/ e^{-2} Å^7	N	mass/ m_u
He	0.205	0.101	0.123	-0.144	0.501	1.434	4.00
Ne	0.396	0.27	0.397	-0.286	1.383	4.45	20.2
Ar	1.64	2.08	6.16	-3.07	13.6	5.90	39.95
Kr	2.48	3.97	16.35	-6.53	30.2	6.70	83.8
Xe	4.04	8.8	42.7	-15.57	80.0	7.79	131.3
Rn	5.1	20	110	-40	134	9	222
Be^+	3.7	2.20				0.77	9.012
Mg^+	5.5	6.22				0.98	24.31
Ca^+	11	54				1.05	40.08
Sr^+	13.1	68				1.1	87.82
Ba^+	18.4	200				1.16	137.3
Ra^+	15.5	105.7				1.2	226.03
Zn^+	2.8	4				6	65.39
Cd^+	3.5	4.5				6.5	112.41
Hg^+	2.7	4				7	201.97

[a] See text for sources of values and definitions of quantities.

1.3.6 Model Potential

In Ref. 18 a model potential was set up and used to investigate chemical versus physical interactions in M^+-RG, mostly based on available experimental data. The model potential employed electrostatic terms up to $1/R^8$ and a two-parameter Born-Mayer potential, and is given in Eqn. 1-2 This idea was extended in Refs. 1 and 6 to include the effect of damping factors,[68] which are given in Eqn. 1-3, which model the attenuation of the different interaction terms at short R as a result of overlapping electron densities. Separate damping factors are applied to each $1/R^n$ term in the model calculated for that value of n; note that it is assumed that the b parameter in the damping factors is the same as the Born-Mayer b parameter. Equations involving the model potential are solved, using values for R_e, D_e and ω_e (see Refs.

1, 6 and 18). This yields the two Born-Mayer potential parameters, *A* and *b* as well as the effective charge on the metal cation, *Z*. The latter is the charge required for the model potential to fit the R_e, D_e and ω_e values; in the case of the physical model being a good description, *Z* should come out to be 1.00. For the Group 1 M^+-RG complexes studied in Refs. 1 and 6, very little difference between the damped and undamped values were seen, suggesting that there is little interpenetration of the M^+ and RG electron clouds in these species, and so physical interactions dominate.

$$V(R) = -\frac{\alpha_{RG_d} Z^2}{2R^4} - \frac{C_6}{R^6} - \frac{\alpha_{RG_q} Z^2}{2R^6} + \frac{B_{RG} Z^3}{2R^7} - \frac{C_8}{R^8} - \frac{\alpha_{RG_o} Z^3}{2R^8} - \frac{\gamma Z^4}{24R^8} + Ae^{-bR} \qquad \text{Eqn. 1-2}$$

$$f_n(R) = 1 - \exp(-bR) \sum_{k=0}^{n} \frac{[bR]^k}{k!} \qquad \text{Eqn. 1-3}$$

In Eqn. 1-2 and Table 1-7, the α terms, denoted in an obvious way, are the dipolar, quadrupolar and octupolar polarizabilities of the RG atoms, C_6 and C_8 are the usual dispersion coefficients (calculated from the polarizabilities of RG and M^+ using the Slater-Kirkwood[69] and Koutselos and Mason[70] approximations), *N* is the effective number of "oscillator" electrons used to calculate C_6 and C_8,[69] *B* is the dipolar-quadrupolar polarizability of RG, and γ is the hyperpolarizability of RG; *A* and *b* are the Born-Mayer parameters. In Table 1-7 the values for these quantities used in the present work are presented, many of which are well-established, or have been calculated or estimated – see Ref. 18. The values from that work have been employed, with the following exceptions. The α_d values for Sr^+, Ba^+ and Ra^+ were taken from Ref. 71, while α_q for Sr^+ was taken from from Ref. 72 (the same source for this quantity as the other Group 2 cations up to Ba^+), and α_q for Ra^+ was taken from Ref. 73. Values of *N* for Sr^+, Ra^+ and Rn were estimated in the present work. For Rn, values of α_d and γ were taken from Ref. 74, while values for α_q, α_o and *B* were estimated herein. In the top part of Table 1-8 the calculated charges for the Group 2 M^+-RG complexes are shown. It is notable that, except for the notable cases of Be^+-RG, for all complexes involving RG = He and Ne, the calculated charges are between 0.97 and 1.25, either damped or undamped. It is also notable that in most cases damping leads only to the expected small increase in the calculated effective charge. For

Be^+-RG, the damped effective charge is calculated to be significantly larger, and in the notable case of Be^+-Ne, the damped value is 1.43, while the undamped one is 0.97. This may be indicative of significant penetration of the electron clouds, but the MO plots in Figure 1-9 suggest otherwise; more likely is that this is caused by the simplicity of the model potential, and hence spurious values of Z arise when the potential is not working well. In the above, the high degree of covalency has been noted in the Be^+-RG complexes, and the unusual reduced potential plots for the Group 2 M^+-Ne complexes; later it shall be emphasized that Be^+-Ne is a very unusual case.

The charges for the M^+-Ar complexes have surprisingly low calculated Z values, as does Ba^+-Kr. Peculiarly, although solutions to the undamped model potential equations were obtained for Ba^+-Ar in Ref. 18, no solutions were possible here, either damped or undamped, using the calculated R_e, D_e and ω_e values for this species. Again, this points to the interactions being somewhat unusual for this complex. Solution to the model potential equations makes use of two parameters that are representative of the minimum (R_e and ω_e), as well as D_e; furthermore, it is assumed that the electrostatic and Born-Mayer parameters are applicable to the whole potential – indeed, in Ref. 6 the model potential with the obtained Z, A and b parameters fitted the whole calculated potential very well for the lightest, Li^+-He, and the heaviest, Cs^+-Xe, complexes considered. In those cases, Z had a value very close to 1.00, demonstrating that the interactions in those species were largely physical in nature. The suggestion from the values in Table 1-8 is that this is not the case for many of these species.

In summary, when significant amounts of R-dependent changes in the amount of hybridisation occur, such as in the Group 2 M^+-RG complexes, then trying to model the interaction with a simple model potential such as Eqn. 1-2 becomes futile. It is notable that the model potential fails completely for Ba^+-Ar in that no solution for Z could be found.

For the Group 12 species, whose calculated Z values are presented in the bottom part of Table 1-8, it is found largely that the model potential solutions give rise to Z values in the range 0.95–1.15 for most of the species, with generally a small increase when damping is included, and hence it appears to be working well. That slightly larger values are calculated for the heaviest Hg^+-RG complexes, suggests that those values may be fortuitously "sensible" and that in fact the model potential not appropriate. This would be in line with the significant amounts of covalency observed in the contour plots, discussed above.

Table 1-8: Effective charges on M^+ from the electrostatic model potential (Eqn. 1-2),[a] in units of elementary charge *e*.

M^+	Method	M^+-He	M^+-Ne	M^+-Ar	M^+-Kr	M^+-Xe	M^+-Rn
			Group 2				
Be^+	undamped	1.03	0.97	0.67	0.88	1.06	0.99
	damped	1.05	1.43	0.82	1.02	1.20	1.18
Mg^+	undamped	1.05	0.99	0.86	0.89	0.97	0.91
	damped	1.05	1.03	0.92	0.93	1.00	0.96
Ca^+	undamped	1.08	1.09	0.64	0.71	0.82	0.79
	damped	1.08	1.14	0.72	0.76	0.86	0.84
Sr^+	undamped	1.10	1.15	0.69	0.75	0.84	0.80
	damped	1.10	1.19	0.74	0.79	0.87	0.84
Ba^+	undamped	1.12	1.19	-[b]	0.42	0.67	0.65
	damped	1.12	1.25	-[b]	0.46	0.71	0.69
Ra^+	undamped	1.14	1.17	0.88	0.87	0.91	0.87
	damped	1.14	1.17	0.91	0.89	0.93	0.90
			Group 12				
Zn^+	undamped	1.05	0.97	0.96	1.01	1.12	1.06
	damped	1.06	0.99	0.99	1.04	1.16	1.13
Cd^+	undamped	1.08	1.01	1.02	1.04	1.12	1.06
	damped	1.09	1.01	1.03	1.05	1.13	1.10
Hg^+	undamped	1.12	1.06	1.10	1.15	1.29	1.25
	damped	1.12	1.07	1.11	1.16	1.30	1.29

[a] See text.

[b] No solution – see text.

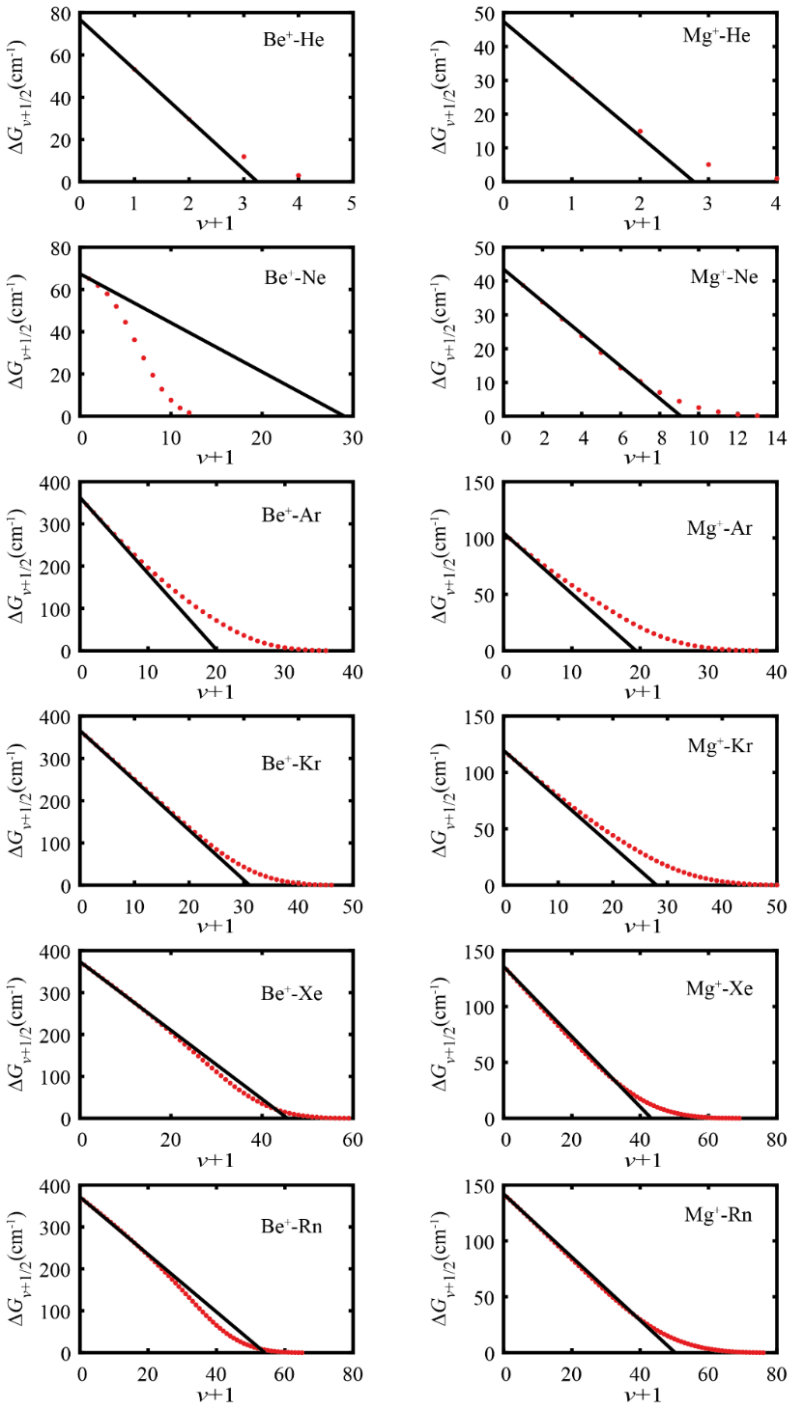


Figure 1-12. Birge-Sponer Plots for Be^+-RG and Mg^+-RG. The red dots are the calculated spacings between consecutive vibrational levels, while the line is a Morse line calculated from the ω_e and $\omega_e x_e$ values given in Table 1-1 (see text).

1.3.7 Birge-Sponer Plots

In general, close to R_e, one would expect a diatomic species to be described well by a linear Birge-Sponer plot and then at long-range this would transfer over into Leroy-Bernstein behaviour.[75-77]

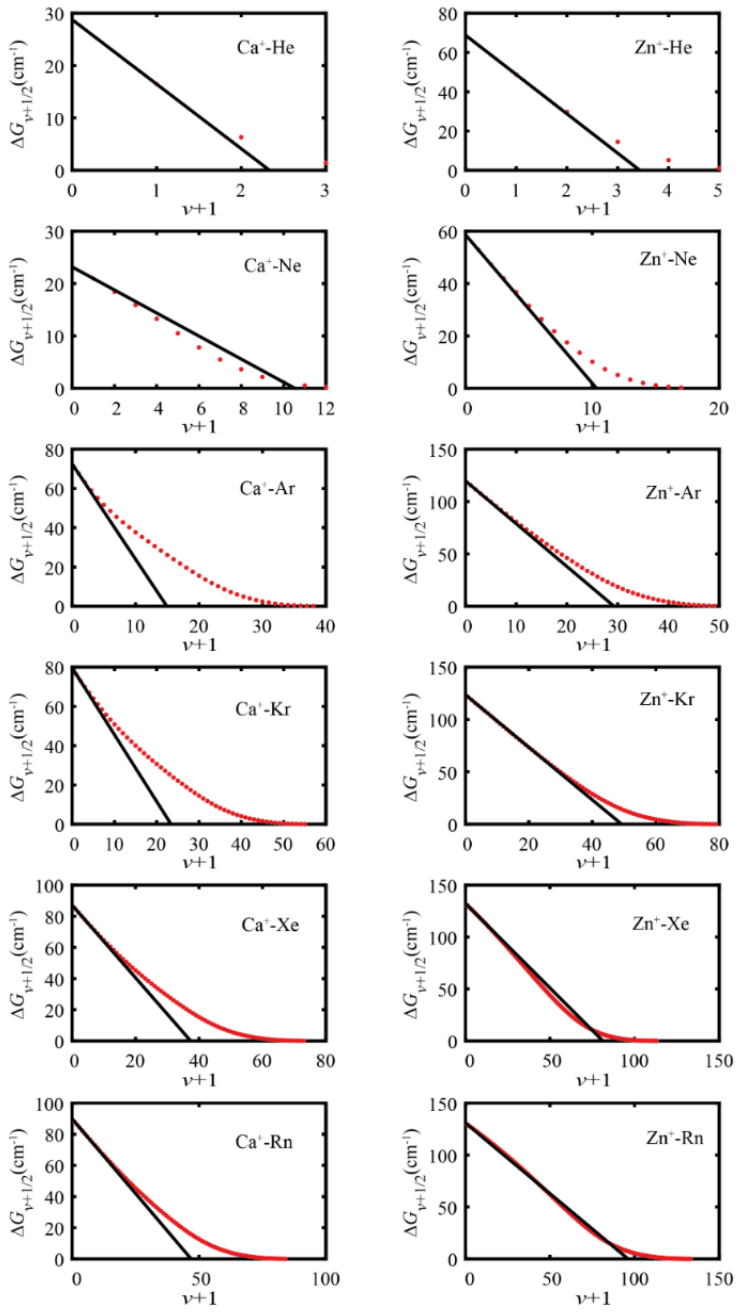


Figure 1-13. Birge-Sponer Plots for Ca^+-RG and Zn^+-RG. The red dots are the calculated spacings between consecutive vibrational levels, while the line is a Morse line calculated from the ω_e and $\omega_e x_e$ values given in Table 1-1 and Table 1-2(see text).

For a suitably high number of bound levels, this long range behaviour is expected to follow a $(\Delta G_{v+1/2})^{2n/(n+2)}$ dependence, where n is that of the R^{-n} dependence of the potential at long range. For an atomic cation/rare gas interaction, an R^{-4} dependence is expected, and so we expect a $(\Delta G_{v+1/2})^{4/3}$ dependence at long range. Hence, it is expected that the Birge-Sponer plots for the M^+-RG complexes to be approximately linear, but then to deviate, exhibiting a $(\Delta G_{v+1/2})^{4/3}$ dependence for high v, i.e. close to the dissociation limit.

Presented in Figure 1-12, Figure 1-13, Figure 1-14 and Figure 1-15 are plots of $\Delta G_{v+1/2}$ *vs.* $(v+1)$ for the Group 2 and Group 12 M^+–RG complexes where v is the value for the lower of a pair of consecutive vibrational levels; although not strictly a Birge-Sponer plot (where the abscissa would be $v+1/2$), the term is used here for convenience. On each graph, the red points correspond to the calculated spacings between adjacent calculated vibrational levels, while the solid black "Morse line" corresponds to "Morse spacings" calculated from the vibrational constants ω_e and $\omega_e x_e$ presented in Table 1-1 and Table 1-2; as noted above, derivation of the constants ω_e and $\omega_e x_e$ relies on only the lowest two vibrational levels together with the D_e value. Hence, the correspondence between the red points and the black line gives an indication of how consistent the curvature close to R_e is with regards to the shape of the rest of the IEC. These plots give much more information than simply the values of D_e^{Morse}/D_e presented in Table 1-1 and Table 1-2; in particular, in many cases they exhibit changes in the curvature of the IEC from R_e to the dissociation asymptote. So, for example, D_e^{Morse}/D_e for Mg^+-Ne is 1.05 and it might be expected that the Morse line would largely agree with the Birge-Sponer one for this complex; however, the plot shows that the Birge-Sponer plot is in fact curved with some vibrational levels falling below the Morse line while others lie above. Overall these deviations largely cancel out across the whole of the plot, so that the D_e^{Morse}/D_e value hides the fact that these variations in the shape of the IEC are occurring. It is clear, therefore, that caution is merited in deducing too much from the D_e^{Morse}/D_e ratios in Table 1-1 and Table 1-2. However, it is clear that when values are far from 1.00, either below or above, then it is likely that the BS plot will show unexpected behaviour.

While examining the BS plots for Be^+-RG in Figure 1-12, it can be

seen that for RG = Ar and Kr, the behaviour is much as expected, with the linear region at low v following the Morse line closely, and the LeRoy-Bernstein deviation for the higher values. However, for RG = Xe and Rn the BS plot has dipped under the Morse line for intermediate values of v; this is intepreted in terms of a change in the interaction terms at long- versus short-R.

As covalency and small amounts of sp hybridisation occur, the attractive and repulsive parts of the potential will change, leading to curvature in the BS plot.

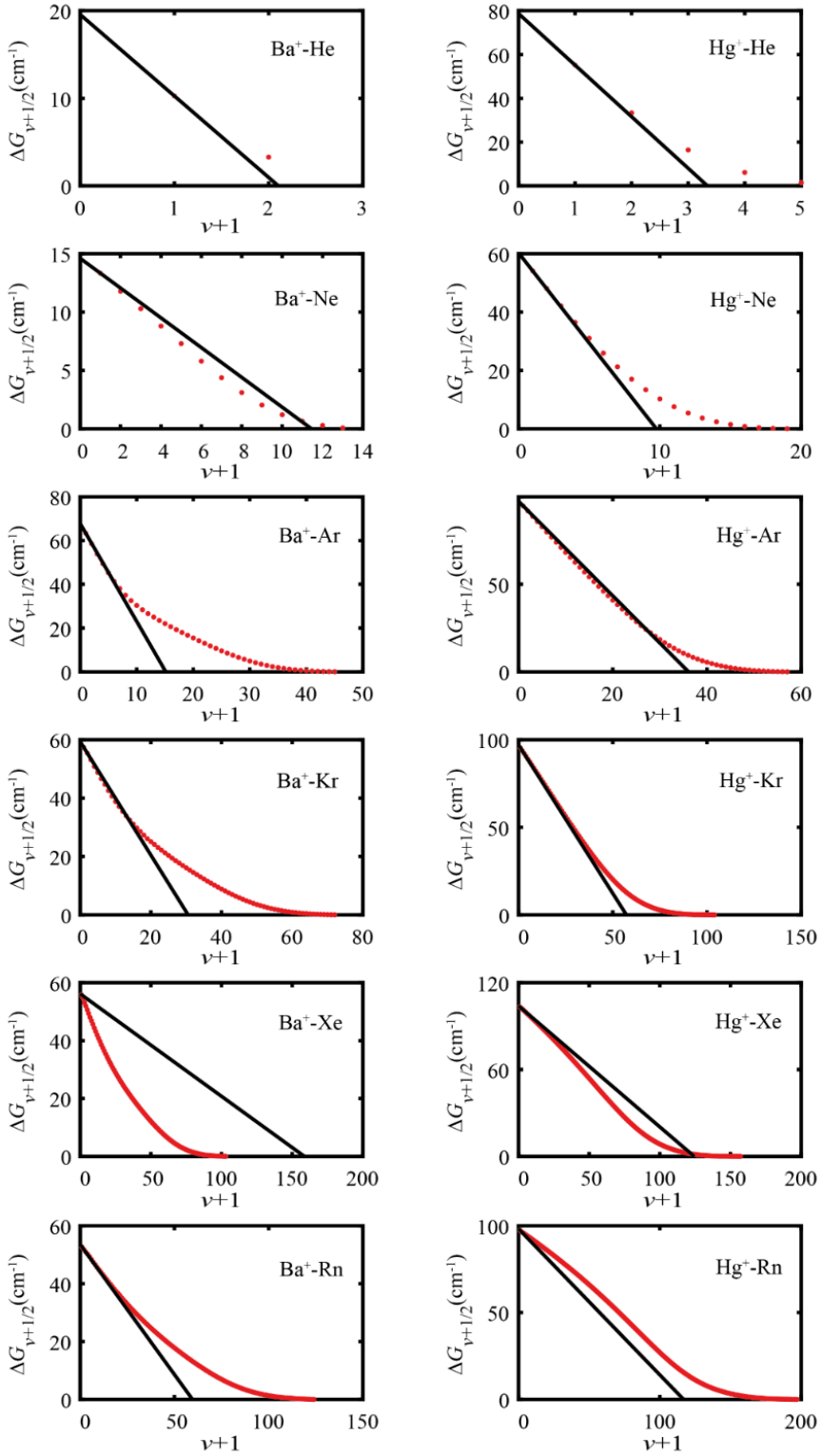


Figure 1-14. Birge-Sponer Plots for Ba^+-RG and Hg^+-RG. The red dots are the calculated spacings between consecutive vibrational levels, while the line is a Morse line calculated from the ω_e and $\omega_e x_e$ values given in Table 1-1 and Table 1-2 (see text).

The effect is most stark in the case of Be^+-Ne, where the BS points lie far under the Morse line, indicating that the curvature of the IEC close to R_e is very different from that at even moderate R values. One can visualize this most easily by considering the Be^+ and Ne atoms approaching each other from long range, as Ne gets closer, attracted by the positive charge, its electrons start to interact with the Be^+ 2s one and this brings in a repulsive term. This softens the potential at moderate R

values (being the sum of the attractive and repulsive terms), and so causes the decrease in slope of the BS plot for low v. (Recall that the Be^+-Ne reduced potential plot in Figure 1-3 showed the starkest deviation from the behaviour of the other Be^+-RG species, indicating a significantly softer repulsive potential.) It may thus be seen that Be^+-Ar and Be^+-Kr are intermediate cases where the sum of the attractive and repulsive terms give approximately linear BS plots and Morse-like behaviour. (Note that little can be said regarding the plot for Be^+-He, since there are so few bound levels.) A very similar picture can be seen for the Mg^+-RG complexes, although Mg^+-Ne does not show the stark deviation from the Morse line seen for Be^+-Ne (again in line with the reduced potential plots in Figure 1-3). This is rationalized by the fact that Mg^+ is larger than Be^+ owing to the better shielding in the former, this leads to less overlap of the Ne and Mg^+ 3s orbitals than the corresponding situation in Be^+-Ne (see MO plots in Figure 1-9).

When examining the BS plots for Ca^+-RG – Ra^+-RG, it is seen that these show unusual shapes, most noticeably in the RG = Ar–Xe plots. There is the expected long-range curved region, but then an approximately linear section at mid-v values and then a steepening of the potential at low-v. This changing slope is likely attributable to the sd hybridisation (see molecular orbital plots and above discussion) that will lead to an R-dependent change in the form of the potential as the RG atom approaches M^+, giving rise to very un-Morse-like behaviour as the electron density moves off-axis. Close to R_e, however, it is assumed that the amount of electron density in the sd hybrid orbitals reaches a level whereby repulsion effects come into play, and this causes a steepening of the potential in this region. For Be^+-Ne, the steepening is not seen, since the Ne is not polarizable enough to offset the cost of hybridizing enough of the electron density for this to occur.

Now the Group 12 M^+-RG BS plots in Figure 1-13, Figure 1-15 and Figure 1-14 are examined. It can be seen that for Zn^+-RG, Figure 1-13, there is a close-to-linear region for low *v*, but some bowing occurs for Zn^+-Xe and this is more noticeable for Zn^+-Rn. Matching this with the MO diagrams in Figure 10, there is a minor amount of elongation of the Zn^+ 4s orbital on the side opposite to the incoming RG atom, and this is in line with the high 4p ← 4s excitation energy (Table 1-4). Instead, energy is gained by some covalency with electron density transferred into the outermost *n*p orbital on the RG atom.

However, in the low-*v* region, close to R_e, a significant amount of repulsion occurs as the incoming RG atom gets cushioned by the 4s electron density, causing an overall softening of the potential, and hence the curvature of the BS plot into a lower-gradient region.

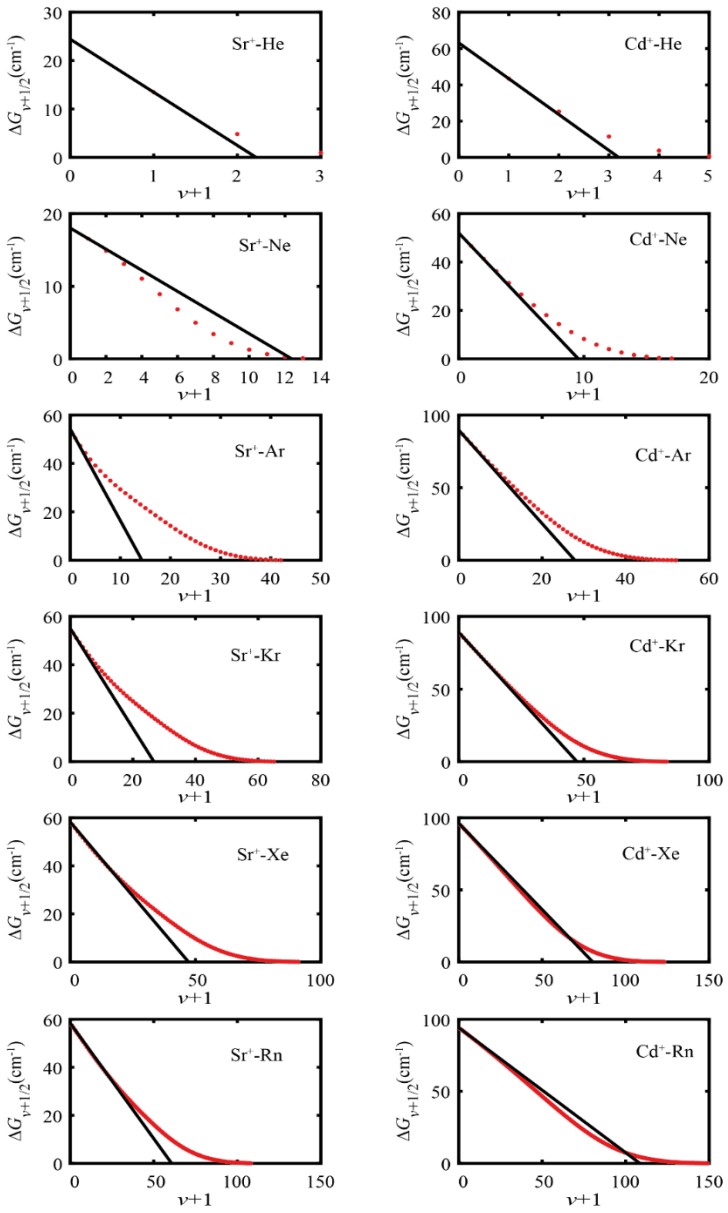


Figure 1-15. Birge-Sponer Plots for Sr^+-RG and Cd^+-RG. The red dots are the calculated spacings between consecutive vibrational levels, while the line is a Morse line calculated from the ω_e and $\omega_e x_e$ values given in Table 1-1 and Table 1-2(see text).

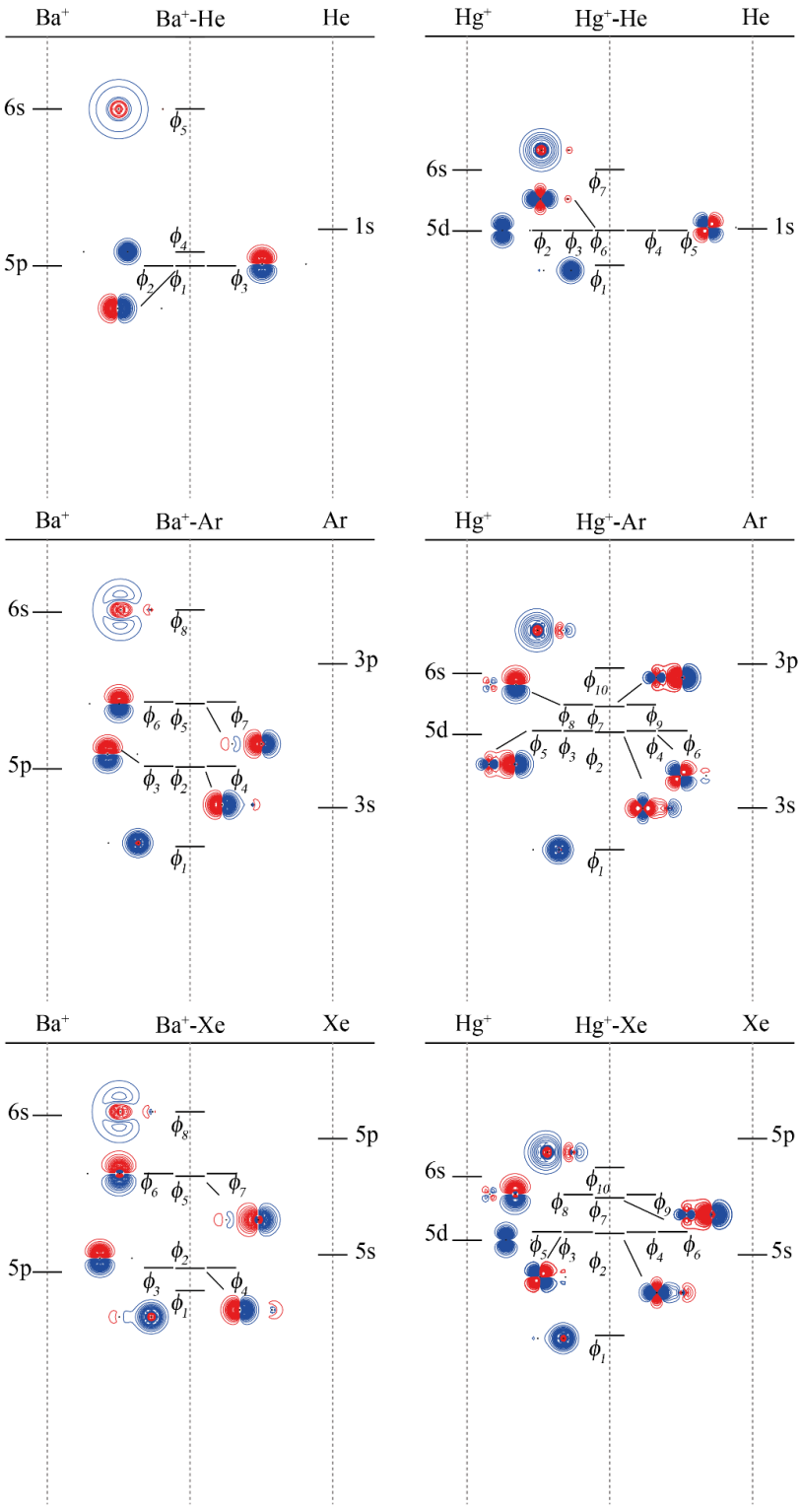


Figure 1-16. MO diagram and contour plots for the Ba^+-RG and Hg^+-RG complexes calculated at the RCCSD(T) R_e values obtained at the extrapolated basis set limit

Table 1-9: Local energy densities $H(R)$ for the Group 2 and 12 M^+-RG complexes.[a]

	He	Ne	Ar	Kr	Xe	Rn
			Group 2			
Be^+	0.0006	-0.0022	-0.0025	-0.0071	-0.0116	-0.0133
Mg^+	0.0002	0.0000	0.0001	-0.0001	-0.0009	-0.0014
Ca^+	0.0001	0.0002	0.0020	0.0017	0.0011	0.0007
Sr^+	0.0001	0.0002	0.0016	0.0014	0.00010	0.0007
Ba^+	0.0001	0.0002	0.0021	0.0014	0.0008	0.0006
Ra^+	0.0001	0.0001	0.0011	0.0011	0.0008	0.0006
			Group 12			
Zn^+	0.0008	0.0006	-0.0029	-0.0064	-0.0084	-0.0089
Cd^+	0.0008	0.0007	0.0005	-0.0018	-0.0037	-0.0044
Hg^+	0.0013	0.0011	-0.0002	-0.0040	-0.0071	-0.0080

[a] Calculated at the bond critical points from the AIM analyses.

A similar picture appears to hold for the Cd^+-RG BS plots, Figure 1-15, but with the bowing being slightly less pronounced, likely caused by the slightly larger Cd^+ ion; this is also consistent with the smaller amount of outermost *n*p contribution to the MOs in the plots – see Figure 1-11. When we move on to examining the BS plots for Hg^+-RG in Figure 16, however, it may be seen that there is significant departure from the Morse line, and significant bowing of the BS plot from mid- to low-*v*. Again, by examining the MO contour plots in Figure 12, the amount of sp hybridisation appears to be small, as no elongation of the Hg^+ 6s orbital is noticeable; however, there is prominent mixing of the Hg^+ 6s and outermost np_z RG orbitals. Furthermore, although there are small contributions in the cases of Zn^+-RG and Cd^+-RG, in Hg^+-RG a sizeable mixing between the $np_{x,y}$ RG orbitals and the d_{xz} and d_{yz} orbitals is evident. The MO contour plots in Figure 1-16 suggests that these d orbitals are (*n*-1)d orbitals, and there is a distinct break in the degeneracy in the five 5d orbitals in the Hg^+-Ar and Hg^+-Xe plots in Figure 1-16. It is interesting to note the contrast between the MO contour plots of Ba+-RG and Hg+-RG in Figure 1-16 (and, to a lesser extent the corresponding comparisons in Figure 1-10

and Figure 1-11). The sd hybridisation dominates in the case of the Group 2 species (Ca+-RG – Ra+-RG), but this is minimal for the corresponding Group 12 species because the available d orbitals for hybridisation are so much higher in energy (Table 1-4). In the case of Hg^+-RG, where the $5d^96s^2$ "d-hole" state is relatively low in energy (but still far higher than the nd^1 states for Group 2), hybridisation does not occur to any great extent since this would lead to higher electron density in the Hg^+ 6s orbital, enhancing rather than alleviating the electron repulsion. In addition, the *n*p orbitals are also significantly higher in energy for the Group 12 species, and this means that sp hybridisation is too costly to contribute much to the stabilization of these species. Hence, the only route open is small amounts of covalency/charge transfer.

1.3.8 *H*(*R*) values

Presented in Table 1-9 are the values of the *H*(*R*) parameter from the AIM analysis. It has been argued that a robust criterion for determining covalency is that the total local electronic energy density, *H*(*R*), has a negative value.[78] The values of the *H*(*R*) parameter implies that there is a small amount of covalency for all of the Be^+-RG complexes except for RG = He, and that the amount of covalency increases with the atomic number of RG. For Mg^+-RG there are only small indications of covalency for the heavier species. Overall, this appears to be in line with the MO contour plots in Figure 1-9, with the covalency enhanced for Be^+-RG because of the smaller size of Be^+, allowing the RG atoms to approach more closely. Of the series that exhibit covalency, the Mg^+-RG complexes are the most weakly bound. This can be attributed to the larger size of the Mg^+ ion coupled with its 3s orbital being furthest from the outermost RG *n*p orbitals energetically. Then when looking at the *H*(*R*) values for the other Group 2 M^+-RG complexes for $M^+ = Ca^+$–Ra^+ (except for Cd^+-Ar), it is seen that these values are all positive indicating essentially no covalency; the implication is that the observed sd hybridisation on the metal centre occurs as a result of the incoming RG atom, but the effects are all atom-centred and results in minimal sharing of electron density between M^+ and RG – see MO diagrams, contour plots and above discussion.

For the Group 12 species, there is no covalency for the species with RG = He and Ne. However, all of the other M^+-RG complexes have $H(R) < 0$, and the magnitude increases with the atomic number of RG. The Cd^+-RG series has the smallest covalency, which is again in line with the larger size of Cd^+. These covalency effects are reflected in the equilibrium dissociation energies of the Group 12 complexes, which are much higher than for the corresponding M = Ca–Ba complexes with the heavier rare gases, and more in line with the M = Be and Mg complexes.

The Be^+-RG series is the most strongly bound out of both Groups 2 and 12, owing to the small size of Be^+ and its low number of electrons. These comments are in line with the MO diagrams, contour plots and above discussion.

1.4 Conclusions

In the present work we high-quality IECs for M^+-RG complexes for RG = He–Rn and M^+ = Be^+–Ra^+ and Zn^+–Hg^+ have been reported. These were calculated at the RCCSD(T) level of theory, and were basis set extrapolated from quadruple- and quintuple-ζ basis sets. From these IECs spectroscopic constants have been calculated, which are in excellent agreement with the small number of experimental values available. Further, trends in some of the key constants have been examined, which indicated that the interactions across these species were different.

Hence the interactions in the Group 2 and Group 12 M^+-RG complexes were examined using a range of approaches. One of the key indicators was the MO diagrams combined with the MO contour plots. These indicated that even though both of these series of metals have …*n*s^1 electronic configurations, there are three modes of interaction: physical, covalent and sd hybridisation, with the latter alleviating the repulsion that occur as the electrons on the approaching RG atom start to interact with the outermost *n*s orbital on M^+. The role of covalency was confirmed by an examination of the AIM $H(R)$ parameter, which concurred that this was present for Be^+-RG (RG = Ne–Rn), minimally present for Mg^+-RG (RG = Kr–Rn), and present for all Group 12 M^+-RG species for RG = Ar–Rn (but not Cd^+-Ar). For Be^+-He, Mg^+-RG (Rg = He–Ar), covalency was largely non-existent, and although also absent for M^+ = Ca^+–Ra^+ and RG = Ar–Rn, there was significant sd hybridisation to facilitate the interaction.

Hence for Be^+-He, Mg^+-RG (Rg = He–Ar), the Group 12 M^+-RG (RG = He and Ne) and Cd^+-Ar complexes, it is concluded that the interactions are "physical", with no clear evidence of chemical behaviour. For Be^+-RG (RG = Ne–Rn), Mg^+-RG (RG = Kr–Rn) and the Group 12 M^+-RG complexes (RG = Ar–Rn, but not Cd^+-Ar), the conclusion can be made that the interactions have a covalent contribution, which varies, but is most prominent for the species with the heavier RG atoms. Finally, for the Group 2 M^+-RG complexes (RG = Ar–Rn), there are no indications of covalency, since $H(R) < 0$, but consistent with comments made in some earlier work done by the Wright group at the University of Nottingham,[9,10] the significant sd hybridisation is described as chemical as it involves a significant perturbation of electron density that results in a stronger interaction. In contrast to comments made in earlier work of

the Wright group at the University of Nottingham[9], sp hybridisation appears to be minimal and covalency is the main mode of interaction.

In this work, the conclusion is made that sd hybridisation (and to a much lesser extent, sp hybridisation) causes a breakdown in the model electrostatic potential (Eqn. 1-2). This occurs since the potential uses fixed values for a range of electrostatic quantities applicable to a particular electronic state of M^+, and so they have no R dependence; however, the sd hybridisation is R dependent and happens to differing extents. Thus, it can be seen from Table 1-8 that for the cases where the heavier Group 2 M^+ are interacting with the heavier RG, values very far from the "physical" value of 1.00 are observed, with no solution being found for Ba^+-Ar. The failure of the model potential is particularly marked for the Ba^+-RG complexes owing to the very low energy of the unoccupied 5d orbitals; indeed, barium has been suggested as being an honorary transition metal.[79,80] In contrast, except for Be^+-Ne (see below), it is found that Z values fairly close to 1.00 for the Be^+-RG, Mg^+-RG and, most of the Group 12 M^+-RG complexes; however, given the covalency deduced for these species, these "sensible" values may simply be fortuitous.

The model potential results for Be^+-RG are unusual. As can be seen from Table 1-8, for most species, there is at most a very small rise in Z when damping is included, as expected – this is even true for the heavier Group 2 M^+-RG complexes, where sd hybridisation causes the model to fail. However, for the Be^+-RG complexes, the rises are quite substantial for all except Be^+-He, and is particularly marked for Be^+-Ne. It is notable that the BS plot in Figure 1-12 for this complex is also very unusual, and suggests that repulsion is playing a major role at R_e. Indeed, the value of the repulsive potential at R_e is 5.6×10^{-3} E_h for the undamped potential and 1.90×10^{-3} E_h for the damped potential. This, and the values for the other Be^+-RG potentials suggests that the simple electrostatic model potential with a two-parameter Born-Mayer potential is not sufficient to describe a potential where the RG and M^+ orbitals overlap and repel in an R-dependent way close to R_e.

A number of observations in the present work suggest that creating a universal diatomic potential would be extremely difficult, particularly the observation that R-dependent hybridisation, covalency and repulsion. These also suggest that defining a radius for an atom or atomic cation that is transferable to a wide range of species is also fraught with danger, as the interactions can be so different.

1.5 Bibliography

(1) Soldán, P.; Lee, E. P. F.; Lozeille, J.; Murrell, J. N.; Wright, T. G. High-quality interatomic potential for Li^{+}·He. *Chemical Physics Letters* **2001,** *343* (3–4), 429.

(2) Lozeille, J.; Winata, E.; Soldán, P.; Lee, E. P. F.; Viehland, L. A.; Wright, T. G. Spectroscopy of Li^{+}·Rg and Li^{+}·Rg transport coefficients (Rg = He-Rn). *Physical Chemistry Chemical Physics* **2002,** *4* (15), 3601.

(3) Viehland, L. A.; Lozeille, J.; Soldán, P.; Lee, E. P. F.; Wright, T. G. Spectroscopy of Na^{+}.Rg and transport coefficients of Na^{+} in Rg(Rg=He-Rn). *The Journal of Chemical Physics* **2003,** *119* (7), 3729.

(4) Viehland, L. A.; Lozeille, J.; Soldán, P.; Lee, E. P. F.; Wright, T. G. Spectroscopy of K^{+}·Rg and transport coefficients of K^{+} in Rg (Rg=He–Rn). *The Journal of Chemical Physics* **2004,** *121* (1), 341.

(5) Hickling, H. L.; Viehland, L. A.; Shepherd, D. T.; Soldán, P.; Lee, E. P. F.; Wright, T. G. Spectroscopy of M^{+}·Rg and transport coefficients of M^{+} in Rg (M = Rb–Fr; Rg = He–Rn). *Physical Chemistry Chemical Physics* **2004,** *6* (17), 4233.

(6) Breckenridge, W. H.; Ayles, V. L.; Wright, T. G. Analysis of the bonding in alkali-cation/Rg complexes (Rg=He–Xe) using a simple model potential. *Chemical Physics* **2007,** *333* (1), 77.

(7) Mcguirk, M. F.; Viehland, L. A.; Lee, E. P.; Breckenridge, W. H.; Withers, C. D.; Gardner, A. M.; Plowright, R. J.; Wright, T. G. Theoretical study of Ba^{n+}-RG (RG = rare gas) complexes and transport of Ba^{n+} through RG (n = 1,2; RG = He-Rn). *The Journal of Chemical Physics* **2009,** *130* (19), 194305.

(8) Gardner, A. M.; Withers, C. D.; Wright, T. G.; Kaplan, K. I.; Chapman, C. Y. N.; Viehland, L. A.; Lee, E. P. F.; Breckenridge, W. H. Theoretical study of the bonding in M^{n+}-RG complexes and the transport of M^{n+} through rare gas (M=Ca, Sr, and Ra; n=1 and 2; and RG=He–Rn). *The Journal of Chemical Physics* **2010,** *132* (5), 194305.

(9) Gardner, A. M.; Withers, C. D.; Graneek, J. B.; Wright, T. G.; Viehland, L. A.; Breckenridge, W. H. Theoretical Study of M^{+}−RG and M^{2+}−RG Complexes and Transport of M^{+} through RG (M = Be and Mg, RG = He−Rn). *The Journal of Physical Chemistry A* **2010,** *114* (28), 7631.

(10) Yousef, A.; Shrestha, S.; Viehland, L. A.; Lee, E. P.; Gray, B. R.; Ayles, V. L.; Wright, T. G.; Breckenridge, W. H. Interaction potentials and transport properties of coinage metal cations in rare gases. *The Journal of Chemical Physics* **2007,** *127* (15), 154309.

(11) Breckenridge, W. H.; Ayles, V. L.; Wright, T. G. Evidence for emergent chemical bonding in Au^+-Rg complexes (Rg = Ne, Ar, Kr, and Xe). *The Journal of Physical Chemistry A* **2008,** *112* (18), 4209.

(12) Qing, E.; Viehland, L. A.; Lee, E. P.; Wright, T. G. Interaction potentials and spectroscopy of Hg+Â·Rg and Cd+Â·Rg and transport coefficients for Hg+ and Cd+ in Rg (Rg==He[Single_Bond]Rn). *The Journal of Chemical Physics* **2006,** *124* (4), 3093.

(13) Lee, E. P. F.; Gray, B. R.; Joyner, N. A.; Johnson, S. H.; Viehland, L. A.; Breckenridge, W. H.; Wright, T. G. Accurate potential energy curves for Zn+–Rg (Rg=He–Rn): Spectroscopy and transport coefficients. *Chemical Physics Letters* **2007,** *450* (1), 19.

(14) Gray, B. R.; Lee, E. P. F.; Yousef, A.; Shrestha, S.; Viehland, L. A.; Wright, T. G. Accurate potential energy curves for Tl^+–Rg (Rg=He–Rn): spectroscopy and transport coefficients. *Molecular Physics* **2006,** *104* (20-21), 3237.

(15) Gardner, A. M.; Gutsmiedl, K. A.; Wright, T. G.; Breckenridge, W. H.; Chapman, C. Y. N.; Viehland, L. A. Theoretical study of Al^+–RG (RG=He–Rn). *The Journal of Chemical Physics* **2010,** *133* (16), 164302.

(16) Gardner, A. M.; Gutsmiedl, K. A.; Wright, T. G.; Lee, E. P. F.; Breckenridge, W. H.; Rajbhandari, S.; Chapman, C. Y. N.; Viehland, L. A. Theoretical Study of M^+−RG Complexes (M = Ga, In; RG = He−Rn). *The Journal of Physical Chemistry A* **2011,** *115* (25), 6979.

(17) Harris, J. P.; Gardner, A. M.; Wright, T. G.; Breckenridge, W. H.; Viehland, L. A. Interactions in the B^+–RG Complexes and Comparison with Be^+–RG (RG = He–Rn): Evidence for Chemical Bonding. *The Journal of Physical Chemistry A* **2012,** *116* (20), 4995.

(18) Bellert, D.; Breckenridge, W. H. Bonding in ground-state and excited-state A^+.Rg van der Waals ions (A = atom, Rg = rare-gas atom): a model-potential analysis. *Chemical Reviews* **2002,** *102* (5), 1595.

(19) Pyykkoe, P. Predicted Chemical Bonds between Rare Gases and Au^+. *Journal of the American Chemical Society* **1995,** *117* (7), 2067.

(20) Prascher, B. P.; Woon, D. E.; Peterson, K. A.; Dunning, T. H.; Wilson, A. K. Gaussian basis sets for use in correlated molecular calculations. VII. Valence, core-valence, and scalar relativistic basis sets for Li, Be, Na, and Mg. *Theoretical Chemistry Accounts* **2011,** *128* (1), 69.

(21) Hill, J. G.; Peterson, K. A. Gaussian basis sets for use in correlated molecular calculations. XI. Pseudopotential-based and all-electron relativistic basis sets for alkali metal (K-Fr) and alkaline earth (Ca-Ra) elements. *The Journal of Chemical Physics* **2017,** *147* (24), 244106.

(22) Peterson, K. A.; Puzzarini, C. Systematically convergent basis sets for transition metals. II. Pseudopotential-based correlation consistent basis sets for the group 11 (Cu, Ag, Au) and 12 (Zn, Cd, Hg) elements. *Theoretical Chemistry Accounts* **2005,** *114* (4-5), 283.

(23) Halkier, A.; Helgaker, T.; Jørgensen, P.; Klopper, W.; Koch, H.; Olsen, J.; Wilson, A. K. Basis-set convergence in correlated calculations on Ne, N 2 , and H 2 O. *Chemical Physics Letters* **1998,** *286* (3–4), 243.

(24) MOLPRO is a package of ab initio programs written by Werner, H.-J. K., P. J. et al.

(25) R. J. LeRoy, L. A. C. P. f. S. t. R. S. E. f. B. a. Q. L., University of Waterloo Chemical Physics Research Report No. CP-663, 2007; see http://leroy.uwaterloo.ca/programs/.

(26) Schaftenaar, G.; Noordik, J. H. Molden: a pre- and post-processing program for molecular and electronic structures. *Journal of Computer-Aided Molecular Design* **2000,** *14* (2), 123.

(27) Mulliken, R. S. Electronic Population Analysis on LCAO–MO Molecular Wave Functions. I. *The Journal of Chemical Physics* **1955,** *23* (10), 1833.

(28) Reed, A. E.; Weinstock, R. B.; Weinhold, F. Natural population analysis. *The Journal of Chemical Physics* **1985,** *83* (2), 735.

(29) Bader, R. F. W. *Atoms in molecules : a quantum theory*; Clarendon Press: Oxford, 1990.

(30) M. J. Frisch, G. W. T., H. B. Schlegel, G. E. Scuseria, M. A. Robb, J. R. Cheeseman, G. Scalmani, V. Barone, B. Mennucci, G. A. Petersson, H. Nakatsuji, M. Caricato, X. Li, H. P. Hratchian, A. F. Izmaylov, J. Bloino, G. Zheng, J. L. Sonnenberg, M. Hada, M. Ehara, K. Toyota, R. Fukuda, J. Hasegawa, M. Ishida, T. Nakajima, Y. Honda, O. Kitao, H. Nakai, T. Vreven, J. A. Montgomery, Jr., J. E. Peralta, F. Ogliaro, M. Bearpark, J. J. Heyd, E. Brothers, K. N. Kudin, V. N. Staroverov, R. Kobayashi, J. Normand, K. Raghavachari, A. Rendell, J. C. Burant, S. S. Iyengar, J. Tomasi, M. Cossi, N. Rega, J. M. Millam, M. Klene, J. E. Knox, J. B. Cross, V. Bakken, C. Adamo, J. Jaramillo, R. Gomperts, R. E. Stratmann, O. Yazyev, A. J. Austin, R. Cammi, C. Pomelli, J. W. Ochterski, R. L. Martin, K. Morokuma, V. G. Zakrzewski, G. A. Voth, P. Salvador, J. J. Dannenberg, S. Dapprich, A. D. Daniels, Ö. Farkas, J. B. Foresman, J. V. Ortiz, J. Cioslowski, and D. J. Fox. gaussian 09, Revision C.01. *Gaussian, Inc., Wallingford, CT* **2009**.

(31) Glendening, E. D. B., J. K.; Reed, A. E.; Carpenter, J. E.; Bohmann, J. A.; Morales, C. M.; Landis, C. R.; Weinhold, F. NBO 6.0, Theoretical Chemistry Institute, University of Wisconsin, Madison, 2013.

(32) Keith, T. A.; AIMAll, T. K.; Software, G.; Park, O.; KS; 2011; aim.tkgristmill.com, s.

(33) Subbaram, K. V.; Coxon, J. A.; Jones, W. E. Investigations of metal ion – rare gas pairs by optical spectroscopy: High resolution analysis of the $A^2\Pi_r$–$X^2\Sigma^+$ system of $BeAr^+$. *Canadian Journal of Physics* **1976,** *54* (54), 1535.

(34) Coxon, J. A.; Jones, W. E.; Subbaram, K. V. Electronic spectra of metal ion – rare gas pairs: : High resolution analysis of the $A^2\Pi_r$-$X^2\Sigma^+$ system of $BeKr^+$. *Canadian Journal of Physics* **1977,** *55* (3), 254.

(35) Coxon, J. A.; Jones, W. E.; Subbaram, K. V. First Observation of the $BeXe^+$ Molecule: The $A^2\Pi$–$X^2\Sigma$ Band System in Emission. *Canadian Journal of Physics* **1975,** *53* (19), 2321.

(36) Reddic, J. E.; Duncan, M. A. Photodissociation spectroscopy of the Mg^+-Ne complex. *The Journal of Chemical Physics* **1999,** *110* (20), 9948.

(37) Scurlock, C. T.; Pilgrim, J. S.; Duncan, M. A. Rotationally Resolved Photodissociation Spectroscopy of Mg^+-Ar. *The Journal of Chemical Physics* **1995,** *103* (9), 3293.

(38) Pilgrim, J. S.; Yeh, C. S.; Berry, K. R.; Duncan, M. A. Photodissociation spectroscopy of Mg^+–rare gas complexes. *The Journal of Chemical Physics* **1994,** *100* (11), 7945.

(39) Reddic, J. E.; Pullins, S. H.; Duncan, M. A. Photodissociation spectroscopy of the Ca^+–Ne complex. *The Journal of Chemical Physics* **2000,** *112* (11), 4974.

(40) Pullins, S. H.; Scurlock, C. T.; Reddic, J. E.; Duncan, M. A. Photodissociation spectroscopy of Ca^+–rare gas complexes. *The Journal of Chemical Physics* **1996,** *104* (19), 7518.

(41) Kaup, J. G.; Breckenridge, W. H. Bond energies of $CaAr^+$, $CaKr^+$, and $CaXe^+$ from resonant two-color photoionization thresholds. *The Journal of Chemical Physics* **1997,** *107* (12), 4451.

(42) Kaup, J. G.; Breckenridge, W. H. Spectroscopic characterization of the metastable $4p\pi\ ^2\Pi_{0-}$ valence states and the $5s\ ^3\Sigma^+$ Rydberg states of the CaAr, CaKr, and CaXe van der Waals molecules. *The Journal of Chemical Physics* **1997,** *107* (14), 5283.

(43) Kaup, J. G.; Breckenridge, W. H. Spectroscopic characterization of the singly excited CaAr($4d\pi\ ^3\Pi P_0$),CaAr($4d\delta\ ^3\Delta_1$) states and the doubly excited CaAr($4p\pi 4p\pi\ ^3\Sigma^-$) state. *J. Chem. Phys.* **1997,** *107* (15), 5676.

(44) Lüder, C.; Prekas, D.; Vourhotaki, A.; Velegrakis, M. Photodissociation spectrum of Sr^+Ne. *Chemical Physics Letters* **1997,** *267* (267), 149.

(45) Lüder, C.; Velegrakis, M. Photofragmentation spectrum of the Sr^+Ar complex. *The Journal of Chemical Physics* **1996,** *105* (6), 2167.

(46) Prekas, D.; Feng, B.-H.; Velegrakis, M. Vibrational constants and binding energies for the $A^2\Pi$ and $X^2\Sigma$ states of Sr^+Kr from photodissociation spectroscopy. *The Journal of Chemical Physics* **1998,** *108* (7), 2712.

(47) Massaouti, M.; Sfounis, A.; Velegrakis, M. Vibrational constants and binding energies of Sr^+Xe. *Chemical Physics Letters* **2001,** *348* (1), 47.

(48) Buchachenko, A. A.; Viehland, L. A. Interaction potentials and transport properties of Ba, Ba^+, and Ba^{2+} in rare gases from He to Xe. *The Journal of Chemical Physics* **2018,** *148* (15), 154304.

(49) Panov, S. I.; Williamson, J. M.; Miller, T. A. The electronic spectroscopy of the Ba^+–Ar complex - Potential surface and dissociation energies. *The Journal of Chemical Physics* **1995,** *102* (19), 7359.

(50) Viehland, L. A.; Hampt, D. S. The distribution of velocities for Ba^+ ions in Ar gas. *The Journal of Chemical Physics* **1992,** *97* (7), 4964.

(51) Tuttle, W. D.; Harris, J. P.; Zheng, Y.; Breckenridge, W. H.; Wright, T. G. Hybridisation and Covalency in the Group 2 and Group 12 Metal Cation/Rare Gas Complexes. *The Journal of Physical Chemistry A* **2018**, DOI:10.1021/acs.jpca.8b07139 10.1021/acs.jpca.8b07139.

(52) Kaup, J. G.; Leung, A. W. K.; Breckenridge, W. H. Spectroscopic characterization of the metastable $3p\pi\ ^3\Pi_{0+,0-}$ valence states and the $4s\ ^3\Sigma^+$ Rydberg states of the MgKr and MgXe van der Waals molecules. *The Journal of Chemical Physics* **1997,** *107* (24), 10492.

(53) Massick, S.; Breckenridge, W. H. A new class of strongly bound, doubly excited valence states of neutral van der Waals molecules: $Mg(3p\pi,3p\pi\ ^3P_J)$-$Ar(^3\Sigma^-)$. *The Journal of Chemical Physics* **1996,** *104* (19), 7784.

(54) Kaup, J. G.; Breckenridge, W. H. Bond energies of $MgKr^+$ and $MgXe^+$ from resonant two-color photoionization thresholds. *The Journal of Chemical Physics* **1997,** *107* (7), 2180.

(55) Niu, X. H. S., W. W.; Wang, S.; Shi, D. H. Accurate Spectroscopic Calculations on the $X^2\Sigma^+$, $A^2\Pi$, and $2^2\Sigma^+$ Electronic States of the $BeAr^+$ Cation Including Spin-Orbit Coupling. *Canadian Journal of Physics* **2014,** *92*, 397.

(56) Niu, X.; Zhu, Z.; Chen, Q. Ab initio study of the low-lying electronic states of [Be–Kr]$^{+}$. *Chemical Physics Letters* **2015,** *619*, 208.

(57) Abdessalem, K.; Mejrissi, L.; Issaoui, N.; Oujia, B.; Gadã©A, F. X. One and two-electron investigation of electronic structure for $Ba^{+}Xe$ and BaXe van der Waals molecules in a pseudopotential approach. *The Journal of Physical Chemistry A* **2013,** *117* (36), 8925.

(58) Goble, J. H.; Hartman, D. C.; Winn, J. S. Chemiluminescent associative ionization reactions. *The Journal of Chemical Physics* **1977,** *66* (1), 363.

(59) Winn, J. S. A systematic look at weakly bound diatomics. *Accounts of Chemical Research* **1981,** *14* (11), 341.

(60) Tellinghuisen, J.; Henderson, S. D.; Austin, D.; Lawley, K. P.; Donovan, R. J. Reduced potential-energy curves for diatomic molecules. *Physical Review A: General Physics* **1989,** *39* (3), 925.

(61) Hooydonk, G. V. Universal Two-Parameter Kratzer-Potential and Its Superiority over Morse's for Calculating and Scaling First-Order Spectroscopic Constants of 300 Diatomic Bonds. *European Journal of Inorganic Chemistry* **1999,** *1999* (10), 1617.

(62) Xie, R.-H.; Gong, J. Simple Three-Parameter Model Potential for Diatomic Systems: From Weakly and Strongly Bound Molecules to Metastable Molecular Ions. *Physical Review Letters* **2005,** *95* (26), 263202.

(63) Xie, R.-H.; Hsu, P. S. Universal Reduced Potential Function for Diatomic Systems. *Physical Review Letters* **2006,** *96* (24), 243201.

(64) Sutherland, G. B. B. M. The relation between the force constant, the inter-nuclear distance, and the dissociation energy of a diatomic linkage. *Proceedings of the Indian Academy of Sciences - Section A* **1938,** *8* (5), 341.

(65) Wright, T. G.; Breckenridge, W. H. The Radii of atomic ions determined from diatomic ion-He bond lengths. *The Journal of Physical Chemistry A* **2010,** *114* (9), 3182.

(66) Kramida, A. R., Yu.; Reader, J. and NIST ASD Team (2018). NIST Atomic Spectra Database (ver. 5.5.6), [Online]. Available: https://physics.nist.gov/asd [2018, July 6]. National Institute of Standards and Technology, Gaithersburg, MD.

(67) Tuttle, W. D.; Thorington, R. L.; Viehland, L. A.; Breckenridge, W. H.; Wright, T. G. Interactions of C+(2PJ) with rare gas atoms: incipient chemical interactions, potentials and transport coefficients. *Philosophical Transactions* **2018,** *376* (2115), 20170145.

(68) Tang, K. T.; Toennies, J. P. An improved simple model for the van der Waals potential based on universal damping functions for the dispersion coefficients. *The Journal of Chemical Physics* **1984,** *80* (8), 3726.

(69) Stone, A. J. *The theory of intermolecular forces*; Clarendon Press: Oxford, 1996.

(70) Koutselos, A. D.; Mason, E. A. Correlation and prediction of dispersion coefficients for isoelectronic systems. *The Journal of Chemical Physics* **1986,** *85* (4), 2154.

(71) Sahoo, B. K.; Timmermans, R. G. E.; Das, B. P.; Mukherjee, D. Comparative studies of dipole polarizabilities in Sr^+, Ba^+, and Ra^+ and their applications to optical clocks. *Physical Review A* **2009,** *80* (6), 062506.

(72) S. H. Patil, K. T. T. Multipolar polarizabilities and two- and three-body dispersion coefficients for alkali isoelectronic sequences. *The Journal of Chemical Physics* **1997,** *106* (6), 2298.

(73) Sahoo, B. K.; Das, B. P.; Chaudhuri, R. K.; Mukherjee, D.; Timmermans, R. G. E.; Jungmann, K. Investigations of properties to test possibilities for new optical-frequency standards. *Physical Review A* **2007,** *76* (4), 040504.

(74) Soldán, P.; Lee, E. P. F.; Wright, T. G. Static dipole polarizabilities (α) and static second hyperpolarizabilities (γ) of the rare gas atoms (He–Rn). *Physical Chemistry Chemical Physics* **2001,** *3* (21), 4661.

(75) J. LeRoy, R.; B. Bernstein, R. Dissociation energies of diatomic moleculles from vibrational spacings of higher levels: application to the halogens*. *Chemical Physics Letters* **1970,** *5* (1), 42.

(76) Le Roy, R. J.; Bernstein, R. B. Dissociation energies and long-range potentials of diatomic molecules from vibrational spacings: The halogens. *Journal of Molecular Spectroscopy* **1971,** *37* (1), 109.

(77) LeRoy, R. J.; Bernstein, R. B. Dissociation Energy and Long-Range Potential of Diatomic Molecules from Vibrational Spacings of Higher Levels. *The Journal of Chemical Physics* **1970,** *52* (8), 3869.

(78) Cremer, D.; Kraka, E. Chemical Bonds without Bonding Electron Density ? Does the Difference Electron-Density Analysis Suffice for a Description of the Chemical Bond? *Angewandte Chemie International Edition in English* **1984,** *23* (8), 627.

(79) Gagliardi, L.; Pyykkö, P. Cesium and barium as honorary d elements: CsN_7Ba as an example. *Theoretical Chemistry Accounts* **2003,** *110* (3), 205.

(80) Wu, X.; Zhao, L.; Jiang, D.; Fernández, I.; Berger, R.; Zhou, M.; Frenking, G. Barium as Honorary Transition Metal in Action: Experimental and Theoretical Study of $Ba(CO)^+$ and $Ba(CO)^-$. *Angewandte Chemie International Edition* **2018,** *57* (15), 3974.

Chapter 2

Assignment of REMPI Spectra of Some Disubstituted Benzenes

2.1 Introduction

This study uses the resonance-enhanced multiphoton ionisation (REMPI) spectroscopic technique to obtain electronic spectra of extremely cold substituted benzenes. As a key point in this work, REMPI spectra of *meta*-disubstituted and *ortho*-disubstituted benzenes are analysed, as a way of understanding the photophysics and photochemistry of biomolecules, such as nucleic acid bases and amino acids.

Vibrations are key quantities by which spectroscopists gain insight into both geometric and electronic structures of molecules. During an electronic transition or ionisation, elucidation of resultant changes in geometry and information on changes in electronic structure can be inferred by analysing the vibrational activity.[1] Basically, vibrational activity can be described by a labelling scheme including a limited number of vibrational modes (the normal modes), which contains all the possible motions consistent with the molecular symmetry. In this work, four disubstituted-benzene REMPI spectra are assigned and analysed. Four REMPI spectra of *meta*-disubstituted and *ortho*-disubstituted benzene in this work were mainly recorded by Drs. Adrian Gardner, William Tuttle and Mr. David Kemp, with the assignments being undertaken by the author.

As a fundamental component of most large biochemical molecules, it is insightful to investigate the vibrational spectroscopy of simple substituted benzenes in different electronic states.[1] Here listed are some factors why benzene is an interesting molecule:

(i) benzene is a molecule with high symmetry, and according to selection rules this will affect the appearance of the spectra;

(ii) vibronic coupling occurs;

(iii) as a type of prototypical aromatic molecule the observed spectroscopy can be compared with calculated results according to quantum chemistry, varying from simple Hückel theory through to state-of-art *ab initio* methods.[2]

The replacement of one or two hydrogen atoms with different atoms can directly cause the change of the electronic structure of the ring through donation or withdrawal of electron density by the substituent through inductive and mesomeric effects.[2] The direct study of biomolecules is complicated by two key aspects: (i) the excited electronic states are often short-lived owing to conical intersections, and so much of the detailed information on vibrational and torsional levels cannot be discerned; and (ii) they are difficult to get into the gas phase intact.[3] By observing the spectra of substituted benzenes, some key information which is related to the biochemical reaction and the behaviour of biomolecules becomes possible to be obtained from electronic excitation and photoelectron spectroscopy.[4]

2.1.1 Resonance-Enhanced Multiphoton Ionisation (REMPI) Spectroscopy

Modern electronic spectroscopy is a broad and constantly expanding field. As one important member of modern electronic spectroscopy techniques, resonance-enhanced multiphoton ionisation (REMPI)[5] is a technique applied to the spectroscopy of atoms and small molecules, which is a particularly powerful, and widely used in most laser mass spectrometric laboratories across the world[6]. As REMPI is a two-stage process, two photons are used to complete two different steps respectively, and often these will come from different lasers. One laser is used in the first step to excite the molecule to one excited intermediate state with one photon or more photons.[2] Then, the other laser provides one or more further photons which will be absorbed by the molecule to climb above the ionisation limit. It is notable that the ions can be detected with almost 100% efficiency and they can be mass-selected, which is a significant advantage of the REMPI technique.

Boesl *et al*.[7] performed the original definitive experiments in 1978. Then at Columbia, REMPI experiments were independently performed by Zandee *et al*.[8] REMPI spectroscopy is also widely used to study molecular complexes, the Wright group[9] at the University of Nottingham recorded the $\tilde{A} \leftarrow \tilde{X}$ transition of Xe·NO for the first time. The transition $\tilde{A} \leftarrow \tilde{X}$ of the Rg (Rg= Ar-Xe)·NO complexes has inspired a huge amount of attention[10]. With (1+1) resonanace-enhanced multiphoton ionisation (REMPI) spectroscopy, Miller[11] observed bound-bound

transitions for the Rg· NO complexes. In 1996, the first structured REMPI spectra of the $\tilde{A}$ state of Kr·NO was reported[12] and then in 1998 that of Xe·NO was first reported[13].

2.1.2 Molecular Vibrations

In order to simplify the study, molecules are usually regarded as if they contained nuclei fixed in space. As a matter of fact, molecules can of course move through space (translation), they can rotate and internuclear distances can be altered by vibrations. Since it is essentially unquantised motion, translational motion is uninteresting from the point of view of spectroscopy. While analysing a molecular sample qualitatively, the use of group vibrations is an important tool. However, vibrations and rotations are both very important motions for spectroscopists to study and so each will be considered with further details, beginning with molecular vibrations.[2]

Whilst, the situation is clearly more complicated for polyatomic molecules, since there is more than one bond that may be stretched/ compressed, and there are also bond angles that can be changed by vibrations. It is helpful to focus on small molecules to bring out key features applicable to more complicated molecules.

2.1.3 Labelling Scheme

In this work new labelling schemes, Gardner and Wright Scheme (or D_i schemes)[1,14] covering both the symmetrically- and asymmetrically-disubstituted benzenes is applied to all of the present molecules so that the ordering of the assignment can be consistent. As for the Mulliken[15] (Herzberg[16]) labelling scheme, it would give different labels to vibrational modes with the same motions to the same family of molecules.[1] Besides the Mulliken labelling scheme, Wilson mode labels[17] and the related Varsányi scheme[18] are also two existing labelling schemes which have been widely applied. It is quite common practice to use Wilson notation[17] to assign vibronic spectra of substituted benzenes while particular normal modes are associated with labelling bands[19]. Both Wilson notation[17] and the Varsányi scheme[18] have been discussed before and are regarded as unreliable[20]. As shown in previous work, it is possible to label the phenyl-localised vibrations of a range of *meta*-disubstituted benzenes consistently[20], where vibrations with the same or very similar atomic motion are associated with the same label.

An N-atomic linear molecule has 3N-5 normal modes of vibration, while 3N-6 for a non-linear one.[2,21] With D_i Scheme[1,14], all the modes of vibration can be express by one unique notation for one certain symmetry.

2.1.4 Symmetries of Vibrational Modes

Similar to transforming the molecular orbitals (MOs) of one molecule to the irreducible representations of the molecular point group, it is quite useful to transfer the normal vibrations to irreducible representations[2]. Since it makes classifying the modes according to symmetries become possible. One the other more important aspect, when establishing selection rules for transitions between vibrational levels in spectroscopy, it is important to realise that each normal mode has a certain type of symmetry. Particularly, the consideration about the symmetries of the vibrational wavefunctions is essential. As the symmetries of the normal coordinates and the vibrational wavefunctions are often confused with each other, considerable difficulty usually exists. The symmetry of the normal coordinate, during a vibration, is determined by the atomic motion. It is not necessary that the symmetry of the vibrational wavefunction should always be consistent with the symmetry of the normal coordinate. If the normal coordinate is totally symmetric, then the corresponding vibrational wavefunction is totally symmetric for all values of the vibrational quantum number. But, if the normal coordinate is non-totally symmetric, then the vibrational wavefunction will be totally symmetric when the vibrational quantum number is even and non-totally symmetric when the vibrational quantum number is odd.

2.1.5 Combination Bands, Overtones and Fermi Resonances

It is common for a spectroscopist to assign combination bands, overtones and Fermi resonances[22,23] to the features in a vibrational spectrum, which do not correspond to known fundamentals. Usually, the intensity of a combination band or an overtone is lower than a fundamental. While, briefly, the Fermi resonance is caused by the interaction between two close energy levels.

An overtone occurs when a vibrational mode is excited from ν=0 to ν=2, which is called the first overtone, or ν=0 to ν=3, the second overtone. The energy of the overtone transition will be approximately a whole multiple of the fundamental associated with the particular transition.[22,23]

A combination band is observed while more than two or more fundamental vibrations are excited simultaneously. [22-24]Due to the symmetry, even if a fundamental vibration cannot occur then a combination band involving it might occur.

2.2 Computational Details

In order to aid in the assignment of the spectra, the vibrational frequencies of both molecules were calculated in the Wright research group using the GAUSSIAN 09 software package.[25] The TD-B3LYP/aug-cc-pVTZ level of theory was employed for all S_1 state calculations, and all of the harmonic vibrational frequencies were scaled by the usual factor of 0.97 to account for any degree of anharmonicity.

The vibrational modes of the S_1 states were labelled by comparing the molecular vibrational displacements of each molecule with the S_0 vibrations modes of their counterparts via a generalized Duschinsky matrix approach. For this we employ the FC-LabII programme[26]. These results were then used by the author to assign the REMPI spectra, discussed below.

2.3 Assignment Methodology

The theoretical wavenumber of different vibrational modes were obtained from quantum chemical calculations. The assignment is supported by the theoretical wavenumber of each vibrational mode[1,14]. The REMPI spectra of *ortho*-disubstituted benzene and *meta*-disubstituted benzene were assigned by these steps: Assignment of fundamentals, and assignment of combinations, which is slightly more complicated than for the fundamentals. Assignment of fundamentals is a basic process before starting the assignment of other peaks, which could provide basic criteria to be referred to when assigning much more complex peaks. Those peaks which are generated by fundamental transition present the simplest transitions that happen in the electronic excitation. This means that the precise assignment for these can be greatly helpful to judge whether other combinations are reasonable, as some of these are caused by the coupling of two or several fundamentals. During the fundamental selection, two predominant factors must be considered. One is the similarity in value, while the other is the symmetry[27,28] of each vibrational mode. Briefly, the symmetry requirement can be expressed by the integral (Eqn. 2-1)：

$$\mu = \int \varphi^* \boldsymbol{\mu} \varphi d\tau \neq 0 \qquad \text{Eqn. 2-1}$$

where,

$$\boldsymbol{\mu} = \boldsymbol{i}\mu_x + \boldsymbol{j}\mu_y + \boldsymbol{k}\mu_z \qquad \text{Eqn. 2-2}$$

Here, $\boldsymbol{\mu}$ is the transition dipole moment operator. To get a totally symmetric representation, the combination of a coordinate *x, y* or *z* and the wavefunctions must belong to the same representation.[22,23,27,28] Thus, identifying the symmetry of the molecule is an important step.

The combination band is a much complicated circumstance compared to the fundamental band. Though the all the mathematical possible combinations can be calculated by the with a computer program written in Python (by Dr. J. P. Harris); however, many of the possible combinations are not symmetry allowed.

2.4 Results and Assignment

2.4.1 Assignment of *ortho*-difluorobenzene

Ortho-difluorobenzene belongs to the C_{2v} group.

Shown in Table 2-1 and Figure 2-1 is the assignment of the (1+1) REMPI spectrum of ortho-difluorobenzene. The assignment for each peak is based on the selection rules mentioned in methodology section. Then, a comparison between this assignment and Kable's[29] assignment (shown in Table 1 of this paper[29]) is applied. Vibrations D_{21} and D_{20} both have a_1 symmetry. The calculated values of 21^1 and 20^1 correspond to peak at 278 cm^{-1} and 398.5 cm^{-1} respectively which are in good agreement with the experimental values. Those two also match well with Kable's[29] assignment (shown in Table 1 of this paper[29]). In a similar way, it is obvious that the assignment for peak at 722.5 cm^{-1} should be 17^1 and the assignment at 925.5 cm^{-1} should be 15^1.

Listed above are four fundamental peaks which match the assignments in Swinn and Kable's work[29] exactly. There are also two combination assignments which match well with Kable's[29], 26^127^1 at 751.5 cm^{-1} and 17^120^1 at 1121.5 cm^{-1}.

One factor which should not be ignored is that the calculated values can be prone to error. Therefore, the calculated values cannot be completely relied on to make the assignment. Some calculated peak positions can deviate from the experimental value more than 20 cm^{-1}. This would cause the missing of some assignment. In order to make the assignment more reliable and reasonable, Kable's[29] assignment is used to gain insight on those peaks which are hard to assign. Then, some more fundamentals are found from Kable's work[29], 18^1 at 486.5 cm^{-1}, 19^1

at 511.5 cm^{-1}, 16^1 at 763.5 cm^{-1}, 13^1 at 1148 cm^{-1}, 12^1 at 1183.5 cm^{-1}, 11^1 at 1243.5 cm^{-1} and 10^1 at 486.5 cm^{-1}. Besides these fundamentals, many combinations and overtones are assigned as well, 29^2 at 241.5 cm^{-1}, 30^2 at 257 cm^{-1}, 28^2 at 581.5 cm^{-1}, $25^1 29^1$ at 606.5 cm^{-1}, 27^2 at 614.5 cm^{-1}, 26^2 at 893 cm^{-1}, $19^1 20^1$ at 909.5 cm^{-1}, $23^1 28^1$ at 934 cm^{-1}, 18^2 at 971 cm^{-1}, 25^2 at 980cm^{-1}, 24^2 at 1102 cm^{-1}, $15^1 21^1$ at 1202.5 cm^{-1}, $22^1 25^1$ at 1241cm^{-1} and 17^2 at 1444.5 cm^{-1}.

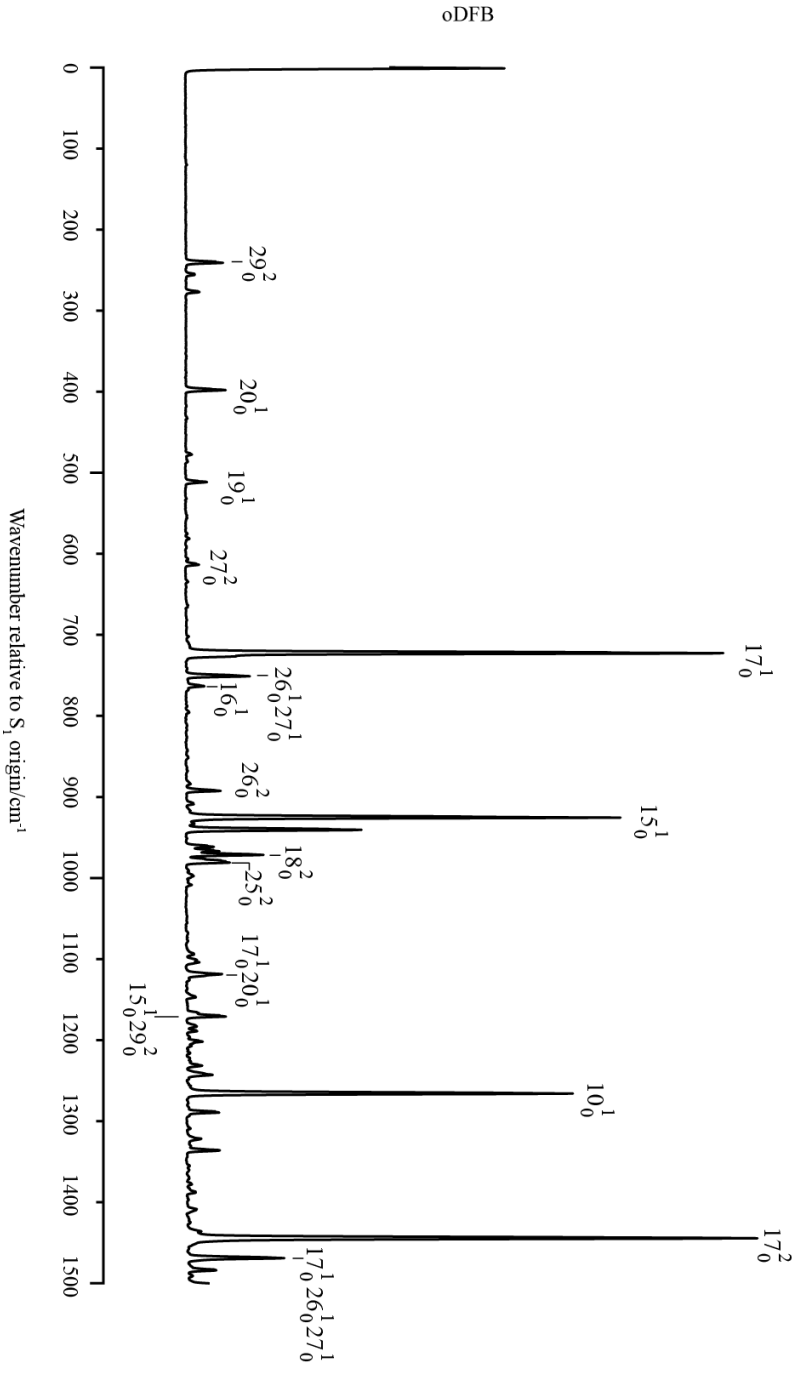


Figure 2-1. Assigned REMPI spectra of *ortho*-difluorobenzene to wavenumber ~ 1500 cm^{-1}

Table 2-1: Assignment of *ortho*-difluorobenzene

Wavenumber [a] (cm^{-1})	Assignment	Wavenumber [a] (cm^{-1})	Assignment
241.5	29^2	971	18^2
257	30^2	980	25^2
278	21^1	1102	24^2
398.5	20^1	1105	?
478	29^4	1119	13^1
486.5	18^1	1122	17^120^1
511.5	19^1	1148	13^1
575.5	26^130^1	1172	15^129^2
581.5	28^2	1184	12^1
606.5	25^129^1	1189	$23^128^129^2$
614.5	27^2	1203	15^121^1
722.5	17^1	1204	16^120^1
751.5	26^127^1	1241	22^125^1
763.5	16^1	1244	11^1
840.5	16^1	1266	10^1
893	26^2	1290	
909.5	19^120^1	1337	$20^123^128^1$
925.5	15^1	1445	17^2
934	23^128^1	1470	$17^126^127^1$
962	?	1484	$17^118^121^1$
967.5	17^129^2		

[a] Measured relative to the origin transition at 37827 cm^{-1}.

In Kable's paper[29] published before, some triple and quadruple combinations were also assigned, 17^129^2 at 967.5 cm^{-1}, 15^129^2 at 1171.5 cm^{-1}, $20^123^128^1$ at 1337 cm^{-1}, $17^126^127^1$ at 1469.5 cm^{-1}, $17^118^121^1$ at 1484 cm^{-1}, 29^4 at 478 cm^{-1} and $23^128^129^2$ at 1188.5 cm^{-1}. Assignment merely based on calculated values might cause high deviation for combinations and overtones. But these assignments for combinations and overtones, from the experimental work can be much more reliable.

In this work, the peak at 840.5 cm^{-1} is assigned as 16^1 according to the results from the quantum chemical calculation. The peak in Kable's paper[14,29] was labelled with a question mark, while in this work it is assigned.

At the low-wavenumber end of the spectrum, the transition at 398.5 cm^{-1} is regarded as 20^1 and the transition at 511.5 cm^{-1} is regarded as 19^1. Then the transition at 909.5 cm^{-1} is labelled as 19^120^1. The sum of the wavenumbers of vibrations D_{20} and D_{19} is exactly 910 cm^{-1}, via this

result the assignment for the transition at 909.5 cm^{-1} is reasonable. The peak at 971 cm^{-1} is assigned as the overtone of vibration D_{18}. It can be seen that the wavenumber 971 cm^{-1} is roughly equal to the double of 486.5 cm^{-1}. The assignment $17^{1}20^{1}$ also approximately equals to the sum of vibrations D_{17} and D_{20}. Similarly, the transition at 1202.5 cm^{-1} is assigned as $15^{1}21^{1}$ which seems quite rational with the same reason as well as the peak at 1204 cm^{-1} assigned as $16^{1}20^{1}$. The peak at 1444.5 cm^{-1} assigned as 17^{2} can also be regarded as a reliable assignment.

For the triple combination, there are a number of assignments that also obey this principle. The transition $17^{1}29^{2}$ at 967.5 cm^{-1} matches well with the sum of two wavenumbers, 722.5 cm^{-1}, 241.5 cm^{-1}. The peak at 1171.5 cm^{-1} also shows a good consistency with the sum value of vibration D_{15} and two D_{29}. As for the quadruple combinations, the assignment, 29^{4} for the peak at 478 cm^{-1} obeys this principle, whose sum equals to 483 cm^{-1}.

From this, it is obvious to see that the deviation between the wavenumber of the peak and the sum wavenumber of several assigned peaks would increase with the increasing of the multiplicity of the combination, even though the values used here are all experimental values. Therefore, the assignment for combinations with calculated values requires more caution.

2.4.2 Assignment of *ortho*-chlorofluorobenzene

Ortho-chlorofluorobenzene also belongs to the C_s group.

There are 30 vibrational modes in *ortho*-chlorofluorobenzene molecule. Because of the increasing uncertainty in the assignment in the high wavenumber region, the assignment for REMPI spectra of *ortho*-chlorofluorobenzene molecule is only attempted below 1500 cm^{-1}. The assignment process for this molecule turns to a little more complicated compared to *ortho*-difluorobenzene because the two substituents are different. Another factor causing complexity is two principal stable isotopes of chlorine, ^{35}Cl (75.78%) and ^{37}Cl (24.22%).

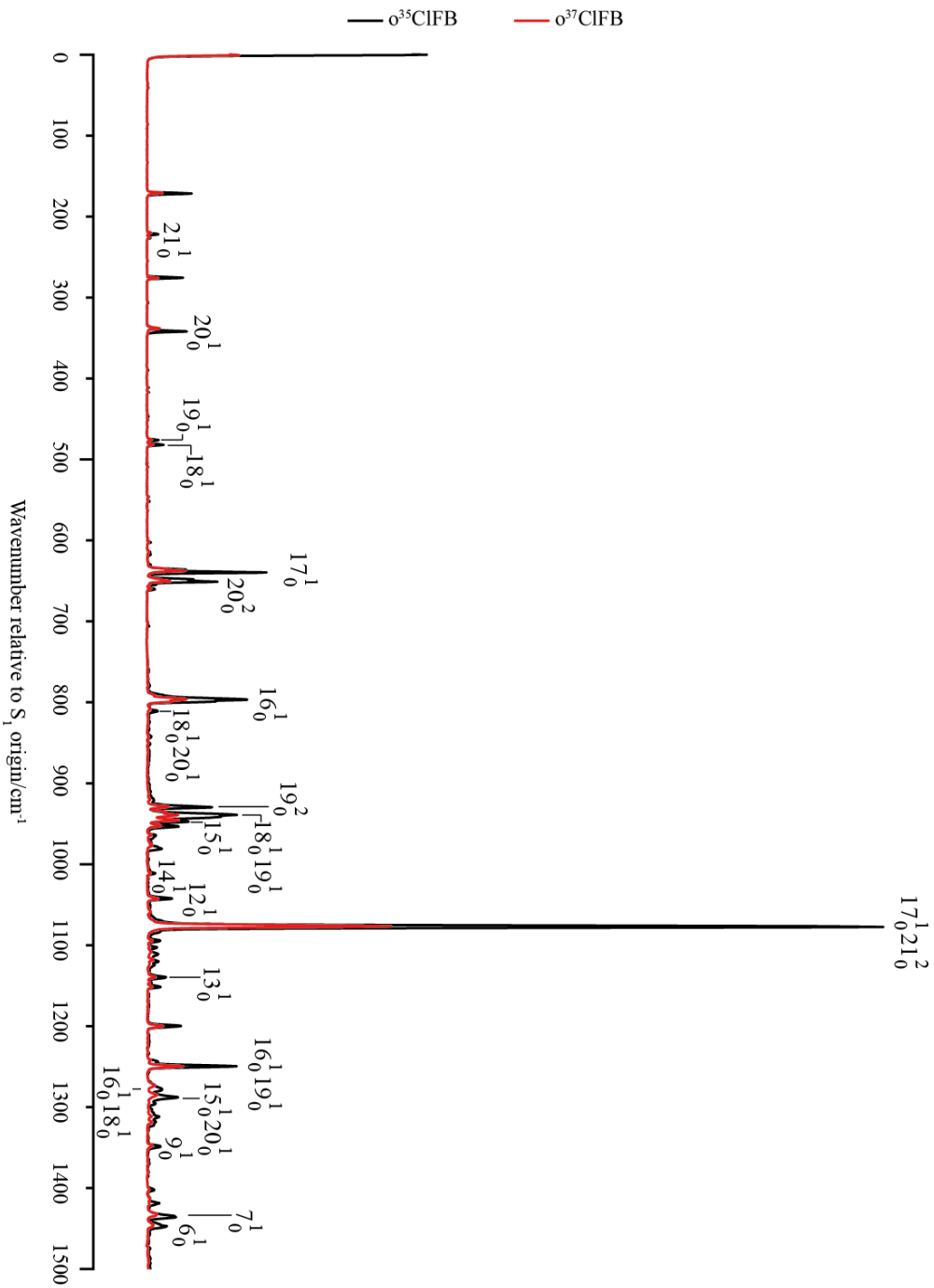


Figure 2-2. Assigned REMPI spectra *ortho*-chlorofluorobenzene to wavenumber ~ 1500 cm^{-1}. The black trace is the ^{35}Cl isotopologue, and the red one ^{37}Cl.

Figure 2-2 shows brief assignment of *o*-ClFB. The obvious ratio difference between ^{35}Cl (75.78%) and ^{37}Cl (24.22%) provides an important clue to distinguish the ^{35}Cl and ^{37}Cl isotopologues. Generally, those peaks with smaller area under the curve are regarded as attributable to the ^{37}Cl molecule. Before assigning the combinations, all the fundamentals before 1500 cm^{-1} are picked out first.

Table 2-2: Assignment of *ortho*-chlorofluorobenzene

^{35}Cl-Wavenumber [a] (cm^{-1})	^{37}Cl-Frequency [a] (cm^{-1})	Assignment	^{35}Cl-Wavenumber [a] (cm^{-1})	^{37}Cl-Wavenumber [a] (cm^{-1})	Assignment
171.5	171	?	941.5	939	26^2 or $25^1 28^1 30^2$
222	220.5	21^1	947.5	946	$18^1 19^1$
275.5	276	?	953.5	952.5	15^1
342	338	20^1	964.5	964.5	$17^1 20^1$ or $23^1 28^1$ or $21^1 25^1$ 27^1
337.5	336	?	981.5	975.5	$21^1 26^1 28^1$
476	476	19^1	1013.5	1012.5	14^1
482	482	18^1	1042.5	1043	12^1
546.5	547.5	$20^1 21^1$	1077.5	1076.5	$17^1 21^2$
636.5	635	$27^1 28^1$ or 27^2 or $21^1 28^1 30^1$	1094.5	1095.5	$20^1 26^1 28$ or $18^1 27^1 28^1$
639.5	637.5	17^1	1140.5	1140	13^1
648	648	27^2	1200	1200.5	21, 23, 28 or 16, 28, 30
651	650.5	20^2	1244	1242	11^1
660.5	660	21^3	1249.5	1250	$16^1 19^1$
797	796.5	16^1	1278.5	1273	$16^1 18^1$
799	799	$19^1 20^1$	1288.5	1284	$15^1 20^1$
811	808	$18^1 20^1$	1349	1348	9^1
929.5	929	19^2	1436	1432	7^1
939	935	19^2	1447	1445	6^1

[a] Measured relative to the origin transition at 37048 cm^{-1}.

These are the first assignments of this spectrum. Here, the calculated values are only used as a guide to assign the peaks on the spectra.

Then, some assignments of multiple combination which have adjacent wavenumbers with the sum wavenumbers of combined vibrational modes are also picked out. Although, all the assignments for this molecule can only be made according to the calculation, the repeated vibrational modes in combinations let the assignment become more reasonable. But, one thing needs to be mentioned is that other assignments are sometimes possible. More detailed assignments are listed in Table 2-2.

Another efficient way to check those assignments is to see whether the isotopic shift is in a reasonable range which is usually set as 1.5 cm^{-1} in this study. As a requirement according to the selection rule, all the assignments listed here have a_1 symmetry.

2.4.3 Assignment of *meta*-difluorobenzene

Meta-difluorobenzene belongs to the C_{2v} group.

There are totally 30 vibrational modes in *meta*-difluorobenzene molecule. In Kable's paper[30] (see Table I in this paper), most peaks are assigned. This is a valuable resource to make a comparison between the present work and Kable's[30]. In this work peaks were only assigned to the wavenumber 1300 cm^{-1}, as shown in Figure 2-3 and Table 2-3.

In this part, assignments are still based on the calculated values. Then the assignment is compared with previous assignment made by Kable et al.[16]. It is found that only the peak at 317.5 cm^{-1} and the peak at 254 cm^{-1} from the calculated assignment match Kable's assignment[30], which are labelled as 21^1 and 30^2 respectively as well as 18^121^1 for the peak at 759.5 cm^{-1}.

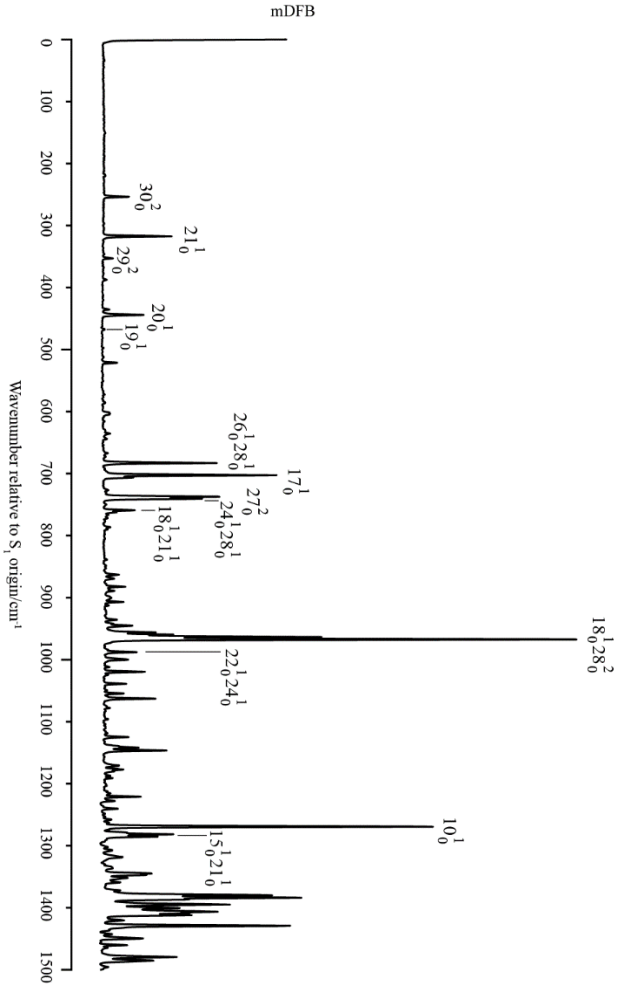


Figure 2-3. Assigned REMPI spectra *meta*-difluorobenzene to wavenumber ~ 1500 cm^{-1}

One thing that needs to be mentioned is that the peak at 683 cm^{-1} and the peak at 702.5 cm^{-1} are regarded as 17^1 and 26^128^1 respectively. But the order is exactly opposite in Kable's work[30]. From this, a limited similarity between the calculated values and experimental results can be seen. Two other similar assignments are listed in Table 2-3. The peak at 740.5 cm^{-1} is considered as a combination of 25^1 and 28^1, while it was 24^128^1 in Kable's[30] experimental work.

Table 2-3: Assignment of *meta*-difluorobenzene

Wavenumber [a] (cm^{-1})	Assignment	Wavenumber [a] (cm^{-1})	Assignment
254	30^2	901.5	24, 26
317.5	21^1	908	19,20
354	29^2	937	19^120^1
444.5	20^1	957	24^2 or 24^125^1
471	19^1	963.5	28^218^1
605.5	25^130^1 or $26^1\ 30^1$	1000.5	22^124^1
683	26^128^1	1012.5	17^13^1
702.5	17^1	1020.5	17^13^1
737	27^2	1039.5	23^127^1
740.5	24^128^1	1063	22^125^1
759.5	18^121^1	1063.5	22^125^1 or 22^2
883.5	18^1	1269.5	10^1
900	24^126^1 or $25^1\ 26^1$	1281	15^121^1

[a] Measured relative to the origin transition at 37926.5 cm^{-1}.

For this molecule, only 5 peaks were assigned as fundamentals, 21^1 at 317.5 cm^{-1}, 20^1 at 444.5 cm^{-1}, 19^1 at 471 cm^{-1}, 17^1 at 702.5 cm^{-1} and 10^1 at 1269.5 cm^{-1}. One feature of these fundamental peaks is the intensity of all these peaks are relatively higher than peaks nearby.

Only two positions at 908 cm^{-1} and 937 cm^{-1} repeated the same labels at the beginning of the assignment as combinations, 19^120^1. The calculated wavenumber of D_{19} is 440 cm^{-1} and it is 462 cm^{-1} for 20^1, which means the sum of two wavenumbers is 902 cm^{-1}. Though it seems much closer to 908 cm^{-1}, the deviation cannot be ignored.

2.4.4 Assignment of *meta*-chlorofluorobenzene

1, 3-chloro fluorobenzene belongs to the C_s point group.

In order to keep the reliability of the assignment, only the peaks in region till 1500 cm^{-1} are assigned.

Table 2-4: Assignment of *meta*-chlorofluorobenzene

^{35}Cl-Wavenumber [a] (cm^{-1})	^{37}Cl-Wavenumber [a] (cm^{-1})	Assignment	^{35}Cl-Wavenumber [a] (cm^{-1})	^{37}Cl-Wavenumber [a] (cm^{-1})	Assignment
205.5	205	$29^1 30^1$	1041	1044	$17^1 28^1 29^1$
241	239.5	21^1	1053.5	1054	$17^1 19^1$
328.5	329.5	29^2	1091.5	1091	$16^1 21^1$
367.5	364	20^1	1092	1091.5	$17^1 18^1$
429	429.5	19^1 or $27^1 30^1$	1117	1118	12^1
456	455.5	18^1 or 21^2	1134.5	1135	$19^1 20^2$
515.5	516	$25^1 30^1$	1207.5	1207.5	$17^1 26^1 29^1$
638	636.5	17^1 or $25^1 29^1$	1220	1221.5	$22^1 25^1$
660	660.5	$26^1 28^1$ or $19^1 21^1$	1220.5	1221.5	11^1 $22^1 25^1$
697.5	698	$18^1 21^1$	1252.5	1253	$13^1 21^1$
714	714.5	$25^1 28^1$ or 20^2	1253	1253.5	$15^1 28^1 30^1$
849.5	850	16^1	1274	1271.5	10^1
949	950	25^2	1344	1345	9^1
962.5	962.5	15^1 or 23, 28	1369	1369.5	$13^1 20^1$
967.5	967.5	$23^1 28^1$	1392.5	1395	$15^1 18^1$
982	983.5	$17^1 20^1$	1484	1484	$22^1 23$ or 22^2
1002.5	1000.5	14^1	1485.5	1484	$22^1 23^1$ or 22^2
1025	1026	13^1			

[a] Measured relative to the origin transition at 37045 cm^{-1}.

Assignments for the peaks in REMPI spectra are made according to the result of the calculation. *Meta*-chlorofluorobenzene is still a molecule with isotopic shift effect. Thus, the different positions of the peaks can be used as a clue to check whether the assignment is reasonable or not. As shown in Table 2-4 and Figure 2-4, most isotopic shift values are ranged from 0.5-1.5 cm^{-1}. For instance, the ^{35}Cl peak at 241 cm^{-1} and the ^{37}Cl peak at 239.5 cm^{-1} are labelled as 21^1, the ^{35}Cl peak at 367.5 cm^{-1} and ^{37}Cl peak at 364 cm^{-1} are labelled as 20^1. The density of fundamentals decreases gradually with the increasing of the wavenumber while the assignments of low wavenumber peaks are much more reliable.

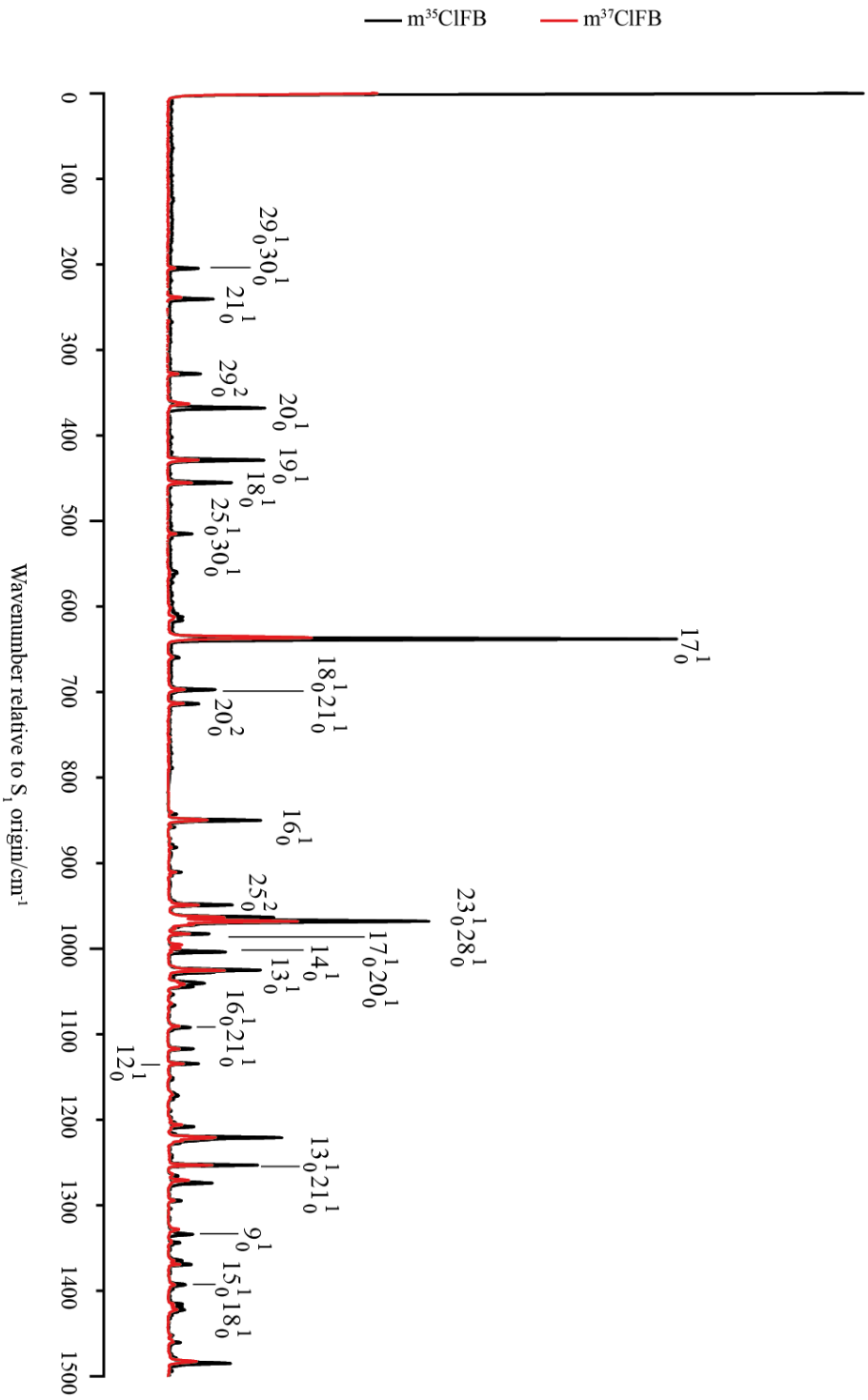


Figure 2-4. Assigned REMPI spectra *meta*-chlorofluorobenzene to wavenumber ~ 1500 cm^{-1}

Although most combinations are also assigned to each peak according to the value. In this work, in order to select more reasonable assignment for the combination an efficient is applied - comparing the assignment with the figures of different calculated vibration modes of *meta*-

difluorobenzene[1]. Though, *meta*-chlorofluorobenzene and *meta*-difluorobenzene are two different molecules, they still share a quite similar structure. It is worthwhile to test the assignment against this comparison. Because of the different isotopic Cl atoms in *meta*-cholorofluorobenzene, the motion of this special substitute might be slightly different after the combination of several vibrational modes. For instance, the overlap of the same vibrational mode might more likely cause an isotopic shift in spectra. A combination of different vibrational motions towards different directions would cause the decrease of the isotopic shift. The isotopic shift for the first peak pair, ^{35}Cl peak at 205.5 cm^{-1} and ^{37}Cl peak at 205 cm^{-1} show a minor isotopic shift, 0.5cm^{-1}. Referred to calculated vibration modes of *meta*-difluorobenzene, one substitute has totally different moving direction in D_{29} and D_{30}. Therefore, the minor isotopic shift in this position makes sense in this aspect. The difference between ^{35}Cl peak at 205.5 cm^{-1} and ^{37}Cl peak at 205 cm^{-1} is 1 cm^{-1}, which is a little larger than 0.5 cm^{-1}. It is obvious that the combination of the same vibrational modes causes a motion of the Cl atom as a substitute in *meta*-chlorofluorobenzene as expected, then the greater isotopic shift shows up.

Not only can the combination of several vibrational modes be considered by this method, but it can also be used for fundamentals. The ^{35}Cl peak and ^{37}Cl peak are both located at 962.5 cm^{-1}, there is no isotopic shift observed. In D_{15}, whose symmetry is a', both two substitutes do not move. This rationalises why the isotopic shift is not seen. The isotopic shift is 1 cm^{-1} for the assignment (^{35}Cl peak at 1025 cm^{-1} and ^{37}Cl peak at 1026 cm^{-1}), which is labelled as 13^1. In vibration D_{13}, the motion of two substitutes are apparently to be seen. As a consequence, the consideration of concrete vibrational modes with the purely mathematical assignment works well when lacking of supported assignment in previous works.

It is still a useful way to pick out some more reliable combinations, such as 19^121^1 for the ^{35}Cl peak at 660 cm^{-1} and ^{37}Cl peak at 660.5 cm^{-1}. 19^1 and 21^1 are both transitions shown up before this peak. The wavenumber corresponds to transition ^{35}Cl 19^1 is 429 cm^{-1}, while it is 429.5 cm^{-1} for ^{37}Cl peak. As for 21^1, the former is 241 cm^{-1}, the latter is 239.5 cm^{-1}. The sum value is 670 cm^{-1} and 669 cm^{-1} respectively. Compared to ^{35}Cl peak at 660 cm^{-1} and ^{37}Cl peak at 660.5 cm^{-1} they are in an acceptable range of difference. Thus, 19^121^1 is considered as a reliable assignment for this peak.

2.4.5 A Comparison between *ortho*-difluorobenzene and *meta*-difluorobenzene REMPI Spectra

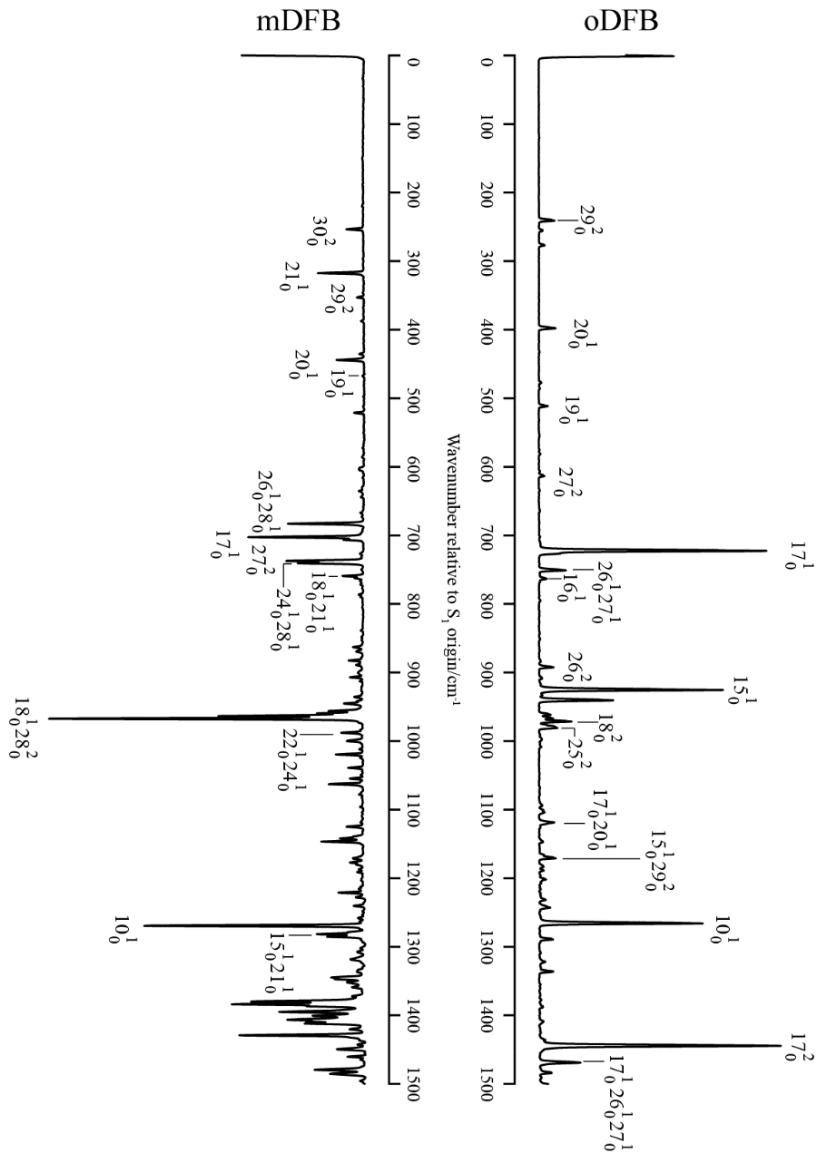


Figure 2-5. A Comparison between assigned REMPI Spectra of *ortho*-difluorobenzene and *m eta*-difluorobenzene to wavenumber ~ 1500 cm^{-1}

In all four spectra, the transition 17^1 is commonly the strongest one. It happens at the position of 700 cm^{-1} to *o*-difluorobenzene and *m*-difluorobenzene REMPI spectra. Although the vibrational motions can be different even with the same D_i numbers for meta and ortho molecules, it is still notable that the fundamental transition 10^1 happens at around 1270 cm^{-1} in both *o*-DFB and *m*-DFB spectra, it is a rare similarly transition in this high wavenumber region,

which is already higher than 1200 cm^{-1}. The intensities of two peaks are also similarly strong, this confirm the correctness in another aspect. In the wavenumber range from 200 cm^{-1} to 700 cm^{-1} similarity appears as expected. Though the 29^2 transition happens at 241.5 cm^{-1} in *o*-DFB REMPI spectrum, it shows up at 354 cm^{-1} in *m*-DFB REMPI spectrum, which is more than 110 cm^{-1} higher than the position in *o*-DFB REMPI spectrum. There is also a difference, 46 cm^{-1} between two positions of 20^1 transition in two spectra, though seems large, the position is relatively similar. 19^1 transition shows up at 511.5 cm^{-1} in *o*-DFB REMPI spectrum, while the position for the same transition is at 471 cm^{-1}. Both two positions of 19^1 are around 500 cm^{-1}.

The sequence of 29^2, 20^1, 19^1, 27^2 transitions can be seen either oDFB REMPI spectrum or mDFB REMPI spectrum. Thus, assignments in the range [200 cm^{-1},700 cm^{-1}] are sensible according to this comparison.

2.4.6 A Comparison between *ortho*-chlorofluorobenzene and *meta*-chlorofluorobenzene REMPI Spectra

The comparison between *o*-chlorofluorobenzene and *m*-chlorofluorobenzene REMPI spectra is shown in Figure 2-6 some similarities of assignment can be found in this figure. In *o*-chlorofluorobenzene REMPI spectrum, the transition 21^1 of ^{35}Cl isotope shows up at 222 cm^{-1} and the transition 21^1 of ^{37}Cl isotope show up at 220.5 cm^{-1}, while the 21^1 transitions of ^{35}Cl *m*-chlorofluorobenzene and ^{37}Cl isotope also show up at 241 cm^{-1} and 239.5 cm^{-1} respectively. The transition peaks 20^1 also show up at a similar position around 300 cm^{-1}. The peaks of 19^1 appear at about 500 cm^{-1} in both spectra as well as 18^1. One thing needs to be emphasised is that the order of 19^1 and 18^1 keep consistent in two REMPI spectra with 19^1 coming before 18^1. 17^1 transitions happen both at a position of 640 cm^{-1} roughly, they are the most similar transitions compared to others before this position. The intensity of the transition peak 17^1 in *m*-chlorofluorobenzene REMPI spectrum is much stronger than the one in *o*-chlorofluorobenzene REMPI spectrum. In *m*ClFB REMPI spectrum, the peak of 20^2 transition slightly shift to a position over wavenumber 700 cm^{-1}.

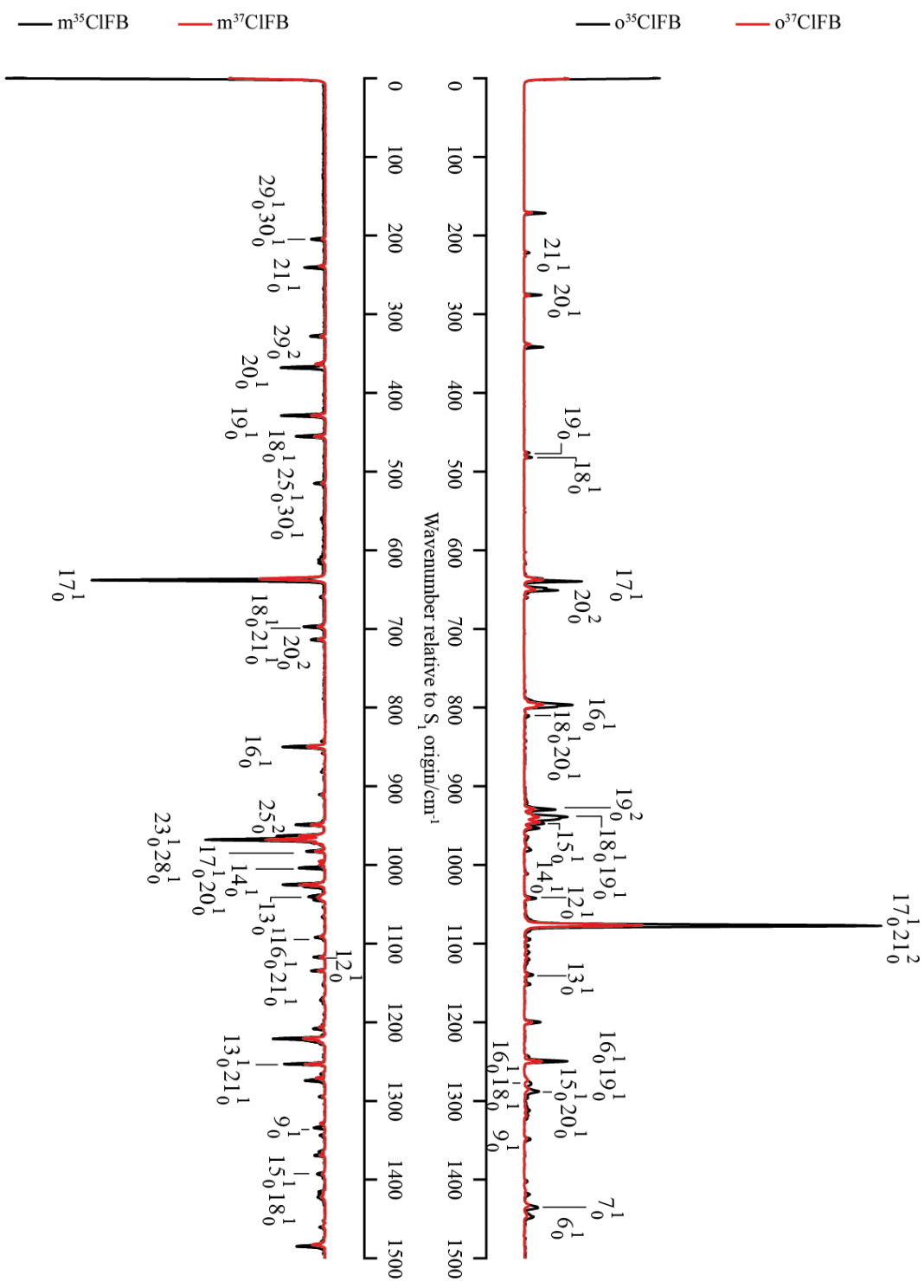


Figure 2-6. A Comparison between assigned *ortho*-chlorofluorobenzene and *ortho*-difluorobenzene REMPI Spectra to wavenumber ~ 1500 cm^{-1}

A finding which is worth emphasising is that the 20^1 band shows up around 300 cm^{-1} and then the combination peaks also share the similar position in two spectrum. This is a strong evidence to confirm the correctness of all 4 assignments. Two peaks of transition 16^1 also happen before 800 cm^{-1} and after 800 cm^{-1} respectively. 14^1 transitions both happen near the position of 1010 cm^{-1}. Transition 9^1 has a special similar assignment in the high wavenumber region of both two different REMPI spectra.

The order of transitions 12^1 and 13^1 is swapped in two REMPI spectra. In the spectrum of oClFB, the transition 12^1 comes first relative to 13^1 at the position before wavenumber 1100 cm^{-1}. The order is exactly opposite in the REMPI spectrum of *m*-ClFB.

From this comparison, at least the assignments from 200 cm^{-1} to 640 cm^{-1} can be regarded as more reliable than other assignments in the higher wavenumber range, where such similarity cannot be found in those two spectra. As for many peaks labelled in this work in the region from 900 cm^{-1} to 1500 cm^{-1}, the similarity does not show up as expected. Since *o*-ClFB and *m*-ClFB are two different molecules in structure but with the same C_s symmetry, the vibrations will be different. Then different transitions happen in each specific position, especially for those combinations. While there is only limited previous work to compare, this kind of comparison provides some proof to check the assignments made in this work.

2.5 Conclusions

In this work, assigned electronic spectra of the $S_1 \leftarrow S_0$ transition of *ortho*-difluorobenzene, *ortho*-chlorofluorobenzene, *meta*-difluorobenzene and *meta*-chlorofluorobenzene up to ~1500 cm^{-1} are presented respectively, using REMPI spectroscopy. For higher wavenumber region, the difficulty becomes obvious in REMPI spectra, thus assignments higher than 1500 cm^{-1} are not shown in this work. D_i labelling scheme[1,14] played an important role in this study, to keep the consistency of all assignments for four molecules. It is useful to identify the combination of vibrational modes in molecules so that an understanding of energy flow through the vibrational modes can be gained.[4] The assignment of *ortho*-difluorobenzene is compared to previous research by Swinn and Kable[29] to confirm the reliability of the analysis here. Assignment of *meta*-difluorobenzene in Scott's paper[30] are used to compare with assignment based on calculation in this work. A type of self-matching method is applied for all four-molecule assignment to make sure of the correctness, which is emphasised above (see 2.4.4). Via two typical comparisons of assigned spectra (see 2.4.5 and 2.4.6), some expected

similarities were found, which should be caused by the similar molecular structure and behaviours.

Further confirmation would be useful, such as by zero-kinetic-energy (ZEKE) photoelectron spectra of *o*-DFB, *m*-DFB, *o*-ClFB and *m*-ClFB molecules[31]. This technique detects pulsed-filed ionisation of very high-lying Rydberg states that are within a few cm^{-1} of an ionisation threshold. The technique essentially allows photoelectron spectra to be recorded with a resolution close to that of the lasers. This can allow vibrational and torsional levels to be resolved.[32-34]

In summary, this work provides fundamental information especially the assignment which provides an understanding of the vibrational behaviour of these four molecules discussed above, *o*-DFB, *m*-DFB, *o*-ClFB and *m*-ClFB. In the future studies, the two-dimensional-LIF (2D-LIF) and ZEKE spectra will also give key information on how mixed the vibrational levels have become – this directly impacts on how well energy can be dispersed in the molecule, and so how well it can resist photo-fragmentation, which occurs when internal energy is localized in particular chemical bonds.

2.6 Bibliography

(1) Kemp, D. J.; Tuttle, W. D.; Jones, F. M. S.; Gardner, A. M.; Andrejeva, A.; Wakefield, J. C. A.; Wright, T. G. Consistent assignment of the vibrations of symmetric and asymmetric *meta*-disubstituted benzenes. *Journal of Molecular Spectroscopy* **2018,** *346*, 46.

(2) Ellis, A.; Feher, M.; Wright, T. *Electronic and Photoelectron Spectroscopy : Fundamentals and Case Studies*; Cambridge University Press: [Erscheinungsort nicht ermittelbar], 2011.

(3) Nalda, R. d.; Bañares, L. *Ultrafast Phenomena in Molecular Sciences : Femtosecond Physics and Chemistry*; Springer: Cham [etc.], 2014.

(4) Andrejeva, A.; Tuttle, W. D.; Harris, J. P.; Wright, T. G. Assignment of the vibrations of the S_0, S_1, and D_0^+ states of perhydrogenated and perdeuterated isotopologues of chlorobenzene. *The Journal of Chemical Physics* **2015,** *143* (10), 104312.

(5) Boesl, U.; Weinkauf, R.; Schlag, E. W. Reflectron time-of-flight mass spectrometry and laser excitation for the analysis of neutrals, ionized molecules and secondary fragments. *International Journal of Mass Spectrometry and Ion Processes* **1992,** *112* (2), 121.

(6) Schlag, E. W. *ZEKE spectroscopy*; Cambridge Univ. Press: Cambridge, 1998.

(7) Boesl, U.; Neusser, H. J.; Schlag, E. W. In *Zeitschrift für Naturforschung A*, 1978; Vol. 33.

(8) Zandee, L.; Bernstein, R. B.; Lichtin, D. A. Vibronic/mass spectroscopy via multiphoton ionization of a molecular beam: the I_2 molecule. *The Journal of Chemical Physics* **1978,** *69* (7), 3427.

(9) Mack, P.; M. Dyke, J.; G. Wright, T. Ã←X̃ transition of Rg·NO complexes (Rg=rare gas) observed using resonance-enhanced multiphoton ionization (REMPI) spectroscopy Xe·NO. *Journal of the Chemical Society, Faraday Transactions* **1998,** *94* (5), 629.

(10) Gamblin, S. D.; Daire, S. E.; Lozeille, J.; Wright, T. G. Further investigations of the Ã←X̃ transition of the Kr·NO and Xe·NO complexes using (1+1) REMPI spectroscopy. *Chemical Physics Letters* **2000,** *325* (1), 232.

(11) Miller, J. C. The A $^2\Sigma^+$ state of rare gas–NO van der Waals molecules probed by 1+1 multiphoton ionization spectroscopy. *The Journal of Chemical Physics* **1989,** *90* (8), 4031.

(12) Bush, A. M.; Dyke, J. M.; Mack, P.; Smith, D. M.; Wright, T. G. One- and two-color resonance-enhanced multiphoton ionization spectroscopy of the Kr·NO complex via the $\tilde{A}\,^2\Sigma^+$ state. *The Journal of Chemical Physics* **1996,** *105* (22), 9804.

(13) Mack, P.; M. Dyke, J.; G. Wright, T. Ã←̃transition of Rg·NO complexes (Rg=rare gas) observed using resonance-enhanced multiphoton ionization (REMPI) spectroscopy Xe·NO. *Journal of the Chemical Society, Faraday Transactions* **1998,** *94* (5), 629.

(14) Gardner, A. M.; Wright, T. G. Consistent assignment of the vibrations of monosubstituted benzenes. *The Journal of Chemical Physics* **2011,** *135* (11), 114305.

(15) Rosenbluth, M. N. Report on Notation for the Spectra of Polyatomic Molecules. *The Journal of Chemical Physics* **1955,** *23* (5), 1118.

(16) Herzberg, G. Molecular Spectra and Molecular Structure V1. *American Journal of Physics* **1991,** *-1* (6), 273.

(17) Jr, E. B. W. The Normal Modes and Frequencies of Vibration of the Regular Plane Hexagon Model of the Benzene Molecule. *Physical Review* **1934,** *45* (10), 706.

(18) Varsányi, G.; Láng, L.; Kovner, M. A.; Lempert, K. *Assignment for Vibrational Spectra of Seven Hundred Benzene Derivatives*; Hilger: London, 1976.

(19) Pugliesi, I.; Tonge, N. M.; Cockett, M. C. An excited state ab initio and multidimensional Franck-Condon analysis of the $A\,^1B_2 \leftarrow X\,^1A_1$ band system of fluorobenzene. *The Journal of Chemical Physics* **2008,** *129* (10), 104303.

(20) Andrejeva, A. International Symposium on Molecular Spectroscopy, 2014; p 1.

(21) Atkins, P. W.; De Paula, J. *Physical chemistry*; W.H. Freeman: New York, 2010.

(22) Atkins, P. W.; Oxford University, P. *Molecular quantum mechanics : An Introduction to Quantum Chemistry. Vol. 2, Vol. 2*; Clarendon Press: Oxford, 1970.

(23) Guillory, W. A. *Introduction to Molecular Structure and Spectroscopy*; Allyn and Bacon, Inc.: Boston, 1977.

(24) Diem, M. *Introduction to Modern Vibrational Spectroscopy*; Wiley: New York, N.Y., 1993.

(25) M. J. Frisch, G. W. T., H. B. Schlegel, G. E. Scuseria, M. A. Robb, J. R. Cheeseman, G. Scalmani, V. Barone, B. Mennucci, G. A. Petersson, H. Nakatsuji, M. Caricato, X. Li, H. P. Hratchian, A. F. Izmaylov, J. Bloino, G. Zheng, J. L. Sonnenberg, M. Hada, M. Ehara, K. Toyota, R. Fukuda, J. Hasegawa, M. Ishida, T. Nakajima, Y. Honda, O. Kitao, H. Nakai, T. Vreven, J. A. Montgomery, Jr., J. E. Peralta, F. Ogliaro, M. Bearpark, J. J. Heyd, E. Brothers, K. N. Kudin, V. N. Staroverov, R. Kobayashi, J. Normand, K. Raghavachari, A. Rendell, J. C. Burant, S. S. Iyengar, J. Tomasi, M. Cossi,

N. Rega, J. M. Millam, M. Klene, J. E. Knox, J. B. Cross, V. Bakken, C. Adamo, J. Jaramillo, R. Gomperts, R. E. Stratmann, O. Yazyev, A. J. Austin, R. Cammi, C. Pomelli, J. W. Ochterski, R. L. Martin, K. Morokuma, V. G. Zakrzewski, G. A. Voth, P. Salvador, J. J. Dannenberg, S. Dapprich, A. D. Daniels, Ö. Farkas, J. B. Foresman, J. V. Ortiz, J. Cioslowski, and D. J. Fox. Gaussian 09, Revision C.01. *Gaussian, Inc., Wallingford, CT* **2009**.

(26) Pugliesi, I.; Müllerdethlefs†, K. Excited-State Ab Initio Calculations and Multidimensional Franck−Condon Simulations on Guanine. *The Journal of Physical Chemistry A* **2006,** *110* (48), 13045.

(27) Cotton, F. A. *Chemical Applications of Group Theory*; Wiley-India: Delhi, 2011.

(28) Bertolucci, M. D.; Harris, D. C. *Symmetry and Spectroscopy : An Introduction to Vibrational and Electronic Spectroscopy*; Oxford University Press: New York, 1996.

(29) Swinn, A. K.; Kable, S. H. The S_1 ($^1A_1$)– S_0 ($^1A_1$) Electronic Transition of Jet-Cooled *o*-Difluorobenzene. *Journal of Molecular Spectroscopy* **1998,** *191* (1), 49.

(30) Graham, P. A.; Kable, S. H. The electronic spectroscopy of jet-cooled *m*-difluorobenzene. *The Journal of Chemical Physics* **1995,** *103* (15), 6426.

(31) Reiser, G.; Rieger, D.; Wright, T. G.; Mueller-Dethlefs, K.; Schlag, E. W. Zero-kinetic-energy (ZEKE) photoelectron spectroscopy of *p*-difluorobenzene via different intermediate vibrational levels in the S_1 state. *The Journal of Physical Chemistry* **1993,** *97* (17), 4335.

(32) Gardner, A. M.; Tuttle, W. D.; Whalley, L.; Claydon, A.; Carter, J. H.; Wright, T. G. Torsion and vibration-torsion levels of the S1 and ground cation electronic states of para-fluorotoluene. *The Journal of Chemical Physics* **2016,** *145* (12), 124307.

(33) Gardner, A. M.; Tuttle, W. D.; Groner, P.; Wright, T. G. Molecular symmetry group analysis of the low-wavenumber torsions and vibration-torsions in the S_1 state and ground state cation of p-xylene: An investigation using resonance-enhanced multiphoton ionization (REMPI) and zero-kinetic-energy (ZEKE) spectroscopy. *The Journal of Chemical Physics* **2017,** *146* (12), 26.

(34) Gardner, Adrian M.; Tuttle, W. D.; Whalley, L. E.; Wright, T. G. Direct observation of vibrational energy dispersal via methyl torsions. *Chemical Science* **2018,** *9* (8), 2270.